NISTIR 6875

Final Report: Effective Non-Toxic Metallic Fire Suppressants

Gregory Linteris

U. S. DEPARTMENT OF COMMERCE
Technology Administration
Building and Fire Research Laboratory
National Institute of Standards
and Technology
Gaithersburg, MD 20899

National Institute of Standards and Technology
Technology Administration
U.S. Department of Commerce

NISTIR 6875

Final Report: Effective Non-Toxic Metallic Fire Suppressants

Gregory Linteris

U. S. DEPARTMENT OF COMMERCE
Technology Administration
Building and Fire Research Laboratory
National Institute of Standards
and Technology
Gaithersburg, MD 20899

May 2002

U.S. DEPARTMENT OF COMMERCE
Donald L. Evans, Secretary

TECHNOLOGY ADMINISTRATION
Phillip J. Bond, Under Secretary for Technology

NATIONAL INSTITUTE OF STANDARDS
AND TECHNOLOGY
Arden L. Bernent. Jr.. Director

Final Technical Report

Effective Non-Toxic Metallic Fire Suppressants

4D/13/1
Date: 2/14/2002

Gregory Linteris', Marc Rumminger[1], Valeri Babushok',
Harsha Chelliah', Tony Lazzarini', and Pasan Wanigarathne'

[1] Building and Fire Research Laboratory
Fire Research Division
100 Bureau Dr. Stop 8652
Gaithersburg MD 20899-8652

'Mechanical and Aerospace Eng.
University of Virginia
122 Engineer's Way
P.O.Box 400746
Charlottesville, VA 22904-4746

February, 2002

Final Technical Report, Jan . 2001 – Dec. 2001

Sponsored by:
The Department of Defense
Strategic Environniental Research and Development Program

Table of Contents

1. Summary

1.1. Task Objectives

The purpose of the project was to: a.) identify which metal species would be effective flame inhibitors, and then b.) attempt to find non-toxic forms of the metal which could be used. Very early in the project, however, we determined that metal species—in any form—might not be effective in practical flames. This in itself was a major finding, and hence an additional, most important objective of the project became: c.) determining the reasons for the unexpected low effectiveness of $Fe(CO)_5$ in cup-burner flames.

1.2. Technical Problems

The main unexpected difficulty in the project relative to the original plans was that the performance of the super-effective agent $Fe(CO)_5$ was found to be highly dependent upon the type of flame used to assess its performance. For example, $Fe(CO)_5$, which is about 80 times as effective as CF_3Br in reducing the overall reaction rate of premixed flames, appeared to be nearly ineffective in subsequent tests in cup burner flames [1]. The problem then became to determine if $Fe(CO)_5$ was indeed ineffective, or perhaps if it was losing its effectiveness—as in premixed and counterflow diffusion flames—but just earlier. To do this it was necessary to develop a new protocol for cup burner extinction to assess the effectiveness of powerful metallic radical scavenging agents over a range of mole fractions, and then examine the performance of $Fe(CO)_5$ (as well as other potentially effective new metals) in the cup burner using this new method.

1.3. General Methodology

Screening tests to find new metallic inhibitors which had strong effects on the overall reaction rate were first conducted in premixed systems. The most promising candidates, Mn and Sn containing compounds, were thus tested for their ability to reduce the flame speed of premixed methane-air flames. These tests also provided a clear delineation of possible loss of effectiveness due to condensation for these low-residence time flames. Since these flames are amenable to numerical modeling of the gas-phase chemistry, such calculations, together with thermodynamic equilibrium calculations, were then used to understand the reasons for the differences in effectiveness between Fe, Sn, and Mn. It was also desired to determine if blends of metals would help to overcome the loss of effectiveness due to condensation. For these investigations, we preformed premixed flame speed determinations with blends of $Fe(CO)_5$ and MMT.

An additional goal of this project was to search for non-toxic forms of metals that might be effective fire suppressants. One approach, both for testing the metal compounds as well as well as for using them in practical applications, is to add metallic compounds to water droplets. Hence, we conducted tests to validate a reliable system for evaluating metal additives to water droplets, and used them to assess the potential of several metal compounds. Both premixed and counterflow diffusion flames of methane and air were used, with droplets of water and solutions. The additives included NaOH, KOH, NaCl, and $FeCl_2$.

Finally, we sought to further understand the effectiveness of metal-based inhibitors in flames resembling fires, and explain why they were surprisingly ineffective for those conditions. For this purpose, we employed cup-burner flames with the organometallic compounds added to the air stream. An approach was developed in which CO_2 was used as the primary suppressant, and the metal compound was added in order to reduce the quantity of CO_2 required for extinction. Since particle formation was believed to be the cause of loss of effectiveness, we conducted laser scattering measurements in the 3-D flow field above cup-burner flames with $Fe(CO)_5$ added to the air stream

1.4. Technical Results

New data and results obtained as a result of this work are:

a.) the flame speed of premixed methane-air flames in the presence of tetramethyltin ($Sn(CH_3)_4$, TMT) at T_{in}=21 ° C; ϕ=0.9, 1.0, and 1.1; and $X_{O_2,\mathrm{ox}}$ =0.2, 0.21, and 0.24.

b.) the flame speed of premixed methane-air flames in the presence of **methylcyclopentadienylmanganese** tricarbonyl ($CH_3C_5H_4Mn(CO)_3$, MMT) at T_{in}=80 ° C; ϕ=0.9, 1.0, and 1.1; and $X_{O_2,\mathrm{ox}}$ =0.19, 0.2, 0.21, and 0.24.

c.) the flame speed of premixed methane-air flames in the presence of MMT and $Fe(CO)_5$ at T_{in}=80 ° C, ϕ=1.0, and $X_{O_2,\mathrm{ox}}$ =0.24.

d.) the extinction condition of counterflow diffusion flames with pure water droplets and water with NaOH, KOH, NaCl, and $FeCl_2$ at variable droplet mass fraction.

e.) the decrease in flame speed of premixed methane-air flames (ϕ=1.0) with added water droplets and water-NaOH solutions.

f.) cup-burner extinction conditions of methane-air flames in the presence of CO_2, Br_2, and CF_3Br.

g.) cup-burner extinction conditions of methane-air flames in the presence of CO_2 combined with a range of mole fractions of CF_3Br, TMT, MMT, or $Fe(CO)_5$. Also performed were tests of the extinction volume fraction of CO_2 with a range of mole fraction of TMT/ MMT/$Fe(CO)_5$ (in a fixed proportion) in the air stream.

h.) the laser light scattering cross section for particles in cup-burner flames of methane and air inhibited by CO_2 and a blended with $Fe(CO)_5$ at a volume fraction of (100, 200, 325, and 450) µL/L in the air stream.

1.5. Important Findings and Conclusions

a.) MMT and TMT are forty and three as effective as $Fe(CO)_5$ in reducing the overall reaction rate of CH_4-air flames.

b.) TMT and MMT lose their effectiveness for inhibiting premixed CH_4-air flames at 3000 and 300 µL/L, respectively, and the loss is stronger than that which would occur due to radical depletion.

c.) $Fe(CO)_5$ added to MMT-inhibited flames showed additional inhibition, indicating that radical depletion is not the reason for the loss of effectiveness observed for MMT-inhibited flames.

d.) The difference in efficiency between TMT, MMT, and $Fe(CO)_5$ is caused by the stability of the metal di-hydroxide intermediates.

e.) The alkali metal hydroxides NaOH and KOH were shown to be effective additives to water droplets, reducing the droplet mass fraction for extinction of counterflow diffusion flames by a factor of three and four, respectively.

f.) For the first time, alkali metals have been shown to have an upper limit of additive mole fraction for their efficient use as flame inhibitors. The cause is believed to be the limiting vapor pressure of intermediate species.

g.) The effectiveness of water droplets in counterflow diffusion flames was shown to be strongly affected by droplet diameter. This highlights the importance of the relationship between droplet size and flow residence time, which is even more important for the case of water with additives.

h.) The performance of water droplets (with or without additives) is highly dependent upon the flame type. This highlights the importance of understanding the temperature and flow field existing in actual fires in order to select the proper droplet size for efficient use of the suppressant.

i.) TMT, MMT, and $Fe(CO)_5$, even when added at low mole fraction, are much less effective at inhibiting cup-burner flames than they are at inhibiting premixed and counterflow diffusion flames.

j.) The effectiveness of TMT, MMT, and $Fe(CO)_5$ in cup-burner flames drops off precipitously above (4000, 400, and 400) µL/L.

k.) The performance of a super-effective inhibitor can vary drastically depending upon the type of flame in which it is tested.

l.) Large scattering signals were measured in cup-burner flames inhibited by $Fe(CO)_5$, indicating the presence of particles, that are believed to be the cause of the poor performance of metals in cup-burner flames.

m.) The following physical effects are believed to be important in chemical inhibition by metal compounds:

  1.) gas-phase transport of the active iron-containing species to the region of high H-atom is necessary for efficient inhibition.

  2.) Particle formation near the location of peak [H] can act as a sink for the iron-containing intermediate species and reduce the catalytic effect.

  3.) The mole fraction of inhibitor influences condensation since at low values, it may be below its saturation value.

  4.) The available residence time affects particle growth.

  5.) Thermophoretic forces can be large in the flame and re-distribute particles away from peak [H].

  6.) Convection and drag forces can prevent particles from reaching the region of peak [H].

1.6. Significant Hardware Developments

We designed, built, tested, and optimized the following:

a.) A system for introducing multiple organometallic agents to the fuel or air stream of a cup burner.
b.) A system for accurately introducing Br_2 to the air stream of a cup burner.
c.) A laser scattering system for measuring nanoparticles in cup-burner flames.

1.7. Special Comments

There are two major findings of this work:

a.) In cup-burner flames, condensation of active metal-containing intermediate species, combined with the flow field and thermophoretic effects, sequester the active species and prevent them from reaching the region of the flame where they are required to extinguish the flame, and

b.) For any inhibitor-flame system containing particles, the effectiveness of the agent will be highly dependent upon the type of flame used to assess the performance. (Note that particles may be present either from the form of the added suppressant itself, or from intermediate species which condense after the suppressant is added to the fire).

1.8. Implications for Further Research

More work needs to be done *to* understand if other super effective agents, for example. those containing phosphorus, form particles during inhibition of flames resembling fires. If so, they too may be plagued by the demonstrated loss of effectiveness for metal species in cup-burner flames. It is difficult to interpret what is actually happening in the cup burner to make the metals ineffective. We have proposed plausible (if unproven) mechanisms by which the metals may become ineffective. Nonetheless, stronger, more accurate statements could be made if we understood the fundamental mechanisms by which chemically active suppressants (e.g., CF_3Br, Br_2, etc., which are effective in the cup burner) work to cause flame extinction. Specifically, it is required to determine: a.) the actual flow field in the cup-burner; b.) the regions of the flame most susceptible to catalytic radical recombination; and c.) the transport rates of the inhibitor to these regions. Detailed flame structure calculations and measurements, of the type previously performed for premixed and counterflow diffusion flames, would yield this information. These data and calculations would provide a much sounder basis for understanding the fate and role of chemically active species in practical suppressed fires, and are in important first step towards understanding the action of chemical inhibitors in actual suppressed fires.

2. Bibliography

1. **Babushok, V., Tsang, W., Linteris, G. T. and Reinelt, D., "Chemical Limits to Flame Inhibition,"*Combustion und Flame*, 115, pp. 551-560, 1998.
2. **Rumminger, M., Reinelt, D., Babushok, V., and Linteris, G. T., "Numerical Study of the Inhibition of Premixed and Diffusion Flames by Iron Pentacarbonyl," *Combustion and Flume,* **116**(1-2), **pp.** 207-219, 1999.
3. Rumminger, M. D.; Reinelt, D.; Babushok, V. I.; Linteris. G. T., "Inhibition of Flames by Iron Pentacarbonyl," *Hulon Options Technical Working Conference.* HOTWC-98. Proceedings. May 12-14, 1998, Albuquerque, New Mexico, 1-12 pp, 1998.
4. Rumminger, M.D. and Linteris, G.T., "Particle Measurements in $Fe(CO)_5$-Inhibited Flames," *NIST Annual Conference on Fire Research,* Rockville MD, Nov. 2-5, 1998.
5. Rumminger, M.D. and Linteris, G.T., "The Role of Particles in Flame Inhibition by Iron Pentacarbonyl," *Halon Options Technical Working Conference*, Albuquerque, NM, April 27-29, 1999, pp. 511-521.
6. Runiminger, M.D. and Linteris, G.T., "Particle Measurements in Flames Inhibited by Iron Pentacarbonyl", *Joint Meeting of' the United Stutes Sections of the Combustion Institute,* Washington, D.C., March 1999.
7. Linteris, G.T. and Rumminger, M.D., "Flame Inhibition by Ferrocene, Carbon Dioxide, and Trifluorornethane Blends: Synergistic and Anti-synergistic Effects," *1999 Full Technical Meeting, Eastern States Section of the Combustion Institute,* July, 1999.
8. **Rumminger, M.D. and Linteris, G.T., "Numerical Modeling of Inhibition of Counterflow Diffusion Flames by Iron Pentacarbonyl", in *Fire Safety Science Proceedings of the Sixth International Symposium,* International Association for Fire Safety Science (Michel Curtat, Ed.). Marne-La-Vallee, France, 2000. pp. 289-300.
9. **Rumminger, M.D. and Linteris, G.T., "Inhibition of Premixed Carbon Monoxide-Hydrogen-Oxygen-Nitrogen Flames by Iron Pentacarbonyl," *Combustion and Flume,* **120**(4):451-464, 2000.
10. ""Linteris, G.T. and Rumminger, M.D., "Premixed Carbon Monoxide/Nitrous Oxide/Hydrogen Flames: Measured and Calculated Burning Velocities with and without $Fe(CO)_5$," *Combustion and Flame,* **122**(1/2):58-75, 2000.
11. **Rumminger, M.D. and Linteris, G.T. "The Role of Particles in Flame Inhibition by Iron Pentacarbonyl," *Combustion and Flame,* **123**(1/2):82-94, 2000.
12. Linteris, G.T. and Rumminger, M.D., "Flame Inhibition by Ferrocene, Carbon Dioxide, and Trifluoromethane Blends: Synergistic and Anti-synergistic Effects," *1999 Full Technical Meeting, Eastern Stutes Section of'the Combustion Institute,* July, 1999.
13. Linteris, G.T. and Rumminger, M.D., "Flame Inhibition by Ferrocene, Alone and with CO_2 and CF_3H," *Halon Options Technical Working Conference,* Albuquerque, NM, May 2-4, 2000, pp. 129-140.
14. Lazzarini, A. K., Krauss, R. H., Chelliah, H. K., and Linteris, G. T., "Extinction of Counterflow Diffusion Flames with Fine-Water Droplets," *Halon Options Technical Working Conference,* Albuquerque, NM, May 2-4, 2000, **pp.** 195-203.

15. **Linteris, G.T., Rumminger, M.D., Babushok, V.I., and Tsang, W., “Flame Inhibition by Ferrocene, and by Blends of Inert and Catalytic Agents,” *Proceedings of the Combustion Institute*, 28:2965-2972, 2000.
16. **Lazzarini, A.M., Krauss, R.H., Chelliah, H.K., and Linteris, G.T, “Extinction Conditions of Non-premixed Flames with Fine Droplets of Water and Water-NaOH Solutions, *Proceedings of the Combustion Institute*, 28:2939-2945, 2000.
17. Wanigarathne, P.C., Krauss, R. H., Chelliah, H. K., and Davis, R.J., “Fire Suppression by Particulates Containing Metallic Compounds,” *Halon Options Technical Working Conference*, Albuquerque, NM, May 2-4. 2000, pp. 393-402.
18. Linteris, G.T. “Suppression of Cup-Burner Diffusion Flames by Super-Effective Chemical Inhibitors and Inert Compounds,” *Halon Options Technical Working Conference*, Albuquerque, NM, April 24-26, 2001, pp. 187-196.
19. Linteris, G. T., Knyazev, V., and Babushok, V., “Premixed Flame Inhibition by Manganese and Tin Compounds,” *Halon Options Technical Working Conference*, Albuquerque, NM, April 24-26, 2001, pp. 72-82.
20. Chelliah, H.K., Lazzarini, A.K., Wanigarathne, P.A., and Linteris, G. T., “A Comparison of Fire Suppression Effectiveness of Sodium Bicarbonate Particles and Fine-Water Droplets in Non-Premixed and Premixed Flames,” *Halon Options Technical Working Conference*, Albuquerque, NM, April 24-26, 2001, pp. 389-394.
21. **Rumminger, M.D. and Linteris, G. T., “Particle Formation in Counterflow Diffusion Flames Inhibited by Iron Pentacarbonyl,” *Combustion and Flame*, **128**(1/2):145-164, 2002.
22. Babushok, V. I., Knyazev, V. D., and Linteris, G. T., “Mechanisms of Flame Inhibition by Tin and Manganese Containing Additives,” *Fifth International Conference on Chemical Kinetics;* Jul 16 - Jul 20, 2001, Gaithersburg, MD, 2001. p. 116.
23. **Linteris, G. T., Knyazev, V., and Babushok, V., “Inhibition of Premixed Methane Flames by Manganese and Tin Compounds,” accepted for publication in *Combustion and Flame*, Dec. 2001.
24. **Linteris, G. T., “Extinction of Cup-Burner Diffusion Flames by Catalytic and Inert Inhibitors,” submitted to *Proc. Combust. Inst. Vol. 29,* Dec. 2001.
25. **Rumminger, M.D., Babushok, V.I., and Linteris, G. T., “Spatial Effects in Chemical Inhibition of Premixed Flames,” submitted to *Proc. Combust. Inst. Vol. 29,* Dec. 2001.
26. **Chelliah, H.K., Lazzarini, A.K., Wanigarathne, P.C., Linteris, G. T., “Inhibition of Premixed and Non-Premixed Flames with Fine Droplets of Water and Solutions,” submitted to *Proc. Combust. Inst. Vol. 29,* Dec. 2001.
27. Linteris, G.T. and Rumminger, M.D., “Particle Formation in Laminar Flames Inhibited by Metals,” Western States Section Meeting, The Combustion Institute, March 25-26, 2002, La Jolla, CA.
28. Linteris, G. T., “Loss of Effectiveness of Organometallic Agents in Cup-Burner Flames,” *Halon Options Technical Working Conference*; Apr 30 - May 2, 2002, Albuquerque, NM., submitted.

** denotes a peer-reviewed, archival publication.

3. Detailed Description of the Project

3.1 Background

Production of the effective and widely used brominated fire suppressant CF_3Br (Halon 1301) and similar compounds has been halted because of their deleterious effects on stratospheric ozone [2]. While short term replacements have been suggested [3-5], they are much less effective than CF_3Br, and a better agent is desired. Recent attention has focused on phosphorus [6-9]and metal species [10-12]. The reasons these agents have attracted interest is because they are up to one hundred times more effective than CF_3Br at reducing the flame speed of hydrocarbon flames when added at low mole fraction. Nonetheless, recent work has shown that while the metal compounds are very effective in both premixed and counterflow diffusion flames at low mole fraction, their marginal effectiveness decreases rapidly above a volume fraction of a few hundred μL/L[1]. The compounds used for the initial tests of the effectiveness of metal compounds are also highly toxic. If some means could be developed to use non-toxic forms of the active element, very effective fire suppressants may be possible. For example, metal species could be effective additives to fire suppressant blends for uninhabited spaces [13].

The goal of the present project, as originally conceived, was to: 1.) determine if other metals experience the same super-effectiveness that $Fe(CO)_5$ and ferrocene showed; 2.) determine if the loss of effectiveness was specific to iron or common to other super-effective agents; 3.) explore ways of overcoming the loss of effectiveness, and 4.) determine if non-toxic forms of the active species could be identified. As the project unfolded, however, we discovered that effectiveness of these super agents in flames resembling fires (e.g., cup-burner type co-flow diffusion flames) was found to be much less than expected based on the results in the premixed and counterflow diffusion flames [14]. An additional—actually a crucial—goal of the project then became to understand the reasons for the poor performance of these agents in the cup burner. Essentially, this last goal was to investigate the flame parameters that lead to the loss of effectiveness of these otherwise powerful inhibitors when used in more practical flames (such as the cup burner).

The approaches taken to accomplish these goals include experimental measurements of the efficiency of metallic agents added to premixed, counterflow diffusion, and cup-burner flames, as well as numerical modeling of the flame structure in all three flame types. Premixed flame speed measurements were used as initial screening tests for new metallic species (which were added as organometallic agents) [12]. These tests determined the potential of the agents for reducing the overall reaction rate in a flame at low mole fraction, and also provided insight into the condensation behavior of the metal's intermediate species as the mole fraction was increased. The premixed flame tests provided comparison of the new metals with iron, both at high and low mole fraction, and allowed an improved understanding of the parameters important in the loss of effectiveness due to condensation. Analyses of the results of numerical calculations of the flame structure of the inhibited flames (using a gas-phase only model), together with calculations of the equilibrium thermodynamics of the reactant mixtures, were then used to understand the reasons for the difference in effectiveness of tin, iron, and manganese in these flames. Further, we

---

[1] Note that μL/L is equivalent to ppm by volume

sought to determine if blends of metals (each kept below their condensation point) could help to overcome the loss of effectiveness experienced by iron when added alone. The premixed flames served as an initial test bed for those experiments.

In addition to identifying possible new metals with superior performance as compared to iron, it was desired to identify non-toxic forms of the metals. One approach for accomplishing that goal is to add the metals (in a non-toxic form) as additives dissolved in water droplets, which are then applied to the flame. These tests were conducted primarily to provide a test procedure for assessing the performance of the metals. They have the additional benefit in that water with additives might be used directly in some application other than aircraft, where freezing is not a concern. In the test procedure, the additives were dissolved in water, which was then fed to an ultrasonic droplet generator that produced a nearly mono-dispersed droplet spray, which was added to the flame [15]. Both premixed and counterflow diffusion flames were used, providing large differences in both flame structure and droplet residence time. To understand system performance and compare the results with similar tests from those in the literature, initial tests were performed with alkali metal compounds (NaOH, KOH, and NaCl) added to water. Of course, tests with the latter of these are useful in their own right, since these simple alkali metal salts are potential practical additives to water. After the tests with water and water/agent solutions of alkali metals, tests were also performed for ferric chloride.

The final task of the project was to understand the reasons for the poor performance of $Fe(CO)_5$ in the cup burner. First, we conducted cup-burner extinction tests in which CO_2 was added to the air stream of cup-burner flames of methane. The organometallic agent was then added, and the reduction in the amount of CO_2 required for extinction was measured [1]. To clearly illustrate any similarities in behavior of the agents in cup-burner flames to that in premixed or counterflow diffusion flames, these experiments were conducted over a range of mole fraction of the metallic inhibitor. Also, the experiments were conducted for several organometallic agents with different efficiencies and condensation behaviors. The reason for the loss of effectiveness of the cup-burner flames was believed to be condensation of oxides and hydroxides. In previous work, we showed that loss of effectiveness in both premixed and counterflow diffusion flames was due to condensation of metal-containing species, and the subsequent isolation of the active moieties away from the regions of high H-atom mole fraction (where the metal intermediates need to be for efficient chemical inhibition). Hence, we also made laser-scattering measurements of the particles in the 3-D flow field above cup-burner flames with $Fe(CO)_5$ added to the air stream [14,16]. Finally, numerical modeling of the particle trajectories in cup-burner flames with small particles seed with the inlet gases helped to illustrate the effects of the flow field drag, and thermophoretic forces. The results of the particle measurements in the cup-burner flames arc then interpreted. Since much of that discussion relies heavily on the insight gained from previous measurements and calculations for premixed and counterflow diffusion flames, background on those findings and new analyses are presented to support our subsequent discussion for the present cup-burner flames measurements and calculations.

3.2 Inhibition by Other Organometallics: Tin and Manganese

Premixed flames are an excellent test method for determining the effect of a chemical inhibitor on flame chemistry. The premixed burning velocity is a fundamental parameter describing the overall reaction rate, heat release, and heat and mass transport in the flame. Of particular convenience, compared to other flames, is the fact that the inhibitor reaches the reaction zone by convection, so that the amount which enters is unambiguous. The experiments are rapid and relatively straightforward, allowing tests over a wide range of conditions. The flames are easily modeled with existing numerical codes, so that detailed information on the mechanism of chemical inhibition can be determined. There is also a very large data base on the effectiveness of other chemical and inert inhibitors in premixed flames for comparison. Consequently, we used premixed flames for the first tests of new metallic inhibitors as described below.

3.2.1. Introduction

Iron pentacarbonyl has been shown to be up to two orders of magnitude more effective than CF_3Br as a flame inhibitor; however, it loses its effectiveness due to condensation of the active species to particles. Consequently, it is of interest to determine if other metals cause similar strong flame inhibition while not suffering from the loss of effectiveness. Since manganese- and tin-containing species have higher vapor pressures than those of iron species, they are potential additives for fire suppression. The present work seeks to determine the gas-phase flame inhibition properties of tin and manganese through experiments and modeling of their influence on the premixed burning velocity of methaneeair flames.

Metals have great potential as flame inhibitors since it is well known that they catalyze the recombination of radicals in the post combustion region of hydrogen – air flames [17-20]. For example, Bulewicz and Padley [17] demonstrated that metallic compounds of Cr, Mn, Sn, U, Mg and Ba accelerate hydrogen atom recombination at ppm levels. Nonetheless, careful studies of flame inhibition, with the goal of assessing the metals' effects on the overall reaction rate, are limited. Tin compounds are used as fire retardant additives for polymers, and to reduce smoke and CO formation [2 1,221. The mechanism of flame inhibition has been attributed to both the promotion of condensed phase char and gas-phase flame inhibition [22,23]. Lask and Wagner [24] found $SnCl_4$ to be about 1/34 as effective as $Fe(CO)_5$ at reducing the burning velocity of premixed ti-hexane–air flames by 30 %, and Miller et al. [25] found it to be about 2/3 as effective as $Fe(CO)_5$ at reducing the flame speed of hydrogen-air flames by 80 %. Miller [26] measured the amount of inhibitor required to lift-off a premixed $CH_4/O_2/N_2$ flat flame at low pressure, and found that tetramethyltin ($Sn(CH_3)_4$, TMT) and $SnCl_4$ required a mole fraction of 1.7 % and 1.1 %, respectively; whereas $Fe(CO)_5$ and Br_2 required 0.23 % and 2.3 %. Morrison and Scheller [27] investigated the effect of twenty flame inhibitors on the ignition of hydrocarbon mixtures by hot wires, and found that $SnCl_4$ was the most effective inhibitor tested for increasing the ignition temperature; whereas the powerful flame inhibitors CrO_2Cl_2 and $Fe(CO)_5$ had no effect on the ignition temperature. As a result of these studies, tin tetrachloride $SnCl_4$ was recommended as compound deserving further study [28].

The effects of manganese compounds on flames has also been studied. Vanpee and Shirodkar [29] investigated the influence of many metal chlorides and metal acetates and acetylacetonates on the limiting oxygen index at extinction in a partially premixed counterflow pool burner of ethanol and air. In their experiment, the inhibitor was dissolved in ethanol, which was aspirated into the air stream. They found manganese acetylacctonate to be more effective than acetylacetonates of iron or chromium. Westblom et al. [30] analyzed the consequence of trace amounts of methylcyclopentadienylmanganese tricarbonyl ($CH_3C_5H_4Mn(CO)_3$, MMT) on the flame structure of a premixed propane - air flame at 5.33 kPa, but found no measurable effect. They suggested a kinetic model for the influence of MMT on those flames [30]. In a review article, Howard and Kausch [21] reported that manganese-containing compounds are among the most effective soot-reducing fuel additives. Finally, MMT is a known antiknock agent for gasoline [31], and Tapscott et al. [32] recently suggested manganese compounds as agents for further consideration in studies of fire suppression performance.

In this section of the report we present data on flame inhition by manganese- and tin-containing compounds. The additive influence was analyzed through the effects on the laminar burning velocity of methane-air mixtures for different equivalence ratios and oxygen mole fractions. The kinetic mechanisms of flame inhibition were analyzed by comparing simulation results with experimental data. The relative inhibition efficiencies of TMT, MMT, $Fe(CO)_5$, and CF_3Br were deduced and analyzed. While the manganese and tin compounds tested are too toxic to be used directly as fire suppressants, they provide convenient means for introducing Mn and Sn to a flame, so that the inhibition mechanisms of these elements can be studied.

3.2.2. Experimental Apparatus

The laminar flame speed S_L provides a measure of an agent's reduction of the global reaction rate. While good techniques exist which allow measurement of burning velocity under conditions of controlled stretch rates [33], they require seeding with particles for determination of the local gas velocity. Since the presence of particles would influence the condensation rates of our metallic species, we instead employed the total area method with a Bunsen-type flame [34]. The experimental arrangement, described in detail previously [11,35-38], has been modified to accommodate new evaporators for TMT and MMT. A Mache-Hebra nozzle burner (1.0 cm ± 0.05 cm diameter) produces a premixed Bunsen-type flame about 1.3 cm tall with a straight-sided schlieren image that is captured by a video frame-grabber board in a PC. Digital mass flow controllers hold the oxygen mole fraction in the oxidizer stream $X_{O2,ox}$, the equivalence ratio ϕ, and the flame height constant while maintaining the inlet mole fraction of the inhibitor (X_{in}) at the desired value. The average burning velocity is determined from the reactant flows and the schlieren image using the total area method. The fuel gas is methane (Matheson' UHP, 99.9 %), and the oxidizer stream consists of nitrogen (boil-off from liquid N_2) and oxygen (MG Industries, H_2O less than 50 µL/L, and total hydrocarbons less than 5 µL/L). The inhibitors used are $Fe(CO)_5$ (Aldrich), TMT (Alfa Aesar), MMT (Alfa Aesar), CF_3Br (Great Lakes), N_2 (boil-off). and CO_2 (Airgas). The catalytic agents are liquids at laboratory conditions. Since they are required in low mole fraction, they are added to the flame in gaseous form rather than as droplets. The $Fe(CO)_5$ is added to the carrier gas using a two-stage saturator in an ice bath, described previously [36]. Nitrogen is the carrier gas for all agents. The TMT was added using an identical two-stage saturator, with a volume of liquid TMT in each stage greater than 50 cm' for all tests. The ice bath was maintained at (0 ± 0.2) °C with a maximum carrier gas flow 0.40 L/min. Because of the toxicity of the agents, the $Fe(CO)_5$ and TMT saturators. as well as the premixed flame burner, were located in fume hoods. For the MMT, the saturator had three

---

[2] Certain commercial equipment, instruments, or materials are identified in this paper to adequately specify the procedure. Such identification does not imply recommendation or endorsement by the National Institute of Standards and Technology, nor does it imply that the materials or equipment are necessarily the best available for the intended use.

stages, each 20 cm long, 2.36 cm I.D. stainless steel tube, and the entire apparatus was submerged in a controlled temperature bath (Neslab), and vented. The bath temperature was typically (79.2 ± 0.1) °C, and the carrier gas flow for this saturator was always <0.5 L/min. The mole fraction of the organometallic inhibitors in the air stream was calculated based on the measured air flow, measured carrier gas flow, and vapor pressure of the agent at the bath temperature, assuming saturated carrier gas. The parameters in the Antoine equation, $\log_{10}(P)=A-B/(T+C)$ (T in "C, P in bar), are (A,B,C): (6.77273, 4.0932, 7.2283), (1258.22, 1286.16, 1882), and (21 1.587, 235.846, 200) for $Fe(CO)_5$ [39], TMT [40], and MMT [41], respectively. Since the vapor pressure of MMT is much lower than that of the other agents, experiments with MMT were conducted at a slightly elevated temperature, with the transfer lines and inlet gases maintained at (80 ± 3) "C and the burner tube maintained at (80 ± 1) °C. For the experiments with TMT and $Fe(CO)_5$, the inlet gas temperature Ti, was (294.2 ± 1) K. Although the absolute value of the burning velocity is quite sensitive to the inlet temperature, comparisons of agent performance across this range of differing gas inlet temperatures is valid, since the *reduction* in the *normalized* burning velocity with agent addition is relatively insensitive in T,,,. For example, calculations for inhibition by TMT (discussed below), and calculations and experiments with CO_2 (unpublished data of ref. [11]) show that changing the inlet gas temperature from 294 K to 353 K provides nearly identical curves of normalized burning velocity versus inhibitor mole fraction, differing from each other by less than 2 % for the two inlet temperatures.

Tests were performed for a range of equivalence ratio and oxygen mole fraction in the oxidizer stream $X_{O_2,ox}$. The agent mole fraction is calculated relative to the total reactant flow. The test conditions are listed in Table 1. Note that while the inlet temperature for the $Fe(CO)_5$ and TMT experiments was 294 K, the experimental and numerically calculated burning velocities in the table have been converted to equivalent values at 298 K to facilitate comparison with other values available in the literature.

The burning velocity in Bunsen-type flames is known to vary at the tip and base of the flame; however, these effects are most important over a small portion of the flame. We have taken several steps to minimize the influence of curvature and stretch on interpretation of the action of the chemical inhibitor. The nozzle burner produces visible and schlieren images which are very closely parallel. For the flame area, we use the schlieren image, which is maintained at a constant size (1.3 cm tall) for all tests. In order to reduce the error caused by flame curvature and stretch, we present the burning velocity of inhibited flames as a normalized parameter: the burning velocity of the inhibited flame divided by the burning velocity of the uninhibited flame. Also, we limit our interpretation of the data to inhibitor loading which produce less than 40 % reduction in flame speed.

Table 1 - Uninhibited laminar burning velocities S_L and adiabatic flame temperature T_{AFT} from 1-D planar numerical calculations, together with the average burning velocity measured in the Bunsen-type flames, for the initial conditions of the experiments.

ϕ	$X_{O_2,ox}$	T_{in} K	T_{AFT} K	$S_{L,calc.}$ cm/s	$S_{L,exp}$ cm/s
TMT					
0.9	0.21	298	2159	35.3	33.9 ± 1.3
1.0	“	“	2235	39.6	38.0 ± 2.3
1.1	“	“	2193	39.8	38.0 ± 1.5
1.0	0.20	“	2185	34.7	33.6 ± 1.4
“	0.244	“	2377	57.0	58.0 ± 3.4
MMT					
0.9	0.21	353	2177	48.0	47.2 ± 1.5
1.0	“		2264	53.2	52.9 ± 2.9
1.1	“		2251	53.6	52.8 ± 2.0
1.0	0.19	“	2167	41.3	39.9 ± 1.6
“	0.2	“	2220	47.4	45.5 ± 1.7
“	0.244	“	2396	74.3	74.7 ± 4.1
MMT and $Fe(CO)_5$					
1.0	0.244	353	2396	74.3	75.9 ± 4.9

Determination of the uncertainties in the experimental data using the present apparatus has been described in detail previously [36]. For the present data, the uncertainty (expanded uncertainties with a coverage factor of 2) in the normalized burning velocity are less than ± 5 % for all cases. The uncertainty in the equivalence ratio is 1.4 %. Neglecting the uncertainties (unspecified) in the vapor pressure correlation for $Fe(CO)_5$, TMT, and MMT. uncertainties in the bath temperature, ambient pressure and carrier gas flow rate yield an inhibitor mole fraction uncertainty of 6.5 %.

3.2.3. Kinetic Mechanisms and Numerical Modeling

There are few data on the chemical kinetics of tin compounds at flame temperatures, although kinetics studies of tin have been conducted for chemical vapor deposition. Studies with hydrogen-oxygen-nitrogen flames by Bulewicz and Padley [42] indicate that tin is present as Sn, SnO, and SnOH, with SnO overwhelmingly predominant. Recent spectroscopic data also indicate that tin is presents in flames as Sn, SnO, and SnOH [43], with SnO accounting for approximately 97 % by volume of all tin species.

The present kinetic model for flame inhibition by tin compounds contains reactions of the species Sn, SnO_2, SnO, SnH and SnOH. The reaction set is based on the consideration of possible reactions of tin-containing species with the radical pool and with the main species of methane combustion. The mechanism, listed in Table 2, consists of 37 reactions of tin-containing species. Rate constants were obtained from the literature when available, or otherwise estimated using empirical procedures and analogies with similar reactions. The reverse rates of the reactions in Table 2 are calculated from the forward rate and the equilibrium constant. It was assumed that tin (and manganese) species are non-reactive with hydrocarbon molecules. In the model development, estimates of rate constants were first made, and then the rates of the most important reactions were adjusted (based on sensitivity analysis) to provide agreement with the experimental results. The decomposition of TMT was described by the overall step listed in Table 2, but using the rate constant for the reaction $Sn(CH_3)_4 \rightarrow Sn(CH_3)_3 + CH_3$ [44]. Enthalpies of formation for the tin-containing (and manganese-containing) species are presented in Table 3. Enthalpies of formation for SnOH and SnH were estimated based on bond energies from refs. [42,45].

The kinetic mechanism for studying the influence of manganese additives in premixed methane-air flames is presented in Table 4. The list of possible Mn-containing species participating in inhibition reactions includes Mn, MnH, MnO, MnOOH, MnHOH, MnOH, MnO, MnO_2 and $Mn(OH)_2$. All species except MnH and MnHOH were considered in the mechanism of Smith [46]. The role of MnOH and MnO in radical recombination was discussed by Bulewitz and Padley [17], and the species MnO and Mn were recently measured in a low pressure propane flame doped by MMT [30]. Hildenbrand and Lau [47] used mass spectrometry to identify the species MnO_2, MnOH, and $Mn(OH)_2$. We included the species MnH in the model since equilibrium calculations showed it to be present in significant quantities in MMT-inhibited flames. Transport parameters of tin- and manganese-containing species were estimated through analogy with similar metallic species, or based on molecular weight correlations for similar species.

For the manganese inhibition reaction set, we generated a list of approximately 160 reactions of Mn-containing species with the radical pool and with the main species of methane combustion. This list was reduced to 61 reactions based on thermochemical considerations and preliminary calculations. For the decomposition of MMT, we adopt the overall description suggested in ref. [30] and ref. [46], and use their rate constants for the Mn-species reactions whenever possible. Rate constants for the remaining reactions were estimated by analogy and based on thermochemical estimates. The main assumptions are the formation of MnO_2 through the reaction of Mn atom with oxygen molecule and the formation of $Mn(OH)_2$ via reaction of MnO with water (both by analogy to reactions of iron-containing species [48]).

Table 2 – Kinetic mechanism for tin inhibition of premised methane-air flames.

($k = \mathbf{A}\ T^{b} \exp(-E/RT)$, mole,s,cm,kJ)

No.	REACTION	A	b	E	Reference
1.	$SnC_4H_{12} \Rightarrow Sn+C_2H_6+C_2H_6$	7.94E+13	0.0	230.	[44]
2.	$Sn+H+M = SnH+M$	1.00E+15	0.0	0.0	*e*
3.	$Sn+OH+M = SnOH+M$	5.36E+18	-0.45	0.0	*
4.	$Sn+OH = SnO+H$	1.00E+13	0.0	27.2	*e*
5.	$Sn+O+M = SnO+M$	1.00E+17	0.0	0.0	*e*
6.	$Sn+O_2 = SnO+O$	3.07E11	0.79	3.63	[49]
7.	$Sn+O_2\ (+M) = SnO_2\ (+M)$	2.00E+13	0.0	0.0	*e*
	Low pressure limit:	1.5E+18	0.0	16.7	
8.	$Sn+HCO = SnH+CO$	3.00E+13	0.0	0.0	*e*
9.	$Sn+CH_3O = SnO+CH_3$	2.00E+13	0.0	0.0	E
10.	$Sn+CO_2 = SnO+CO$	1.39E+14	0.0	75.6	[49]
11.	$Sn+HO_2 = SnO+OH$	1.00E+13	0.0	0.0	*e*
12.	$SnO+H+M = SnOH+M$	5.50E+17	0.0	0.0	*e*
13.	$SnO+O+M = SnO_2+M$	1.00E+20	-1.0	0.0	*e*
14.	$SnO+HCO = SnOH+CO$	9.30E+13	0.0	0.0	*e*
15.	$SnO+HO_2 = SnOH+O_2$	3.00E+13	0.0	29.3	*e*
16.	$SnO_2+H = SnO+OH$	1.00E+14	0.0	8.37	*e*
17.	$SnO_2+OH = SnOH+O_2$	3.00E+12	0.0	31.4	*e*
18.	$SnO_2+OH = SnO+HO_2$	3.00E+12	0.0	46.0	*e*
19.	$SnO_2+O = SnO+O_2$	3.00E+13	0.0	8.37	*e*
20.	$SnO_2+CH3 = SnO+CH_3O$	3.00E+12	0.0	18.8	*e*
21.	$SnO_2+CO = SnO+CO_2$	2.00E+12	0.0	20.9	*e*
22.	$SnOH+H = Sn+H_2O$	1.20E+12	0.0	12.6	*e*
23.	$SnOH+H = SnO+H_2$	7.10E+13	0.0	4.18	*e*
24.	$SnOH+OH = SnO+H_2O$	6.30E+13	0.0	0.0	*e*
25.	$SnOH+O = SnO+OH$	3.00E+13	0.0	0.0	*e*
26.	$SnOH+O = SnO_2+H$	5.00E+12	0.0	37.7	*e*
27.	$SnOH+CH_3 = SnO+CH_4$	2.00E+13	0.0	4.18	*e*
28.	$SnH+H = Sn+H_2$	5.00E+13	0.0	4.18	e
29.	$SnH+OH = Sn+H_2O$	3.00E+13	0.0	0.0	*e*
30.	$SnH+OH = SnOH+H$	5.00E+12	0.0	20.9	*e*
31.	$SnH+O+M = SnOH+M$	1.00E+15	0.0	0.0	*e*
32.	$SnH+O = Sn+OH$	5.00E+13	0.0	4.18	*e*
33.	$SnH+O = SnO+H$	8.00E+12	0.0	4.18	*e*
34.	$SnH+CH_3 = CH_4+Sn$	5.00E+13	0.0	4.18	*e*
35.	$SnH+HCO = Sn+CH_2O$	2.00E+12	0.0	18.8	*e*
36.	$SnH+O_2 = SnO+OH$	3.00E+12	0.0	29.3	*e*

e Estimates.

* By analogy with reactions of K species in ref. [SO]

Table 3 – Thermodynamic properties for tin- and manganese-containing species (298.15 K).

Species	Enthalpy of Formation kJ/mol	Entropy J/(mol K)	Heat Capacity J/(mol K)	Ref.
Mn	283.6	173.6	20.8	[51]
MnO	161.7	236.0	31.7	[51]
MnO_2	23.01	269.3	42.2	[51]
MnOH	17.32	250.3	45.8	[51]
$Mn(OH)_2$	-373.2	291.2	67.1	e, [46]
MnOOH	-116.3	283.3	53.9	e, [46]
MnH	197.9	213.6	29.6	[51]
MMT	-439.3	401.7	149.9	[46]
Sn	301.2	168.4	21.3	[51]
SnO	21.91	232.1	31.8	[51]
SnO_2	11.69	251.5	49.5	[51]
SnOH	-15.06	244.8	46.0	*e*, [42]
SnH	268.2	214.7	29.7	*e*, [45]
$Sn(CH_3)_4$	-17.70	361.2	137.8	[52], [53]
Sn_2	425.4	267.2	42.1	[51]

e Estimation.

Table 4 - Kinetic mechanism for manganese inhibition of premixed methane-air flames.

($k = A\ T^{b} \exp(-E/RT)$, mole,cm,s,kJ)

No.	REACTION	A	b	E	Reference
1.	$Mn+H+M = MnH+M$	1.00E+15	0.0	0.0	*e*
2.	$Mn+OH+M = MnOH+M$	8.00E+22	-2.2	0.0	[46]
3.	$Mn+O+M = MnO+M$	1.00E+15	0.0	0.0	*e*
4.	$Mn+O_2 = MnO+O$	2.50E+14	0.0	125.5	[46]
5.	$Mn+O_2\ (+M) = MnO_2\ (+M)$	2.00E+13	0.0	0.0	*e*
	Low pressure limit:	1.5000E+18	0.0	12.6	
6.	$Mn+HCO = MnH+CO$	3.00E+13	0.0	0.0	*e*
7.	$MnO+H+M = MnOH+M$	7.00E+15	0.0	0.0	[46]
8.	$MnO+O+M = MnO_2+M$	2.00E+19	-1.0	0.0	[46]
9.	$MnO+H = Mn+OH$	1.00E+14	0.0	16.7	***e***
10.	$MnO+OH+M = MnOOH+M$	3.00E+17	0.0	0.0	*e*
11.	$MnO+CH_3 = Mn+CH_3O$	1.00E+14	0.0	29.3	*e*
12.	$MnO+H_2 = Mn+H_2O$	3.00E+12	0.0	20.9	[54]
13.	$MnO+H_2O = MnO_2H_2$	5.40E+12	0.0	0.0	[54]
14.	$MnO+CO = Mn+CO_2$	3.00E+11	0.0	0.0	[46]
15.	$MnO+HCO = MnOH+CO$	2.40E+13	0.0	0.0	[46]
16.	$MnO+CH_2OH = MnOH+CH_2O$	2.40E+13	0.0	0.0	[46]
17.	$MnO_2+H+M = MnOOH+M$	2.00E+22	-1.5	0.0	[46]
18.	$MnO_2+H = MnO+OH$	1.00E+14	0.0	29.3	*e*
19.	$MnO_2+OH = MnOH+O_2$	3.00E+12	0.0	29.3	*e*
20.	$MnO_2+O = MnO+O_2$	5.00E+13	0.0	8.37	*e*
21.	$MnO_2+CO = MnO+CO_2$	2.00E+12	0.0	20.9	e
22.	$MnOH+H = Mn+H_2O$	1.20E+12	0.0	2.09	[46]
23.	$MnOH+H = MnO+H_2$	3.00E+13	0.0	4.18	e
24.	$MnOH+OH+M = MnO_2H_2+M$	1.00E+23	-2.0	0.0	[46]
25.	$MnOH+OH = MnO+H_2O$	1.00E+13	0.0	6.28	[46]
26.	$MnOH+O+M = MnOOH+M$	1.00E+18	0.0	0.0	*e*
27.	$MnOH+O = Mn+HO_2$	3.00E+13	0.0	71.1	*e*
28.	$MnOH+O = MnO+OH$	3.00E+13	0.0	0.0	[46]
29.	$MnOH+O = MnO_2+H$	5.00E+12	0.0	37.7	*e*
30.	$MnOH+CH_3 = MnO+CH_4$	2.00E+13	0.0	12.6	*e*
31.	$MnOOH+H+M = MnO_2H_2+M$	1.00E+16	0.0	0.0	*e*
32.	$MnOOH+H = MnO+H_2O$	2.00E+13	0.0	0.0	e
33.	$MnOOH+H = MnOH+OH$	3.00E+13	0.0	20.9	*e*
34.	$MnOOH+H = MnO_2+H_2$	1.00E+13	0.0	16.7	*e*
35.	$MnOOH+OH = MnO_2+H_2O$	6.00E+12	0.0	6.28	[46]
36.	$MnOOH+O = MnOH+O_2$	2.00E+13	0.0	10.5	*e*
37.	$MnOOH+O = MnO+HO_2$	3.00E+12	0.0	66.9	*e*
38.	$MnOOH+O = MnO_2+OH$	3.00E+13	0.0	18.8	*e*

39.	$MnOOH+CH_3 = MnO+CH_3OH$	3.00E+12	0.0	31.4	e
40.	$MnOOH+CH_3 = MnOH+CH_3O$	1.00E+13	0.0	46.0	*e*
41.	$MnOOH+CO = MnOH+CO_2$	2.00E+12	0.0	20.9	e
42.	$MnO_2H_2+H = MnOH+H_2O$	6.60E+13	0.0	4.18	*e*
43.	$MnO_2H_2+H = MnOOH+H_2$	5.00E+13	0.0	79.5	*e*
44.	$MnO_2H_2+OH = MnOOH+H_2O$	1.00E+13	0.0	37.7	*e*
45.	$MnO_2H_2+O = MnOOH+OH$	2.00E+13	0.0	83.7	***e***
46.	$MnO_2H_2+CH_3 = MnOOH+CH_4$	1.00E+13	0.0	87.9	*e*
47.	$MnH+H = Mn+H_2$	5.00E+13	0.0	12.6	e
48.	$MnH+OH = Mn+H_2O$	1.00E+14	0.0	0.0	*e*
49.	$MnH+O+M = MnOH+M$	1.00E+15	0.0	0.0	*e*
50.	$MnH+O = Mn+OH$	1.00E+14	0.0	8.37	*e*
51.	$MnH+CH_3 = CH_4+Mn$	1.00E+14	0.0	8.37	***e***
52.	$MnH+O_2+M = MnOOH+M$	1.00E+16	0.0	0.0	***e***

e Estimates.

Kinetic models for highly effective flame inhibitors can be considered to consist of two sub-models. The first sub-model includes reactions for the agent decomposition and formation of the active inhibiting species, and the second includes the inhibition reactions. In previous work, it has been shown that for the phosphorus-containing compound DMMP and for ferrocene, the decomposition reactions have a small influence on the predicted inhibitor efficiency as long as the overall activation energy of decomposition is less than 250-335 kJ/mol [11,55]. In the present work, this was also found to be true for TMT and MMT decomposition.

The laboratory flames inhibited by TMT and MMT were numerically modeled as one-dimensional freely-propagating flames. Solutions were obtained using the Sandia flame code *Premix* [56], and the *Chemkin* [57] and transport property [58] subroutines (solutions were obtained for values of GRAD and CURV of 0.17 and 0.25 in PREMIX). The kinetic mechanism for methane combustion was GRIMech 3.0 [59], with the nitrogen chemistry removed. The methane sub-mechanism contains 36 species and 219 reactions. It should be emphasized that the reaction mechanisms used for the present calculations for flames with manganese or tin compounds should be considered only as a starting point. Numerous changes to both the rates and the reactions incorporated may be made once a variety of experimental and theoretical data are available for testing the mechanism. Note also that the calculations are for 1-D planar flames, while the experiments determine the average flame speed of Bunsen-type flames which can be influenced by curvature and stretch. To minimize these effects, both the experimental and calculated data are presented as normalized flame speed reduction.

3.2.4. Results

3.2.4.1. Observations

The appearance of the flames with added organometallic inhibitors is shown in Figure 1. Flames with iron pentacarbonyl are bright orange, with tetramethyltin they are bright pale blue, and with MMT, yellow-green. The intensity of the visible emission increases with inhibitor mole fraction. As the loading of metallic inhibitor increases, there becomes visible a luminous outer shroud as seen clearly in the last two images on the right in Figure 1. We believe these are regions of high particle concentration from inhibitor condensation, leading to broad-band black body radiation, visible here in the orange part of the spectrum. For the TMT-inhibited flames, a white-colored powder (presumably tin oxide) formed on the rim of the quartz burner tube during the tests, especially at high TMT loading. This deposit was removed between collection of each data point. For MMT and $Fe(CO)_5$, a dark red or an orange deposit was formed, respectively. The rate of deposition for these inhibitors, however, was much lower than for the TMT, which was added to the flames at mole fractions about ten times higher.

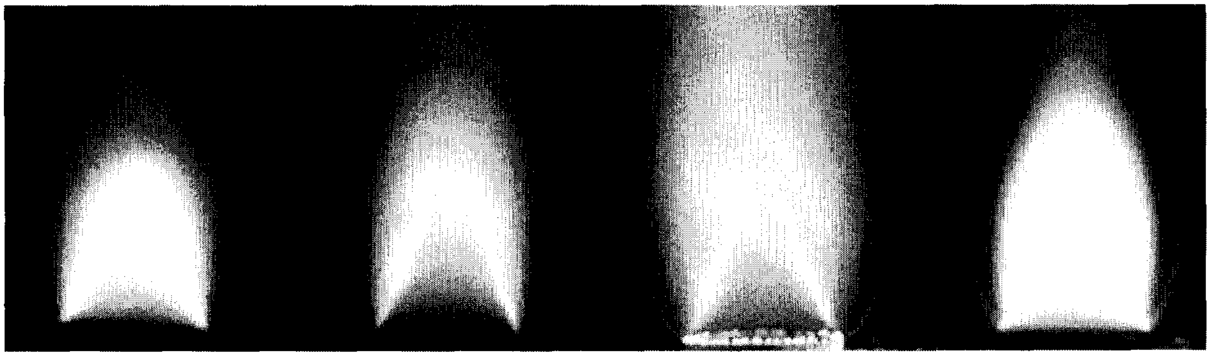

Figure 1 - Visible image of methane-air premixed flame (from left to right: no inhibitor, 50 µL/L of $Fe(CO)_5$, 4000 µL/L of TMT, and 400 µL/L of MMT).

3.2.4.2. Inhibition by Tetramethyltin

Figure 2 shows the relative burning velocity reduction with addition of TMT to methane-air flames ($X_{O_2,ox}$ =0.21) for values of equivalence ratio of 0.9, 1.0, and 1.1. The dotted lines are curve fits to the experimental data, and the solid lines are the results of the numerical calculations described above (and discussed below). Data are plotted as normalized burning velocity, which is the burning velocity of the inhibited flame divided by the value for the same flame in the absence of inhibitor. The calculated and experimental burning velocities, along with the calculated adiabatic flame temperatures of the uninhibited flames used for the normalization are listed in Table 1. For the uninhibited flames, the experimentally determined average burning velocities for the Bunsen-type flames are within about 4 % of the calculated values for 1-D planar flames. In Figure 2 (as well as 3,4,5, and 7 described below), the last data point shown represents the highest volume fraction of inhibitor for which flames could be stabilized on the present burner (i.e., they extinguished at higher volume fractions). The experimental results in Figure 2 demonstrate that for stoichiometric flames, 3000 µL/L of TMT reduces the flame speed by about 41 %, which is about a factor of two better than CF_3Br. The data also show that, unlike $Fe(CO)_5$, the richer flames are inhibited more strongly by TMT than the leaner flames. (Additional numerical tests with SnO as the inhibitor showed that the poorer inhibition of lean flames was due to the fuel effect from the hydrocarbon portion of the relatively large amounts of $Sn(CH_3)_4$ added to the flames.)

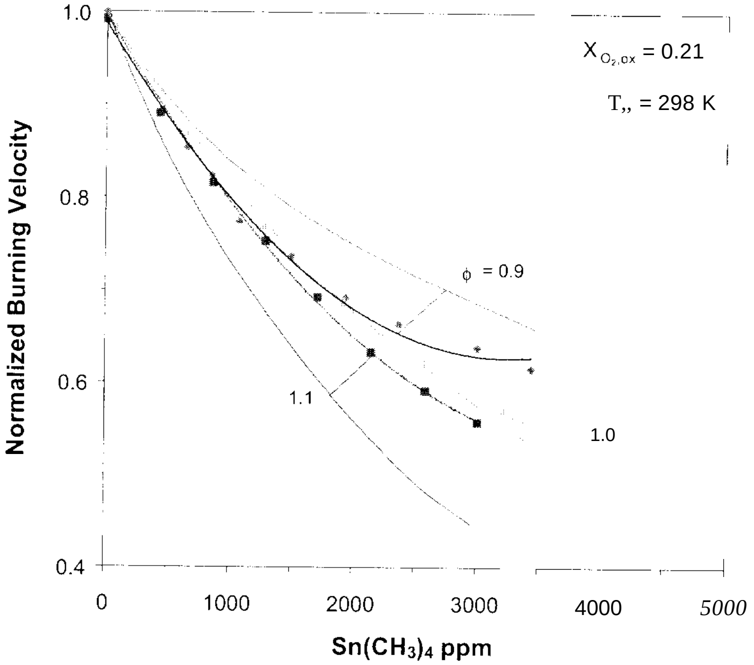

Figure 2 – Normalized burning velocity of premixed $CH_4/O_2/N_2$ flames inhibited by TMT with $X_{O2,ox}$=0.21 and ϕ=0.9, 1.0, and 1.1 (dotted lines: curve fits to data; solid lines: numerical predictions).

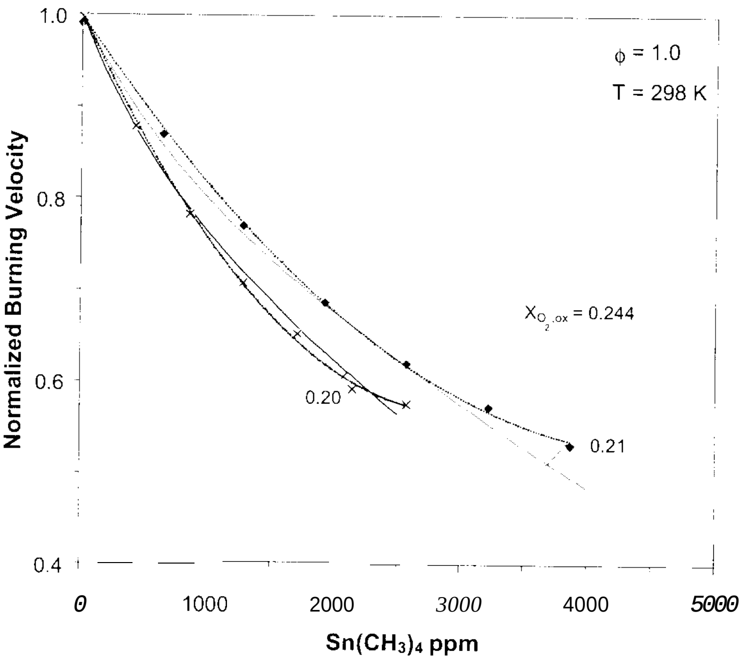

Figure 3 – Normalized burning velocity of premixed $CH_4/O_2/N_2$ flames inhibited by TMT, with φ=1.0 and $X_{O2,ox}$=0.20. 0.21, and 0.244 (dotted lines: curve fits to the data; solid lines: numerical predictions).

As described below, the burning velocity reduction caused by tin species is most sensitive to the rates of the reactions: $SnO + H + M \leftrightarrow SnOH + M$, and $SnOH + H \leftrightarrow SnO + H_2$. Consequently, we adjusted the pre-exponential factor in those rates to provide agreement with the experimental results for stoichiometric mixtures of methane with air. Note, however, the relatively high level of the rate constant for the reaction $H + SnO + M \leftrightarrow SnOH + M$. Bulewicz and Padley [17] also found that a high rate was required for this process to provide agreement with their experimental data on hydrogen atom recombination in the products of a hydrogen flames. **As** Figure 2 shows, the numerical model predicts the amount of inhibition well for stoichiometric flames. For rich and lean flames, however, the model over- and under-predicts the burning velocity, respectively. We attempted to adjust the rates of reactions with tin species to improve the model performance for rich and lean flames. For the reaction set considered, we were not able to find reasonable adjustments to the rate constants to provide better agreement.

Figure 3 shows the measured and calculated flame speeds for TMT in stoichiometric flames $X_{O_2,ox}$ equal to 0.20, 0.21, and 0.244. The experimental data and calculations (with adjusted rate constants) show good agreement for the three values of $X_{O_2,ox}$; however, for the hottest flames ($X_{O_2,ox} = 0.244$) the mechanism slightly overpredicts the inhibition at low mole fraction, and underpredicts it for higher mole fraction. The experimental data show that for the slower and cooler flames (e.g., equivalence ratio is 0.9 or 1.0 and $X_{O_2,ox} = 0.20$ or 0.21), the TMT starts to lose its effectiveness above a certain value. For $Fe(CO)_5$ inhibited flames, such behavior was shown to be due to condensation of the iron-containing intermediates [37]).

3.2.4.3. Inhibition by MMT

The premixed flames inhibited by manganese-containing compound MMT were slightly preheated (T,,,= 80 °C). The values of the calculated and experimental uninhibited burning velocities, and the adiabatic flame temperatures are shown in Table 1. The normalized burning velocities of MMT-inhibited flames with variation in equivalence ratio and $X_{O_2,ox}$ are shown in Figure 4 and Figure 5. MMT is seen to be about thirteen times more efficient at flame inhibition than TMT; however, it too starts to lose its effectiveness for tlame speed reductions near 50%. Based on the sensitivity of the burning velocity to the reaction rates, we adjusted the pre-exponential factors of the reactions $Mn(OH)_2 + H \leftrightarrow MnOH + H_2O$, and $MnO + H_2O \leftrightarrow Mn(OH)_2$ to provide agreement with our experimental data for these methane-air flames at $\phi=1.0$. Using the rates shown in Table 4 the model predicts the burning velocity reduction quite well. Nonetheless, for the hottest flames ($X_{O_2,ox} = 0.244$) this mechanism also overpredicts the inhibition slightly at low inhibitor mole fraction, and underpredicts the inhibition somewhat at intermediate mole fractions. Also, this gas phase mechanism does not capture the decrease in inhibitor effectiveness which occurs with increasing inhibitor initial mole fraction, likely a result of condensation of Mn-containing species.

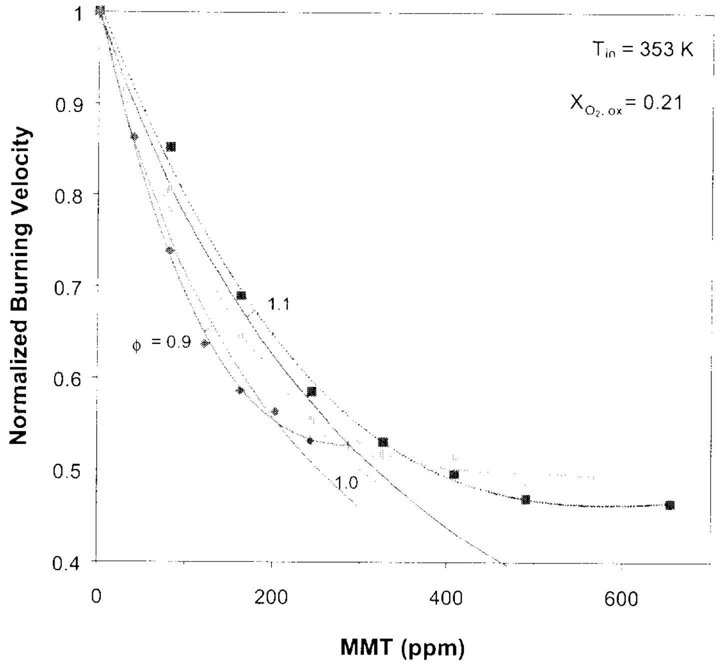

Figure 4 - Normalized burning velocity of premixed $CH_4/O_2/N_2$ flames inhibited by MMT with $X_{O2,ox}$=0.21 and ϕ=0.9, 1.0, and 1.1 (dotted lines: curve fits to data; solid lines: numerical predictions).

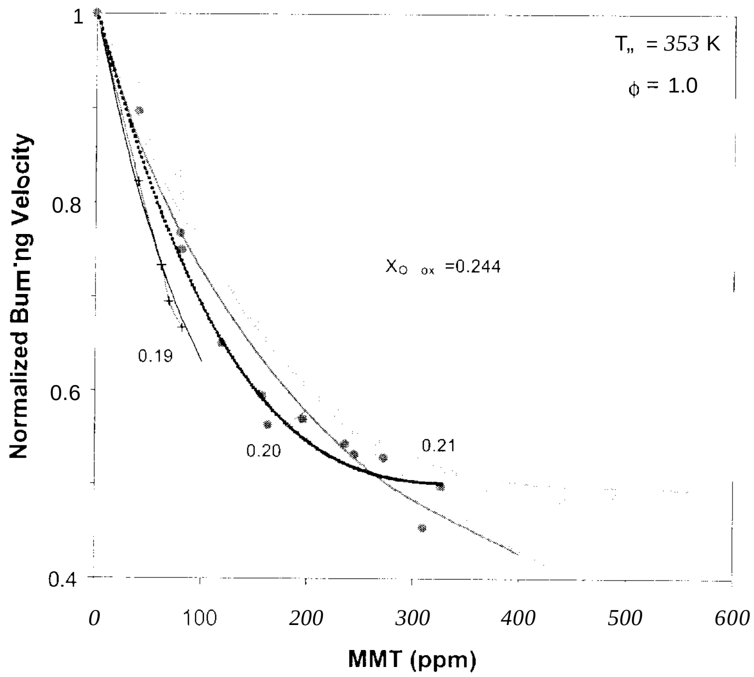

Figure 5 - Normalized burning velocity of premixed $CH_4/O_2/N_2$ flames inhibited by MMT, with phi=1.0 and $X_{O2,ox}$=0.19, 0.20. 0.21, and 0.244 (dotted lines: curve fits to the data; solid lines: numerical Predictions).

3.2.4.4. Comparative Performance of Metals

Figure 6 compares the inhibition effectiveness of $Fe(CO)_5$, MMT, TMT, $SnCl_4$, CF_3Br, and CO_2. The data for $SnCl_4$ inhibition from ref. [24] show tin tetrachloride to be as effective in n-hexane/air flames as TMT is in methane/air flames. Although the experimental data shown for TMT and $SnCl_4$ are not for an elevated inlet temperature of 80 °C, numerical calculations show that the reduction in the *normalized* flame speed caused by TMT addition with T_{in}=298 K differs from that with T_{in}=353 K by less than 1 %. $Fe(CO)_5$ is significantly more effective than any of the other agents, and all of the metal-based inhibitors appear to have greatly reduced effectiveness for burning velocity reductions greater than 50%. If the inhibitor mole fractions are re-scaled in Figure 6 to provide overlap at 30 % reduction in burning velocity, the normalized burning velocity curves of all inhibitors are nearly coincident for flame speed reductions less than 40 % (i.e., the curves are roughly linear up to this amount of normalized flame speed reduction). Such re-scaling of the experimental data shows that at low mole fraction, $Fe(CO)_5$ is about eighty times, MMT forty times, and TMT three times as effective as CF_3Br at reducing the overall reaction rate of stoichiometric, premixed methane-air flames. For flame speed reductions greater than 40 %, the curves for these five agents diverge. As discussed previously [60,61], most inhibitors lose their marginal effectiveness at higher mole fractions, but the decrease in inhibition effectiveness is much more dramatic for the organometallic compounds as was found previously for $Fe(CO)_5$.

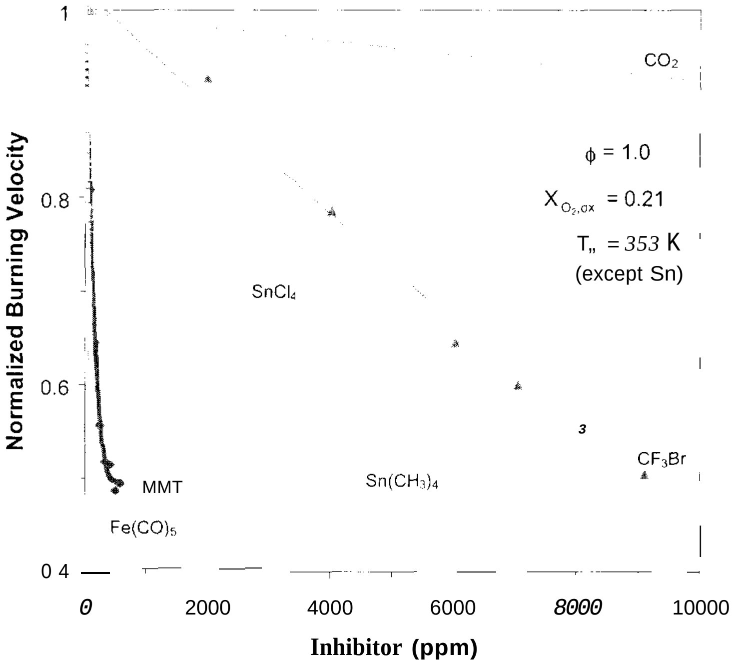

Figure 6 - Normalized burning velocity of premixed $CH_4/O_2/N_2$ flames inhibited by CO_2, CF_3Br, $Sn(CH_3)_4$, $SnCl_4$ [24], MMT, and $Fe(CO)_5$ (T_{in} = 353 K for all data except $Sn(CH_3)_4$ and $SnCl_4$ which are at 298 K). Lines are curve fits to data.

3.2.4.5. Blends of Metals

One approach for overcoming the loss of effectiveness is to add non-condensing amounts of several inhibitors. To test this approach in premixed flames, we performed tests with a blend of MMT and $Fe(CO)_5$, added at a molar ratio of 2:1, respectively. Data for pure MMT, pure $Fe(CO)_5$, and their combination are shown in Figure 7 (T_{in} = 353 K, phi=1.0, and $X_{O_2,ox}$=0.244). The experimental data are represented by the points with a curve fit (dotted line), while the results of the numerical calculations are shown by the solid lines. (The data for the combination of MMT and $Fe(CO)_5$ are plotted as a function of the mole fraction of the abundant agent, MMT). The numerical model, which includes both the reactions of manganese-containing species and the iron-containing species from ref. [48] predicts well the normalized flame speed reduction. As the figure shows, adding 0.5 moles of $Fe(CO)_5$ for each mole of MMT added does provide additional flame speed reduction over that from MMT alone. This is significant since, as discussed previously [37], the loss of effectiveness of the metals at higher concentration could be caused either by condensation of active species, or by the loss of radical population by catalytic recombination. Since the addition of iron to the manganese-inhibited flame causes significant additional inhibition, the *strong* loss of effectiveness in the MMT-inhibited flames is likely due to condensation rather than radical depletion. If the cause was radical depletion, addition of $Fe(CO)_5$ to the flames already inhibited by high amounts of MMT would yield no additional inhibition, since few radicals would be left to recombine. The gas-phase kinetic model captures the *mild* reduction of effectiveness of either agent or their blend acceptably well (for flame speed reductions of less than 40 %).

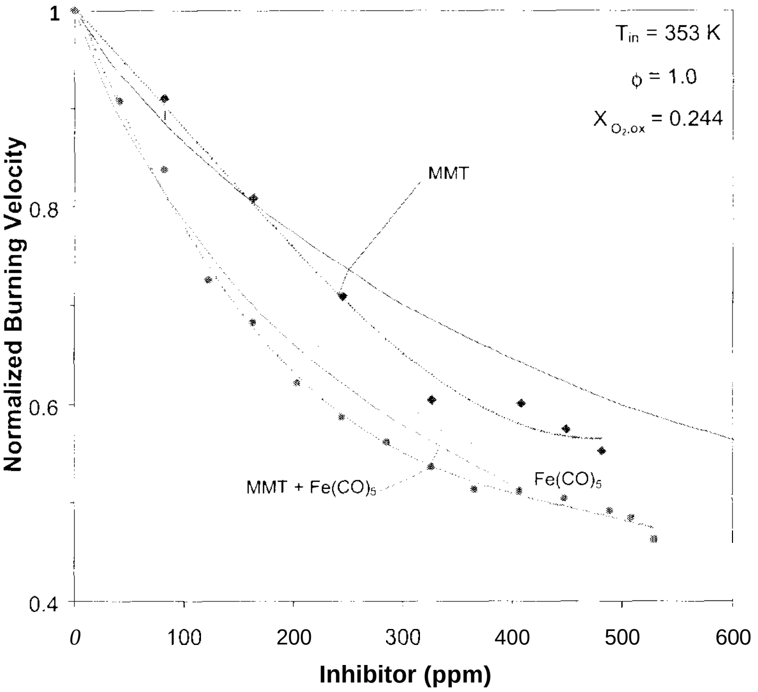

Figure 7 - Normalized burning velocity of premixed $CH_4/O_2/N_2$ flames inhibited by pure MMT and $Fe(CO)_5$, and by a blend of the two (dotted lines are curve fits to the data; solid lines are numerical model calculations).

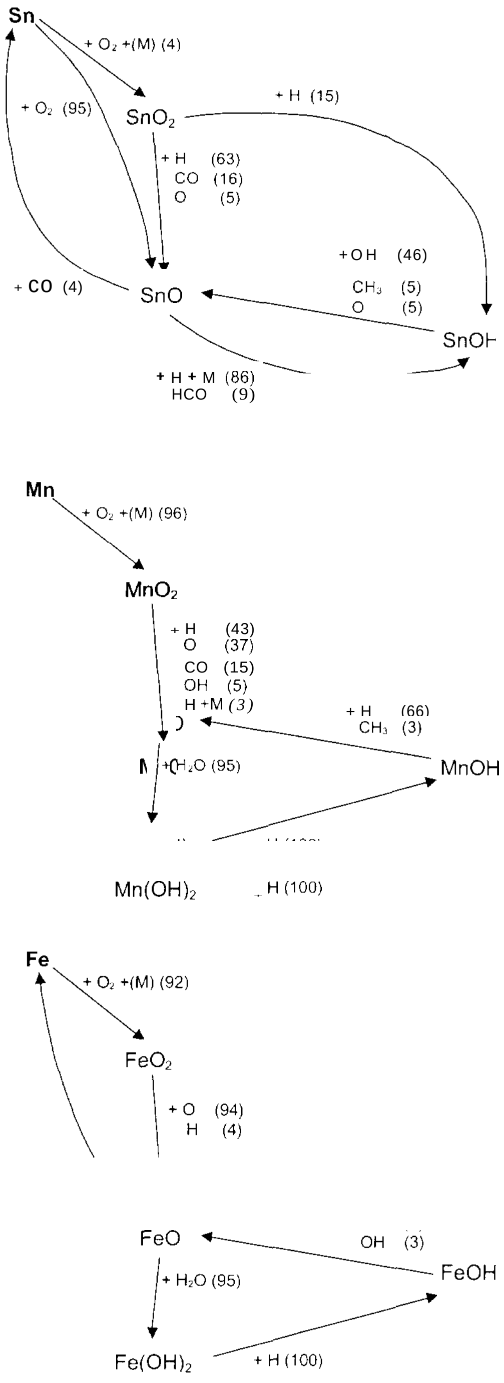

Figure 8 – Reaction pathway for Sn, Mn, and Fe in a premixed methane-air flame (ϕ=1.0, XO2,ox =0.21, Tin=353 K). TMT, MMT, and Fe(CO)5 present at (1963, 128, or 105) μL/L, respectively. The numbers in parentheses are the fractional consumption (percent) of the reactant molecule

3.2.5. Discussion

One of the benefits of numerical modeling of the flame structure of inhibited flames is that the results of the calculations provide detailed insight into the actual reasons for the strong inhibition. Further, the results for different inhibitors can be used to understand why they each demonstrate a different effectiveness. In the sections below, we discuss the inhibition mechanisms of tin and manganese, and compare them to that for iron. The difference in efficiency for these systems are shown to be related to the formation reaction and eauilibrium relationships for the intermediate metal di-hydroxide species Fe(OH)$_2$ and Mn(OH)$_2$.

3.2.5.1. Inhibition Mechanisms of Tin and Manganese

Examination of species profiles, reaction fluxes, and sensitivity coefficients from the numerically predicted flame structure allows investigation of the mechanisms of inhibition of these metallic compounds. The calculations show that TMT decomposes quickly in the flame, with 90 % consumption at 1000 K. **A** diagram showing the important reactions for tin inhibition is shown in Figure 8 (which also shows in parallel format the reaction paths for MMT, and Fe(CO)$_5$ inhibition). In the calculations used to prepare Figure 8, TMT, MMT, or Fe(CO)$_5$ were present at (1963, 128, or 105) μL/L, respectively, in the premixed methane-air flames (ϕ=1.0, T_{in}=353 K, and $X_{O_2,ox}$ =0.21); these volume fractions produced a 30 % reduction in flame speed.

The determination of the important reactions was based on consideration of both the reaction flux and sensitivities. The reaction flux represents the production or consumption of a species by chemical reaction. For a particular reaction, it is defined as the integral that reaction rate per unit volume over the entire flame domain. The total reaction flux for a species is defined as the sum of the reaction fluxes for the individual reactions which produce or consume it. In Figure 8, the pathway for consumption of each species is shown, with arrows connecting the relevant reactant and product species. The number next to each arrow represents the fraction of the total consumption flux for that species which proceeds through that particular reaction.

The tin atom formed as a result of TMT decomposition quickly reacts with O_2 through the reactions $Sn + O_2 (-M) \leftrightarrow SnO_2$, and $Sn + O_2 \leftrightarrow SnO + O$. The former reaction leads to SnO from the reaction of SnO_2 with CO, H, or other radicals. Conversely, the latter reaction forms SnO directly, and is fast at room temperature as compared to the analogous reaction of iron atom. Formation of SnO leads to the following reactions with H and HCO radicals:

$$SnO + H + M \leftrightarrow SNOH + M$$

$$SnO + HCO \leftrightarrow SnOH + CO$$

which, together with the radical scavenging reactions of SnOH, complete the catalytic radical recombination cycle of tin:

$$SnOH + H \leftrightarrow SnO + H_2$$

$$SnOH + OH \leftrightarrow SnO + H_2O$$

$$SnOH + CH_3 \leftrightarrow SnO + CH_4$$

$$SnOH + O \leftrightarrow SnO + OH$$

The net effect of the dominant inhibition reactions can be shown as:

$$SnO + H + M \leftrightarrow SnOH + M$$

$$SnOH + H \leftrightarrow SnO + H_2$$

$$\text{net: } H + H \leftrightarrow H_2$$

Equilibrium calculations show that SnO is the major tin species in the products of a stoichiometric methane–air flame with added TMT.

Figure 9 presents the sensitivity coefficients of the burning velocity to the rate constants (after adjustment) of tin-containing species for methane/air mixtures with equivalence ratios of 0.9, 1.0, and 1.1. In general, the burning velocity is sensitive to the rates of the catalytic cycle reactions with high fluxes: SnO reaction with H or HCO, and SnOH reaction with H, OH, CH_3, or O. The burning velocity is most sensitive to the rate of the reaction $SnO + H + M \leftrightarrow SnOH + M$. which has a sensitivity about four times less than the chain-branching reaction $H - O_2 \leftrightarrow OH + O$. As was found for DMMP and ferrocene additives [11,55], the burning velocity of flames inhibited by TMT is not particularly sensitive to the rate of the decomposition reaction. Numerical tests showed that changes in the overall activation energy of TMT decomposition in the range 170 kJ/mol to 335 kJ/mol have little effect on the burning velocity with up to 2000 μL/L of TMT. Hence, the inhibition effectiveness of tin compounds is likely to be independent on the parent molecule, as long as rapid decomposition occurs

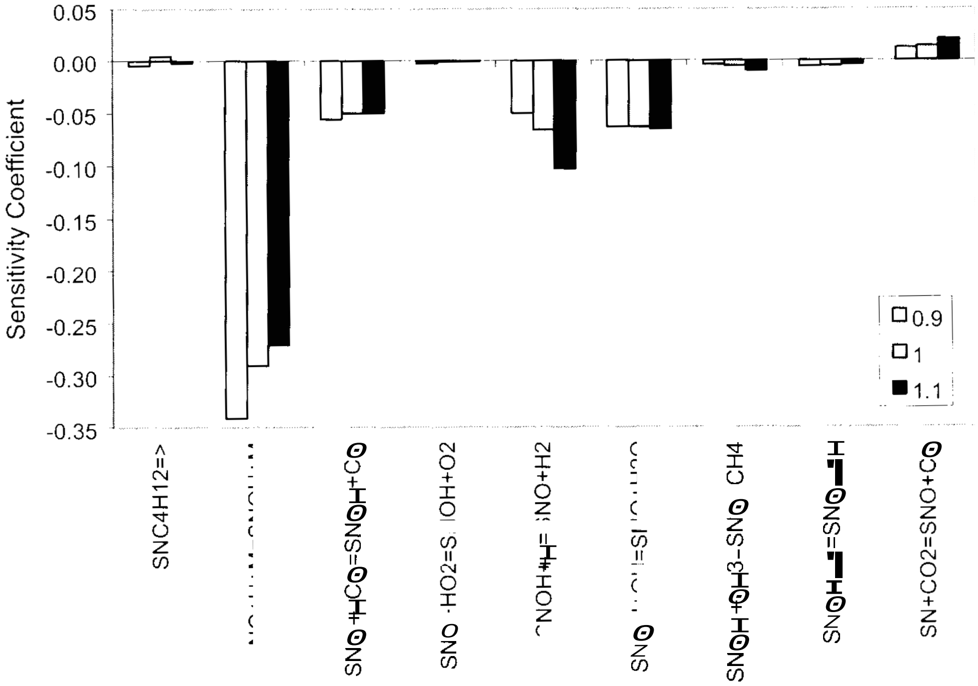

Figure 9 – First-order sensitivity coefficient of the burning velocity to the specific reaction rate constant for reactions with tin-containing species (1963 μL/L of TMT).

The reaction SnO + CO ↔ Sn + CO_2 (which is followed by $Sn+O_2=SnO+O$) is an additional route for CO consumption, and is chain-branching (net: $CO+O_2=CO_2+O$), which reduces the inhibiting effect of SnO in these flames. Similar behavior was found for CO – N_2O flames inhibited by $Fe(CO)_5$ [62]. Changes in these rates affect the calculated inhibition efficiency of TMT; nevertheless, the mechanism is dominated by the rate of reaction SnO + H + M ↔ SnOH + M.

Analysis of the numerical results for inhibition by MMT shows that the behavior of manganese in premixed methane-air flames is similar in many details to that of iron pentacarbonyl. The reaction pathway for manganese species is also shown in Figure 8, and the pathway for iron species from $Fe(CO)_5$ is shown for comparison. As with iron pentacarbonyl, Mn reacts with O_2 to form MnO_2 , which reacts primarily with radicals to form MnO. The catalytic radical recombination cycle consists of:

$$MnO + H_2O \leftrightarrow Mn(OH)_2$$

$$Mn(OH)_2 + H \leftrightarrow MnOH + H_2O$$

$$MnOH + H \text{ (or OH, O)} \leftrightarrow MnO + H_2 \text{ (or } H_2O\text{, OH)}$$

$$\overline{\text{net: } H + H \leftrightarrow H_2}$$

$$\text{(or: } H + OH \leftrightarrow H_2O,\ H + O \leftrightarrow OH\text{)}$$

Although flame equilibrium calculations show that the species MnH is present at relatively large concentrations, the contribution of reactions of this species to the inhibition effect is relatively small. Figure 10 shows the highest absolute values of the sensitivity coefficients of burning velocity to the rate constants (after adjustment) for reactions of manganese-containing species. The burning velocity is sensitive to the rates of the three reactions in the catalytic cycle above, with the rate of the reaction $Mn(OH)_2 + H \leftrightarrow MnOH + H_2O$ having the greatest absolute value. The burning velocity is also somewhat sensitive to the rates of the reactions forming MnO_2 and MnO. The reaction $MnO + H \leftrightarrow Mn + OH$ has a positive sensitivity; i.e. increasing its rate increases the burning velocity. This chain propagating reaction temporarily removes MnO from the catalytic cycle above, thus weakening the inhibition.

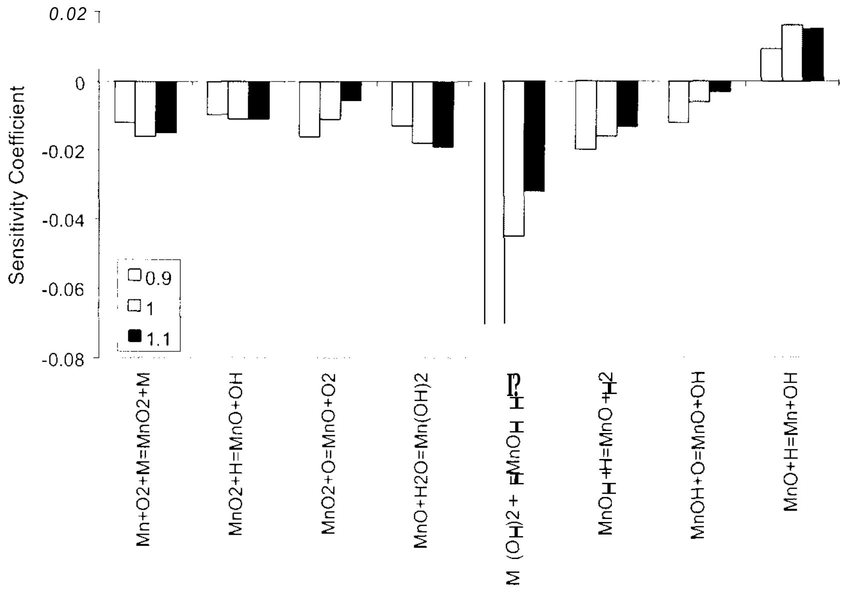

Figure 10 – First-order sensitivity coefficient of the burning velocity to the specific reaction rate constant for reactions with manganese-containing species (150 μL/L of MMT).

3.2.5.2. Comparison of inhibition by $Fe(CO)_5$, MMT, and TMT

In order to evaluate the inhibition mechanisms under comparable conditions, the numerical calculations (for $\phi=1.0$, $X_{O,ox}=0.21$, and $T_{in}=353$ K) were performed, as above, for initial values of TMT, MMT, and $Fe(CO)_5$ which provide an equivalent reduction (30 %) in the normalized burning velocity. These volume fractions were found to be 1963 µL/L, 128 µL/L, and 105 µL/L, respectively. While suppression of a fire would probably require higher agent concentration than that which provides a 30 % flame speed decrease, this degree of flame speed reduction was selected for two reasons. It provides a significant reduction in overall reaction rate (a factor of two), while keeping the agent concentration far enough above the values at which the model and experiments start to diverge (possibly due to condensation). For these flames, the structures are quite similar and the flame speed is the same (37.3 cm/s), allowing straightforward comparison of the inhibition mechanisms.

Based on the calculated results, TMT is required at a mole fraction which is about 17 times greater than iron or manganese compounds for a similar reduction in overall reaction rate. This occurs because the reactions to form SnOH from SnO are rate limiting and slow. Further, the reverse of the reaction $SnO + H + M \leftrightarrow SnOH + M$ is relatively fast at the location of peak catalytic cycle activity because SnO is a dominant equilibrium product in the high temperature region.

In order to further compare the performance of TMT, MMT, and $Fe(CO)_5$, it is useful to plot the relevant species mole fractions as a function of temperature through the flame. Figure 11 shows the mole fractions of the metal species in the inhibition cycles, and the radical species H, OH, and **O**. The vertical line shows the location of the maximum rate of the $H+O_2$ branching reaction. Note that the locations of the peak fluxes of the inhibition reactions (not shown) are very close to the peak flux of the $H+O_2$ reaction and to the maximum concentrations H, OH, and **O.** The bottom figure for TMT inhibition clearly shows the preponderance of SnO as the sink for tin atoms (note the rescaling) , hence requiring a large initial TMT mole fraction to achieve both fast reaction of SnO with H atom, and appreciable mole fraction of SnOH for radical scavenging. In Figure 11, consider the manganese containing species at the location of peak H-atom flux. MnO is present in higher mole fraction than FeO. This occurs from the significant backward reaction of $MnO + H_2O \leftrightarrow Mn(OH)_2$, which provides a lower $Mn(OH)_2$ concentration for the rate-limiting step $Mn(OH)_2 + H \leftrightarrow MnOH + H_2O$.

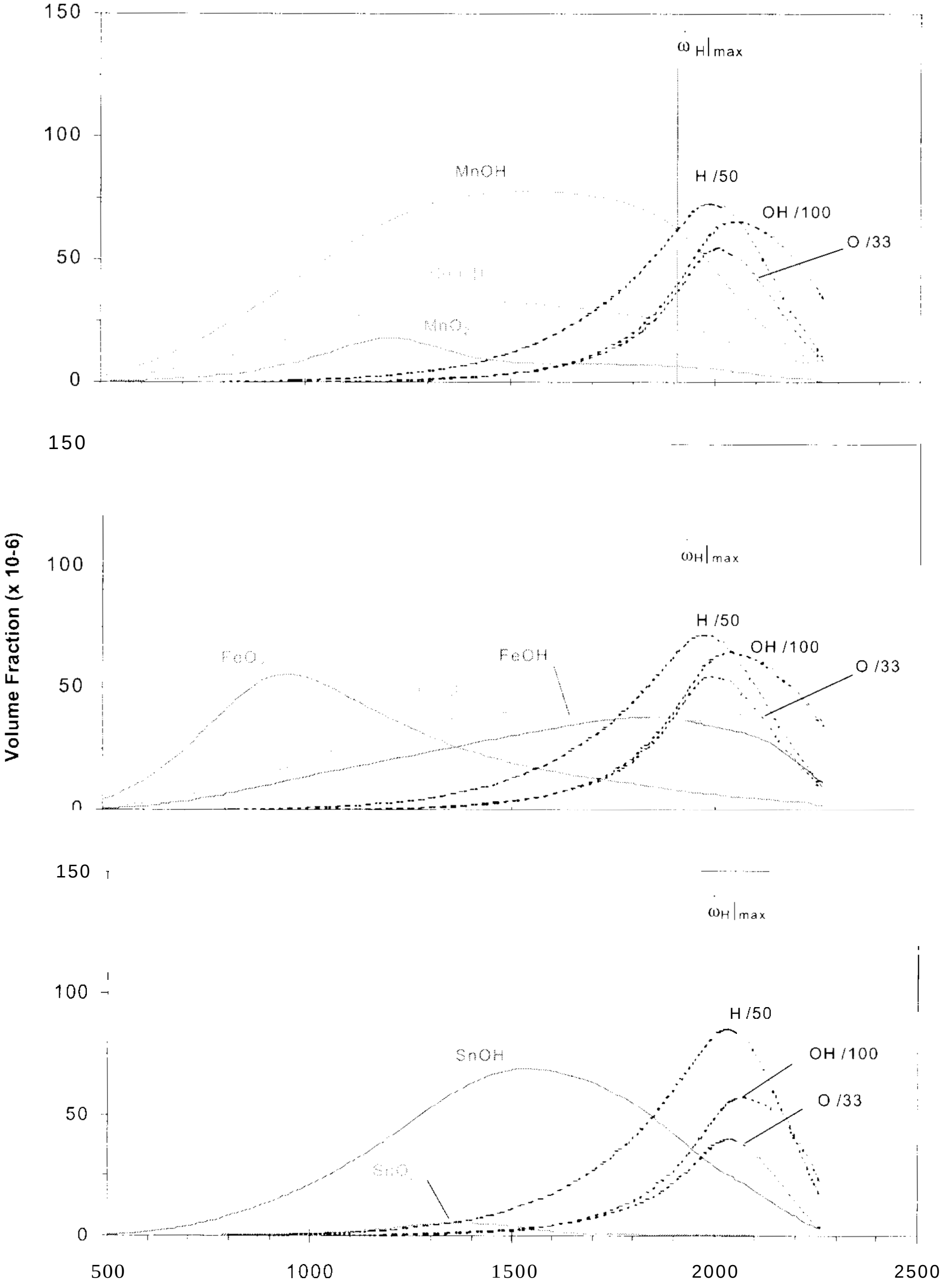

Figure 11 – **Volume fraction of metal species intermediates and H, O, and OH radicals, as a function of temperature in flame for** $Fe(CO)_5$, **MMT, and TMT added at 106 μL/L, 128 μL/L, and 1963 μL/L (corresponding to a 30 % reduction in flame speed).** T_{in}**=353 K,** ϕ**=1.0,** $X_{O_2,ox}$ **=0.21.**

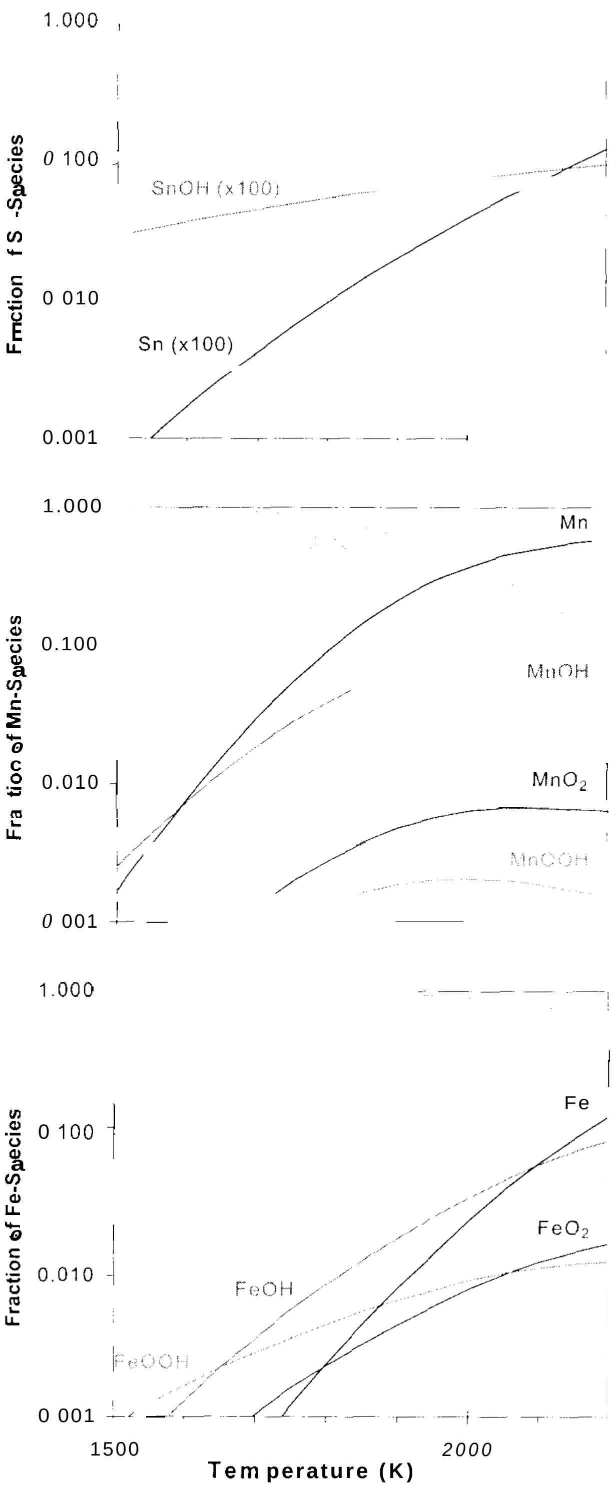

Figure 12 – Fraction of Sn-, Mn-, and Fe-species at equilibrium in methane-air flames as a function of temperature.

The importance of constraints on equilibrium concentrations as they relate to inhibitor efficiency is illustrated in Figure 12 which shows the fraction of all metal species in the flame. For these equilibrium calculations, the metallic element (Sn, Mn, or Fe) is present at a mole fraction or 1.0×10^{-4}, and methane and air are present at stoichiometric proportions. For TMT inhibition, the Sn appears overwhelmingly as SnO (note the scale change on Sn and SnOH), thus higher levels of TMT are required to yield the required levels of SnOH reaction with H atom, and for the required rates of the slow reaction SnO + H + M $\leftrightarrow$ SnOH + M. Note that since the flames of Figure 11 all have equivalent levels of inhibition, the flux of each radical recombining catalytic cycle is about the same; e.g., SnOH, MnOH, and FeOH must be present at about the same mole fraction since their rates of reaction with H-atom are close, and the rates of reactions forming the hydroxide are approximately the same. Comparing $Mn(OH)_2$ and $Fe(OH)_2$ in Figure 12, we see that in the MMT-inhibited flames, the concentration of $Mn(OH)_2$ for temperatures above 1800 K drops off rapidly, whereas in the $Fe(CO)_5$-inhibited flames, $Fe(OH)_2$ does not. Since the reaction of $Mn(OH)_2$ with H atom is rate-limiting (Figure 10), decreases in the $Mn(OH)_2$ mole fraction make MMT less effective as an inhibitor than $Fe(CO)_5$.

3.2.6. Conclusions

In this section we presented the first experimental measurements of the influence of manganese- and tin-containing compounds (MMT, TMT) on the burning velocity of methane/air flames. Comparisons with the agents $Fe(CO)_5$ and CF_3Br demonstrate that manganese and tin-containing compounds are effective inhibitors. The inhibition efficiency of MMT is about a factor of two less than that of iron pentacarbonyl, and that of TMT is about twenty-six times less effective, although TMT is about twice as effective as CF_3Br. There exist conditions for which both MMT and TMT show a loss of effectiveness beyond that expected due to radical depletion, and the cause is believed to be particle formation. Kinetic models describing the inhibition mechanisms of MMT and TMT additives were suggested. Simulations of MMT- and TMT-inhibited flames show reasonable agreement with experimental burning velocity data. The decomposition of the parent molecule for the tin and manganese species is found to have a small effect on the inhibition properties for the range of concentrations used in this work. Calculations confirmed that the main tin-containing species in the flame zone is SnO, while the concentrations of SnO_2, SnOH and Sn are relatively small. The inhibition effect of TMT is determined mostly by the rate of the association reaction $H+SnO + M \leftrightarrow SnOH + M$, and the catalytic recombination cycle is completed by the reactions $SnOH + H \leftrightarrow SnO + H_2$ and $SnOH + OH \leftrightarrow SnO + H_2O$. The inhibition mechanism of manganese-containing compounds is similar, in many details, to the inhibition mechanism for iron pentacarbonyl: $MnO + H_2O \leftrightarrow Mn(OH)_2$; $Mn(OH)_2 + H \leftrightarrow MnOH + H_2O$, and $MnOH + OH$ (or H) $\leftrightarrow MnO + H_2O$ (or H_2). The burning velocity is most sensitive to the rate of $Mn(OH)_2 + H \leftrightarrow MnOH + H_2O$ reaction. Comparison of the mechanisms of inhibition of TMT and MMT to $Fe(CO)_5$ shows that the manganese is not as efficient an inhibitor as iron: due to equilibrium constraints, the mole fraction of the intermediate species $Mn(OH)_2$ drops off at higher temperature (in comparison to $Fe(OH)_2$), slowing its rate-limiting reaction with H atom in the catalytic cycle. This result illuminates the role of equilibrium constraints on species concentrations in the efficiency of catalytic cycles.

3.3 Water with Metal Additives

Water droplets with metal additives are both a useful way to test non-toxic forms of metals, and also one possible way in which they might be used in some applications. This section of the report describes development of an experimental and analytical approach for understanding the benefit of metallic additives to water droplets. It also provides experimental results for solutions of water with NaOH, KOH, NaCl, and $FeCl_2$. The results delineate the parameters important for the efficient use of additives to water, and describe how the characteristics of the flame system itself influences the conclusions about the effectiveness of a particular agent.

3.3.1 Introduction

Since the international ban on production of halon 1301 (because of its adverse effect on stratospheric ozone), application of fine-water droplets as an effective fire suppressant has received considerable attention. Fire suppression by fine-water droplets is attributed to its thermal effects associated with latent heat of vaporization [63], and recent laboratory studies [64] and parallel modeling efforts have established quantitative estimates of these thermal contributions [65,66]. Further enhancement of the fire suppression ability of fine-water droplets through the use of chemical agents has recently received considerable attention [67] and is the main focus of the present investigation. Alkali metals (for brevity Am) have a strong chemical effect in flames, about an order of magnitude more than CF_3Br, and consequently, are good candidates for addition to water sprays. Due to the low vapor pressure of these metals, for example partial pressure $\sim 10^{-32}$ of NaOH at 298 K, they require application as a condensed phase, either as a fine-powder or as a solution in fine water spray to obtain any significant flame suppression.

In order to understand the suppression mechanisms and optimize the performance of chemical agents added to water droplets, it is desired to conduct experiments which can be used as a database for detailed numerical modeling. Extensive tests of metal salts added to a hybrid diffiision-premixed flame were conducted by Vanpee and Shirodkar [29], providing unprecedented data on the effectiveness of metals as flame inhibitors. It is somewhat difficult to model those experiments or interpret the results in detail, however, since some important experimental parameters were not provided (such as the equivalence ratio of these partially premixed flames, and the droplet sizes). Further, their experiments were not conducted over a range of additive mole fractions, which, as described in this paper, is an important parameter. Experiments by Mitani and Niioka [68] considered inhibition of premixed flames with ultra-fine water droplets (less than 2.4 um mean diameter) containing NaOH and $NaHCO_3$, indicating a flame inhibition/extinction with addition of chemical agents. In particular, their slower $C_2H_4/O_2/N_2$ premixed flame experiments (as opposed *to* faster $H_2/O_2/N_2$ flames) showed distinct chemical inhibition effects, but the saturation effects due to condensation of metal vapors were not explored. Recent work by Zheng et al. [67] on counterflow premixed flames inhibited with water/NaCl fine-droplets in fact show signs of saturation with increasing NaCl mass fraction in water. But the reported data on equivalence ratio vs. flame extinction strain rate, at constant water mass addition, is the clearest approach for demonstrating that effect.

Motivated by the need to gain detailed understanding of the parameters important for water additives to be effective inhibitors in flames, and to provide a database suitable for numerical modeling in codes currently being developed, we conduct the experiments described below. Ultimately, the goal is to use droplets with additives for testing the effect of non-toxic forms of metals . Some preliminary data is presented below for $FeCl_2$ in water droplets, but first, we develop the experimental technique. **As** will be demonstrated, droplet size, droplet residence time in the flame, and the saturation of active species produced by the chemical additive are key features which must be controlled to obtain peak performance for the given time-temperature characteristics of an actual fire.

3.3.2. Experiment

Two laboratory flame configurations were used, producing non-premixed and premixed methane-air flames. The burners were designed to be modular, so that the same water generation and gas supply systems could be used with either. The air was supplied by an oil-free shop compressor followed by a series of desiccant beds, and the fuel gas was methane (BOC grade 4.0, 99.99% purity). For the non-premixed flames, gas flows were measured by Teledyne Hastings-Raydist flow meters (factory calibrated with a reported accuracy of +/-1% of full scale reading), and for the premixed flames, by Sierra model 860 mass flow controllers (calibrated with a Bios model 20K piston flow meter so that their expanded relative uncertainty is 2%). For experiments involving water droplets, the metered dry air was saturated with water vapor before feeding to the burner [69]. The relative humidity was verified with a hygrometer (Testo 605-H1).

The droplet generation system used (Sono-Tek Model 8700-120) consisted of the ultra-sonic nozzle and a broadband ultrasonic frequency generator. **A** syringe pump (Instech Model 2000) with a plastic 10 cm^3 syringe fed water to the atomizer. The water mass flow rate at the nozzle exit was measured gravimetrically. by carefully collecting the droplets on a collection surface. While the fraction of water fed to the atomizer which actually reached the nozzle exit was only about 70%, the operation of the droplet injection system was very repeatable over the entire range of water and air flows of the tests. Near the atomizer tip, the droplet size distribution has been characterized by the manufacturer as a log-normal

3.3.2.1. Counterflow Burner

In the counterflow burner, a steady, planar, non-premixed flame was established in the mixing layer of the opposed methane and air streams. The fine-water droplets were introduced with the air stream, which was first saturated with water vapor to eliminate evaporation of the droplets prior to their reaching the hot thermal mixing layer. The fuel and air nozzles (Pyrex glass) each have an area contraction ratio of 6.5 and an exit diameter of 1.5 cm, and at their exits, have nearly plug flow velocity profiles (verified previously through laser-Doppler velocimetry measurements [70]). Co-flowing nitrogen streams on both the fuel and air sides helped to maintain a very stable planar flame disk. The nozzles were enclosed in a cylindrical burner chamber, in which water cooling coils and air dilution of the post-combustion gases eliminate secondary flames. The nozzle tubes enter the chamber through vacuum fittings which permit easy adjustment of the nozzle separation distance (L), which is typically set to 12 mm. **A** schematic and a detailed description of this burner can be found in Ref. [69].

In the non-premixed flame experiments, the water mass flow rate was fixed, and the air and methane flows were increased together until the flame was extinguished. The fuel and air flows were adjusted so as to balance their momentum; i.e., $(\frac{1}{2}\rho v^2)_{air} = (\frac{1}{2}\rho v^2)_{CH_4}$, where p is the density and v is the axial velocity. Knowing the nozzle separation distance, the global flow strain rate at extinction is defined by $a_{ext} = 4|v_{air}|/L$, providing a suitable parameter that describes the non-premixed flame extinction condition [71]. The total water (or solution) droplet mass fraction in the air+saturated water vapor stream is defined here as Y_0, while the mass fraction of the additive (i.e., NaOH, KOH, NaCl or $FeCl_2$), is defined as y_{add}. In experiments, variation of a_{ext} with Y_0 as well as y_{add} were measured.

3.3.2.2. Premixed Burner

The premixed burner used for the present two-phase investigations consisted of a straight sided conical flame established at the exit of a Mache-Hebra type nozzle [70]. **A** schlieren imaging system provided the flame cone angle, which was used to determine the burning velocity [34]. The nozzle exit flow profile was characterized by laser Doppler velocimeter measurements described previously [34]. The typical half-cone angle of the flame was about 20" . With addition of the solution droplets, the flame height was maintained constant at about 2 cm by adjusting the total flow rate of reactants, while maintaining the equivalence ratio at the desired value. For the present data, the uncertainty (expanded uncertainties with a coverage factor of 2) in the burning velocity is ± 6 %.

The inhibition of a laminar premixed flame can be characterized by the relative decrease in the burning velocity (denoted here by S_L) with respect to that of an uninhibited flame (S_L^0). The simple conical premixed flame stabilized above the Mache-Hebra nozzle, and the associated flame cone angle measurement technique adopted here is one of many traditional methods of obtaining the laminar flame speed [34]. While curvature and stretch effects do exist in the flame, they are considered minor, particularly since all results in the present section are reported as normalized flame speed, S_L/S_L^0 . The uninhibited methane and air flame speed obtained from the present burner is (35 ± 1.2) cm/s. Because the ultrasonic atomizer and the length of the Pyrex tube delivering the reactant gas-mixture are the same as in counterflow burner, the median droplet diameter is not expected to be different from that of counterflow flames reported above.

3.3.3. *Results*

3.3.3.1. Extinction of Non-premixed Flames with Water/Solutions

Water-NaOH Fine-Droplets:

Figure 13 shows a comparison of droplet mass fraction in air (Y_0) as a function of the global extinction strain rate *(a,,.,)* with varying NaOH mass fraction in water (y_{NaOH}). Similar results were reported earlier for NaOH mass fractions in water of $y_{NaOH} = 0.055$, 0.112 and 0.175 [69]. In the earlier data, at the lowest flow strain rate of 125 s^{-1}, the case of 0.175 NaOH in water showed a significantly higher effectiveness over 0.055 and 0.112 NaOH cases (i.e., Y_0=0.005 for y_{NaOH}=0.175 vs. Y_0=0.010 for y_{NaOH}=0.055 and 0.112). However, for higher extinction strain rates (> 125 s^{-1}), the previous experimental data indicated negligible differences in extinction condition with varying NaOH mass fraction. These somewhat inconsistent results with varying NaOH mass fractions clearly required further investigation, including investigation about the effectiveness of NaOH at lower mass fractions (i.e., $y_{NaOH}< 0.055$). The new data reported here indicate that the differences in Y_0 for y_{NaOH} of 0.055, 0.112 and 0.175 are within experimental uncertainty. Distinct effects of NaOH mass fraction are obtained only for $y_{NaOH} <0.055$.

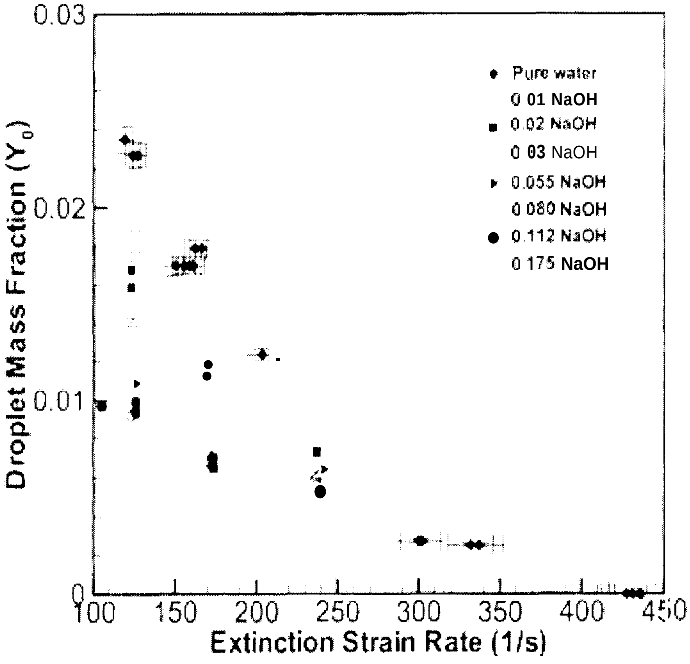

Figure 13 – Droplet mass fraction (Y_0) as a function of extinction strain rate of a methane-air non-premixed flame, for several NaOH mass fractions in water (y_{NaOH}).

The difference between the new y_{NaOH}=0.175 data and previous results was found to be caused by a temperature dependence of the ultrasonic nozzle performance. When the nozzle tip was allowed to reach a steady operating temperature, typically about 40 °C after about 15 min of continuous operation, the resulting flame extinction data were consistent and reproducible. While the revision of y_{NaOH}=0.175 data can be attributed to ultrasonic atomizer nozzle performance, the observation that the mass fraction of NaOH above 0.055 yields no apparent increase in flame suppression is rather interesting and requires further analysis.

The flame extinction results shown in Figure 13 at the strain rate of 125 s^{-1} are re-plotted in, Figure 14 according to the variation of droplet mass fraction (Y_0) vs. NaOH mass fraction in water (y_{NaOH}). As y_{NaOH} is increased above 0.08, the total droplet mass fraction (Y_0) needed for flame extinguishment is seen to become invariant with the NaOH mass fraction in the droplet. Similar saturation behavior has been reported in premixed flames with iron, manganese, and tin organometallic compounds [10,12], and metal salts added as particles [72]. Also shown in Figure 14 is the mole fraction of NaOH in air (X_{NaOH}) assuming that NaOH in droplets is completely released to the gas-phase. Under such an assumption (reasonable if the droplets are completely vaporized at or before the flame). it is not surprising that X_{NaOH} increases almost linearly with increasing NaOH mass fraction in water-NaOH solution. In reality, however, the maximum X_{NaOH} (in equilibrium) is directly related to the partial pressure of NaOH (or any other low vapor pressure sodium compound), and is a function of temperature only. Figure 14 indicates that this limiting value of X_{NaOH} is about 0.0006 (or 600 μL/L of NaOH in air). Therefore, as seen in Figure 14, any increase in NaOH vapor above this partial pressure, for example $y_{NaOH}>0.08$, may not yield any improvement in the fire suppression ability of water-NaOH solution.

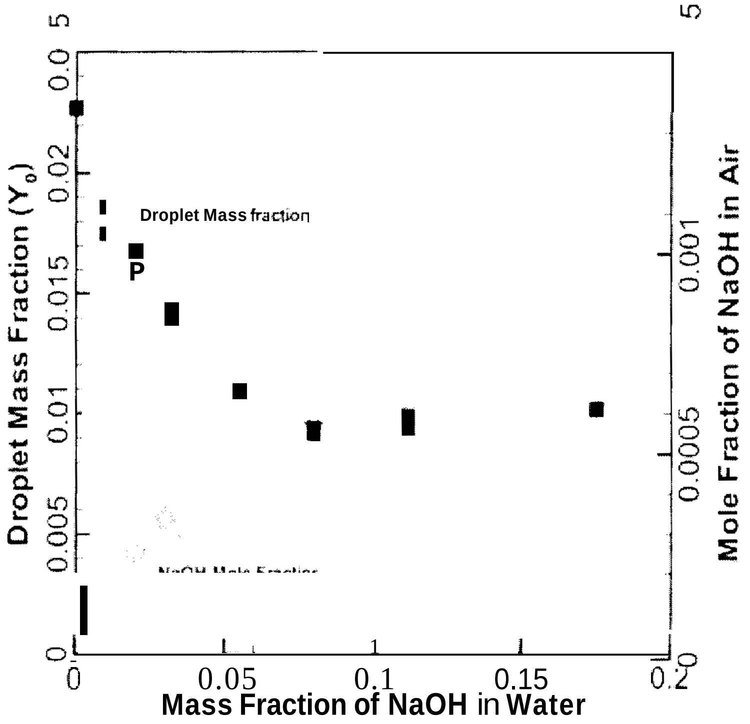

Figure 14 – Y_0 and mole fraction of NaOH in air as a function of y_{NaOH} , for the extinction strain of 125 s^{-1} in Figure 13.

The thermochemical data of NaOH can be used to estimate the gas-phase conditions that yield the limiting value of $X_{NaOH}=0.0006$. Assuming that NaOH exists as a monomer in the gas-phase, an equilibrium liquid-vapor calculation based on the Clausius-Clapeyron equation yields an NaOH saturation temperature of 1125 K. This vapor-liquid equilibrium temperature is about 400-500 K below the characteristic temperature within the rate-limiting oxygen-consumption, radical-production region of the flame [73]. Because of the thermal boundary layer surrounding each evaporating droplet, it is conceivable that an effective temperature below the flame temperature may control the saturation of excess NaOH vapor. Alternatively, loss of active inhibiting species to condensation may be controlled by a compound with a lower vapor pressure than NaOH. In experiments, resolving the appropriate effective temperature that controls saturation of condensation of the relevant species is perhaps impossible, and therefore, only detailed numerical simulations can provide better understanding of the saturation phenomenon occurring. Although numerical simulations that include detailed interactions between the condensed-phase and the gas-phase have recently been developed to describe water-droplet interactions [74], analytical models for droplet evaporation of binary mixtures in flames have not. In this case, modeling of the evaporation of binary liquid droplets with highly disparate boiling temperatures (373 K for water vs. 1663 K for NaOH) may require further simplifications. Hence, in this paper, only experimental results are presented with binary evaporating droplets.

Water-KOH Fine-Droplets:

Besides NaOH, other alkali metal compounds are known to be chemically effective fire suppressants. In particular, potassium containing compounds are believed to be more effective than sodium [72,75]. Figure 15 shows experimentally obtained extinction strain rates of a methane-air non-premixed flame, with similar sized water-KOH droplets, containing varying mass fractions of KOH. For the lowest extinction strain rate considered (i.e., 125 s^{-1}), the data show increasing flame suppression up to about y_{KOH}=0.112. Further increase in KOH mass fraction in water up to 0.175, however, yields no further increase in the flame suppression ability of the water-KOH solution. Following the analysis of water-NaOH saturation vapor conditions, current water-KOH results indicate that the KOH saturates at a gas-phase mole fraction of about X_{KOH}=0.0003, for y_{KOH}=0.112. Liquid-vapor equilibrium data for KOH indicate that this mole fraction corresponds to a gas temperature of about 1025 K, which is about 100 K lower than that obtained for the NaOH case. This lower effective saturation temperature for KOH is consistent with the lower boiling temperature of KOH (1597 K) compared to that of NaOH (1663 K).

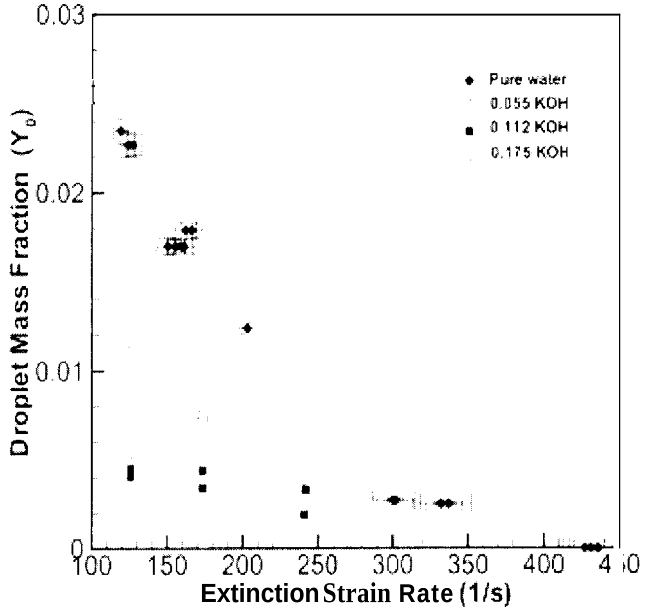

Figure 15 – Droplet mass fraction (Y_0) as a function of extinction strain rate of a methane-air non-premixed flame, for several KOH mass fractions in water (y_{KOH}).

Water-NaCl and Water-$FeCl_2$ Fine-Droplets:

Non-premixed methane-air flame extinction experiments were also conducted with NaCl. Water-NaCl droplets have been considered previously by Zheng et al. [67], but only in the context of extinction of counterflow premixed flames as a function of fuel-air equivalence ratio. The flame suppression trends shown in Figure 16, with increasing NaCl mass fraction in water are consistent with previous data with NaOH and KOH. The metal Fe (in Fe^{+} or Fe^{2+} form) has previously been shown to be very effective [29]. Here, exploratory experiments were conducted to test the efficacy of an Fe^{2+} compound, such as $FeCl_2$ dissolved in water. **A** mass fraction of $FeCl_2$ in water (y_{FeCl_2} = 0:15) was tested and this water-$FeCl_2$ solutions clearly showed chemical inhibition effects. Nonetheless, experiments with lower mass fractions of $FeCl_2$ must be performed to evaluate the occurrence of saturation phenomenon, as observed in water-NaOH solutions.

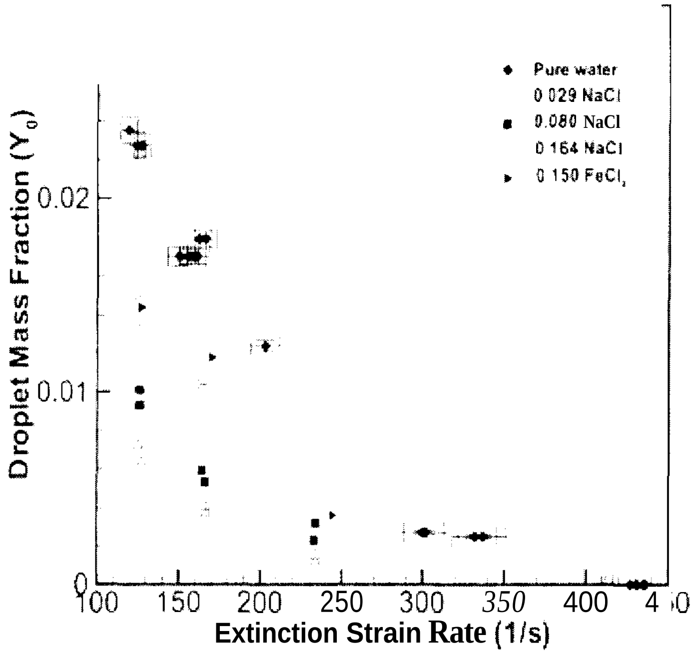

Figure 16 – Droplet mass fraction (Y_0) as a function of extinction strain rate of a methane-air non-premised tlame. for several NaCl and $FeCl_2$ mass fractions in water (y_{add}).

Molar Comparisons of NaOH, KOH, and NaCl

In order to relate the chemical inhibition of the agents considered here to previous studies, the non-premixed flame extinction results are analyzed here on a molar basis for the additive. To avoid uncertainties related to saturation effects, only additive mass fractions below the saturation condition are considered here. Since water-NaOH extinction results show that saturation of NaOH vapor is approached for additive mass fractions above 0.055, the molar comparisons between NaOH and KOH are performed at y_{add}=0.055. For the extinction data points considered, the mole fraction of alkali metal hydroxide (AmOH) was evaluated and is plotted as a function of flame extinction strain rate, as shown in Figure 17a. These molar comparisons clearly indicate roughly two times performance benefit of KOH over NaOH as an additive to water droplets, similar to what has been reported based on flames inhibited with particulates [72,75]. More recent kinetic studies have indicated that recombination of K with OH is about 30 % faster than Na with OH and that recombination of K with O_2 is in fact two to three times faster than Na than with O_2 [76] and this perhaps is the primary reason for the effective flame suppression by KOH. Comparison of molar plots of NaCl vs. NaOH, shown in Figure 17b, indicates surprisingly superior flame suppression ability of NaCl. This is, however, consistent with the saturation of NaCl or NaOH since the vapor pressure of NaCl at 1125 K is 1.8 times that of NaOH. For a droplet mass loading of $Y_0=0.014$ and an extinction strain rate of 125 s^{-1}, a comparison of the mole fraction of chemical agent needed in air (X_i) yields the following order: $X_{KOH} = 0.00021 < X_{NaCl} = 0.00023 < X_{NaOH} = 0.00034 < X_{FeCl_2} = 0.00056$ (assuming linear interpolation between available data). These values indicate that on a molar basis KOH is the most effective chemical agent, followed by NaCl and NaOH. For water-$FeCl_2$, the interpolation was performed assuming that $y_{FeCl_2}=0.15$ is unsaturated at this rather high molar loading, which is certainly questionable. If $FeCl_2$ is found to condense at a lower additive mass fraction (eg. $y_{FeCl_2} < 0.05$), then on a molar basis water-$FeCl_2$ could become the most effective solution as X_{FeCl_2} will approach 0.00018 (instead of 0.00056 above).

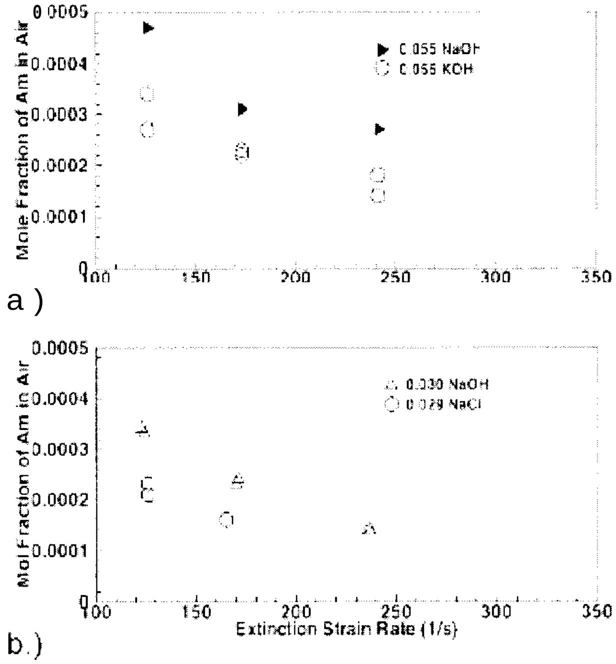

Figure 17 – a.) Mole fraction of alkali metal (Am) in air as a function of non-premixed methane-air flame extinction strain rate, for NaOH and KOH mass fractions of 0.055 from data of Figure 13 and Figure 15; b.) Mole fraction of alkali metal (Am) in air as a function of non-premixed methane-air flame extinction strain rate, for NaOH and NaCl mass fractions of 0.03from data of Figure 13 and Figure 16.

3.3.3.2. Inhibition of Premixed Flames with Water-NaOH Droplets

The inhibition of premixed flame propagation with various chemical fire suppressing agents is well documented [10,24,77]. Here, we consider the inhibition of a conical premixed flame with fine water-NaOH droplets. Based on phenomenological reasoning [78], it is well known that the burning velocity is proportional to the square-root of the chemical reaction rate. Consequently, we plot in Figure 18 the square of normalized burning velocity [$S=(S_L/S^0_L)^{1/2}$] vs. droplet mass fraction (Y_0), for varying NaOH mass fraction in water (y_{NaOH}). With increasing y_{NaOH}, these results do not show any significant increase in flame inhibition compared to the inhibition with pure water droplets. This is a rather unexpected finding because of the close similarities (described below) between the two laboratory flames considered. This insensitivity of y_{NaOH} in water droplets, for the premixed flame configuration, can be explained by considering the droplet residence times in the flame. Because of the vast difference in the boiling temperature between water and NaOH (373 K vs. 1663 K), water is expected to evaporate first. If the flow residence time of droplets through the premixed flame is less than that through counterflow flames, a partially vaporized droplet (smaller than the initial 13 μm at the inflow boundary) with much higher concentration of NaOH will emerge. Therefore, the lack of chemical inhibition observed in the premixed experiments with water/NaOH solutions may be caused by partially vaporized droplets. To test this hypothesis, the flow residence times of droplets through premixed and non-premixed flames, inhibited with pure-water droplets, are investigated below.

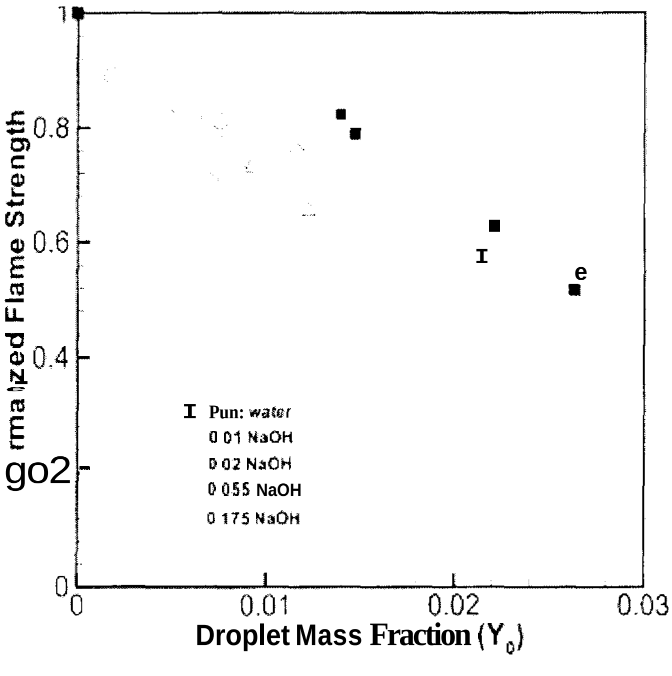

Figure 18 – Square of the normalized burning velocity of a premixed flame inhibited with fine-droplets of water/solution, for several NaOH mass fractions in water.

3.3.3.3. Comparison of Non-premixed and Premixed Flames with Pure-Water Droplets

As described above, the premixed flame burning velocity is proportional to the square-root of the overall chemical reaction rate. The non-premixed flame extinction strain rate, however. is directly proportional to the chemical reaction rate. A formal asymptotic analysis [79], assuming that the overall reaction of the form Fuel + Oxidizer → Products is applicable to both premixed and non-premixed flames, yields the following relationship between the burning velocity and extinction strain rate,

$$(\rho_0 S_L^0)^2 \propto (\rho\lambda/c_p Z_{st}^2)\, a_{ext}$$

where Z,, is the stoichiometric mixture fraction (assumed to be a small parameter), λ the thermal conductivity, and c_p the specific heat. Based on this relationship and assuming that the mixture fraction, transport and thermodynamic properties are not affected by the small fraction of condensed-phase agent added [80], a direct comparison of the extinction/inhibition of non-premixed and premixed flames can be accomplished by defining normalized flame strength as

$$S = (S_L / S_L^0)^2 = (a_{ext,\, inhib} / a_{ext,\, uninhib})$$

Its applicability for droplets of pure water is examined in Figure 19, which shows the normalized flame strength for the premixed and non-premixed flames as a function of the mass fraction of water. The comparison clearly shows that the 13 μm median diameter droplets are not equally effective in inhibiting the premixed flame. (Note that for proper normalizations, S_L^0 corresponds to a case where the premixed methane-air stream is saturated with water vapor, and $a_{ext,uninhib}$ to a case where the non-premixed air stream is saturated with water vapor.)

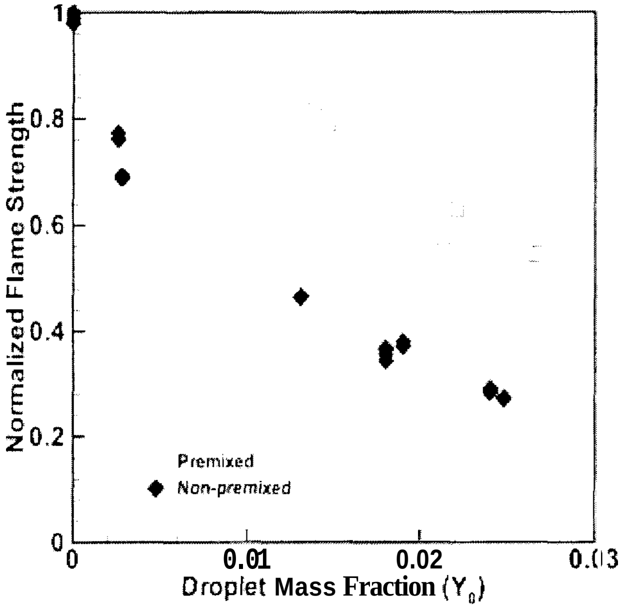

Figure 19 – Normalized flame strength of non-premised and premised methane-air tlames, inhibited with fine-droplets of water with a median diameter of 20 μm.

Effect of Flow Residence Time:

The above mentioned differences between the inhibition of non-premixed and premixed flames by pure water droplets, as well as the disparate results for droplets of water/NaOH in premixed flames, can be explained based on the flow residence time associated with each flame structure and its effect on the evaporation of fine-water droplets. Figure 20 shows the numerically obtained flame structure of a premixed and a non-premixed flame, corresponding to conditions where the flame is inhibited by 13 μm droplets with droplet mass fraction of Y_o–0.01. The estimated flow residence time of these droplets through the thermal layer, from the cold boundary up to the peak flame temperature differs substantially, 4 ms for the premixed vs. 14 ms for the non-premixed. This implies that the time available for the droplets to vaporize in premixed flames is considerably less than in the non-premixed flames, and that the 13 μm droplets are not necessarily the ideal size for inhibiting the premixed flame considered. Consequently, the maximum thermal cooling is not achieved compared to the counterflow flame, resulting in the lower flame inhibition observed in Figure 19 for premixed flames.

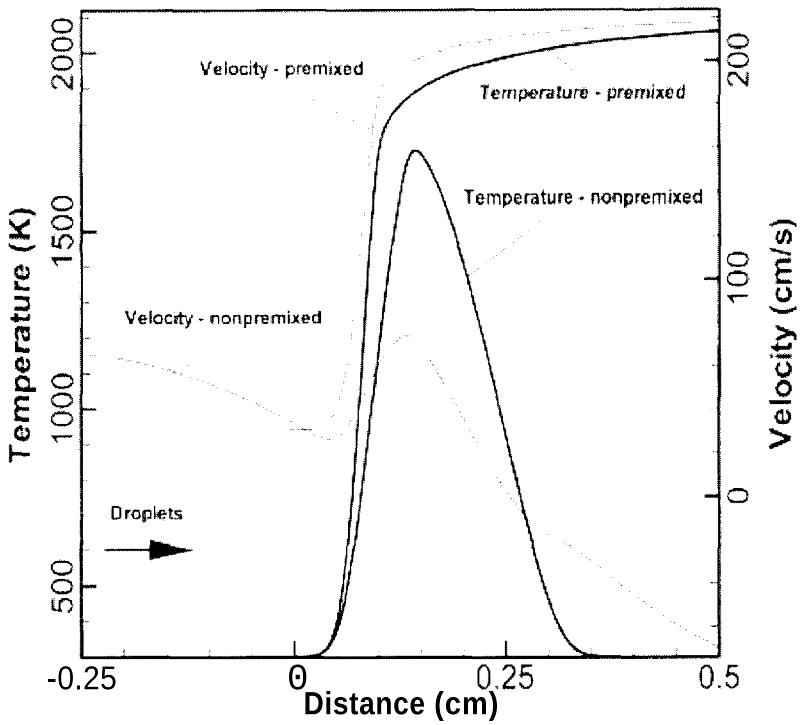

Figure 20 – Non-premixed and a premised flame structure, corresponding to inhibited conditions of water droplet mass fraction of Y_0=0.01.

Interestingly, this finding also explains the much poorer relative effectiveness of either NaOH or KOH at a=240 s^{-1} vs. a=125 s^{-1} , as shown in Figure 13 and Figure 15. The higher strain flames have lower residence time, possibly preventing the release of the additive to the gas phase.

3.3.4. Conclusions

The low vapor pressure of alkali metals at normal room temperature requires delivery of alkali metals as a powder or as a fine-droplet spray for their efficient delivery to a flame. However, efforts to combine the thermal fire suppression ability of fine-water droplets with the chemical inhibition of alkali metals have indicated the existence of an upper agent limit because of the associated limiting vapor pressure of the additive. When the mass fraction of alkali hydroxide in water is below this condensation limit, comparison of the chemical effectiveness clearly indicates that KOH is about two times more effective than NaOH on a molar basis, for a wide range of flow strain rates. Comparison of the effectiveness of water-NaOH with water-NaCl on a molar basis indicates a superior effectiveness of NaCl over NaOH, which can be explained based on their vapor pressures.

The relationship between droplet size and flow residence time is found to be important both for comparing the behavior of condensed phase agents between flame types, as well as for evaluating the efficacy of chemically active additives. Comparison of the effects of water-NaOH droplets on the extinction of non-premixed and inhibition of premixed flames implies that if the droplets are not *completely* evaporated before the chemical reaction layer because of non-optimal droplet size or too short droplet residence time, then the full chemical effectiveness of the agent is not realized. Similarly, when equally sized fine-water droplets are introduced to non-premixed and premixed flames, with no velocity lag between the droplets and the gas-phase (at the inlet), the characteristic flame extinction/inhibition conditions of the two flames differ. Flame structure analysis has revealed that the distinct flow residence time of droplets (with a median diameter of 13 μm) through each flame structure, i.e., 14 ms for the non-premixed flame vs. 4 ms for the premixed flame, is the cause for the observed differences. These results illustrate the importance of understanding the particular reacting flow field and temperature conditions in order to assess the intricate coupling between droplet size and its residence time through the flame structure. These effect must be considered in designing optimal fire suppression systems based on fine-droplets of water/solutions.

3.4. Cup Burner Flame Extinction Tests with Metal Compounds

3.4.1. Introduction

Early in this project it was discovered that $Fe(CO)_5$ did not work well in the cup burner. In this section of the report, we discuss the experimental approach used for assessing the performance of these compounds in the cup burner, and present the early work with $Fe(CO)_5$ added to the fuel or air stream at fixed mole fractions. We then discuss experiments with TMT, MMT, $Fe(CO)_5$, Br_2, and CF_3Br added to cup-burner flames at varying mole fractions. While CF_3Br and Br_2 were both found to be very effective at all mole fractions for reducing the amount of CO_2 required to extinguish the cup-burner flames, all of the organometallic agents were found to be relatively ineffective, overall, at reducing the amount of CO_2 required. While they are several times more effective than CF_3Br at low mole fractions, they lose their effectiveness before an appreciable reduction of the CO_2 required for extinction occurs. Moreover, the performance benefit of these agents over CF_3Br at the low mole fraction is much less than that in premixed or counterflow diffusion flames. These results highlight the importance of flame type for assessing the performance of chemically active suppressants. Details of this investigation are presented below.

3.4.2. Background

As discussed above, metal compounds have attracted attention because it has been found that some metals recombine radicals in the post-combustion region of premixed H_2/O_2 flames [17] and that several metallic compounds are one to two orders of magnitude more effective than CF_3Br at reducing the burning velocity of premixed flames [10-12,24,81]. If means could be found to incorporate such super-effective moieties in a practical fire suppressant (particularly for unoccupied spaces), very effective agents may be possible.

Premixed and counterflow diffusion flames have been used extensively for testing super-effective agents since they provide easily measurable parameters which can be directly related to the effect of the agent on the overall reaction rate. For these super-effective agents, however, few detailed studies have been conducted in flames resembling fires. The present work remedies this deficiency by presenting results for addition of these highly effective agents to cup-burner flames. Not only do cup burners have flame structures that are a reasonable approximation to those in fires, but they are also widely used by the fire protection industry as a metric to assess fire suppressant performance [82]. Hence, measurements of agent performance in cup burners have clear relevance to their eventual use. In the results described below, the catalytic agents are found to be surprisingly poor flame inhibitors in cup burners, relative to CF_3Br. Experimental results are presented which delineate the performance of these agents, and provide an initial explanation of their lack of effectiveness.

As described above in other sections of the report, the agents TMT, MMT, ferrocene, and iron pentacarbonyl ($Fe(CO)_5$) have recently been studied in some detail [11,12,48]. Experiments and modeling of $Fe(CO)_5$ have quantified its performance and explained its mechanism of inhibition for a variety of conditions [36,48,83]. For iron, the strong inhibition is believed to occur from a catalytic radical recombination cycle involving iron oxides and hydroxides: FeOH + H $\leftrightarrow$ FeO + H_2 ; FeO + H_2O $\leftrightarrow$ $Fe(OH)_2$; and $Fe(OH)_2$ + H $\leftrightarrow$ FeOH + H_2O, which yields the net reaction: H + H $\leftrightarrow$ H_2. For manganese-containing inhibitors, the mechanism is believed to be similar (with Mn replacing Fe in the reaction sequence). At low volume fractions, $Fe(CO)_5$ is about eighty times more effective than CF_3Br at reducing the burning velocity of premixed flames; however, at volume fractions above about 100 µL/L, the marginal effectiveness of $Fe(CO)_5$ is greatly reduced. This is believed to occur from condensation of the active iron-containing intermediates to particles [37]. In a similar fashion, MMT loses its effectiveness at about 300 µL/L, and TMT, which is about three times as effective as CF_3Br in premixed flames, loses its marginal effectiveness at about 3000 µL/L. Indeed, if added directly to a cup-burner flame alone, $Fe(CO)_5$ is not expected to be a particularly effective suppressant because condensation of active iron-containing intermediates to particles limits their gas-phase volume fraction, restricting the potential of the gas-phase catalytic cycle. Any practical fire suppressant using these super-effective agents would require some method to overcome the loss of effectiveness.

One approach for overcoming the loss of effectiveness is to combine catalytic agents with inert compounds. In this case, the overall reaction rate is lowered in part through radical recombination by the catalytic agent, and in part through the lower temperature caused by the added diluent. This approach has been discussed in work since the 1950's [36,53,61,72,84,85] which suggested that combinations of thermally acting and catalytic agents might prove beneficial. These predictions have been confirmed in various studies with premixed and counterflow diffusion flames inhibited by $Fe(CO)_5$ [10], ferrocene [11], CF_3Br [86], phosphorus compounds [9], and alkali metals [87]. Tests and calculations show that addition of an inert compound lowers the temperature and in some cases, enhances the performance of the catalytic agent [11]. The goal is to harness the very high efficiency of the metal species at low volume fraction while keeping its concentration below that which causes condensation. Nonetheless, it is generally not known *a priori* if the combination of an inert agent with the catalytic agents will be effective in a particular flame configuration. For example, the lower temperature (because of the inert additive) can cause higher radical superequilibrium [48], increasing the catalytic effect, but may also modify the flame structure, providing larger residence times for particle formation [37].

Based on these encouraging results, extinction experiments of ferrocene together with an inert compound generated by a solid propellant gas generator (SPGG) have recently been conducted in an enclosure containing a spray flame [88]. Unfortunately, the combination did not have the intended high efficiency. Not withstanding, few carefully controlled tests have been performed in cup-burner flames for agents more effective than CF_3Br. In order to gain insight into reasons for the lack of effectiveness of the ferrocene/SPGG combination in suppressing the spray flame and to provide data in a low-strain diffusion flame similar to a fire, we performed experiments with catalytic metal-based inhibitors and CO_2 added to the air stream in a cup burner.

The approach adopted for assessing the effectiveness of the catalytic agents in extinguishing cup-burner flames is to determine how the CO_2 volume fraction at extinction changes in the presence of the catalytic inhibitor. This approach is conceptually the same as the classic oxygen index test used for assessing material flammability [89]. In that test, the oxygen volume fraction in the air stream at extinction (i.e., the oxygen index) is determined for solid, liquid, or gaseous fuels with chemical additives in either the fuel or oxidizer. In the present tests, CO_2 (rather than N_2) is added as the diluent to facilitate comparisons with existing experimental data for other configurations. Although previous studies have been performed with heptane, methanol, and mathane as the fuel [1], the present experiments use methane. A gaseous fuel allows an approximately constant flame size and heat release rate, preserving many properties of the flow field (unlike a liquid pool fuel, for which fuel supply rate varies with inhibitor addition). These methane-air flames with CO_2 are also essentially non-sooting, which is desirable since the metal additives would change the production rates of soot (and thus the radiant heat transfer) which would complicate interpretation of the results. The iron, tin, and manganese compounds were selected because there exists recent experimental data on their performance in premixed methane-air flames for comparison, as described in section 3.2 above.

3.4.3. Experiment

The cup burner, described previously [90,91] , consists of a cylindrical glass cup (28 mm diameter) positioned inside a glass chimney (53.3 cm tall, 9.5 cm diameter). To provide uniform flow, 6 mm glass beads fill the base of the chimney, and 3 mm glass beads (with two 15.8 mesh/cm screens on top) fill the fuel cup. Gas flows were measured by mass flow controllers (Sierra 860) which were calibrated so that their uncertainty is 2 % of indicated flow. To determine the extinction condition, the desired amount of catalytic agent was added to the co-flowing air (held constant at 41.6 L/min), and CO_2 was added to the flow (in increments of < 1 % near extinction) until lift-off was observed. The test was repeated at least three times.

The organometallic inhibitors were added to the air stream using multi-stage saturators in controlled temperature baths. As described above, the $Fe(CO)_5$ and TMT used two-stage saturators, [36]while the MMT used a three-stage saturator, with 50 % larger stages, to insure saturation. A measured portion of the added CO_2 flowed as a carrier through each saturator. The volume fraction of the organometallic inhibitors in the air stream was calculated based on the measured air flow, measured carrier gas flow, and calculated vapor pressure of the agent at the bath temperature. The experimental vapor pressure data was obtained from refs. [39,40]. Since the vapor pressure of MMT is much lower than that of the other agents, the burner and lines were maintained at >(35.0 ± 0.5) °C before and during the tests to reduce the likelihood of MMT condensation. [36]For bromine as the inhibitor, all flow tubes downstream of agent addition as well as the burner base were made of Teflon to avoid reaction. A computer-controlled syringe pump added the liquid Br_2 to a 2.1 m long tubing carrying the air and CO_2, and complete Br_2 evaporation was observed to occur within a tubing length of less than 1 m.

The fuel gas is methane (Matheson UHP, 99.9 %), and the air is house compressed air (filtered and dried) which is additionally cleaned by passing it through an 0.01 µm filter, a carbon filter, and a desiccant bed to remove small aerosols, organic vapors, and water vapor. The chemicals used were $Fe(CO)_5$ (Aldrich), TMT (Alfa Aesar), MMT (Alfa Aesar), CH_3OH (Aldrich, 99.8 %), Br_2 (Aldrich, 99.5 %), CF_3Br (Great Lakes), N_2 (boil-off), and CO_2 (Airgas).

An uncertainty analysis was performed, consisting of calculation of individual uncertainty components and root mean square summation of components. All uncertainties are reported as *expanded uncertainties:* $X \pm ku_c$, from a combined standard uncertainty (estimated standard deviation) u_c, and a coverage factor $k = 2$. Likewise, when reported, the relative uncertainty is ku_c / X. The expanded relative uncertainties for the experimentally determined quantities in this study are: CO_2 volume fraction, 4 %; inhibitor volume fraction for organometallics, CF_3Br, and Br_2: 5 %, 2.7 %, and 2.0 %, respectively.

3.4.4. Results and Discussion

We first review seom test results presented in a prior NGP final report [1]. In those early tests, the amount of CO_2 required for extinction of the cup-burner flame was determined with $Fe(CO)_5$ added to either the air or methane stream. Table 5 summarizes the results. The top line shows that for CO_2 alone, the volume fraction for extinction $X_{CO_2,ext}$ is (15.7 ± 0.6). The next two lines show that addition of $Fe(CO)_5$ to the air stream at relatively high volume fractions (450 µL/L or 924 µL/L) causes only a (9.6 ± 0.5) % or (13.5 ± 0.8) % reduction in $X_{CO_2,ext}$. If we add 1 % CH_4 to the air stream to change the flame location and hence the scalar dissipation rate, the reduction in $X_{CO_2,ext}$ with addition of 450 µL/L of $Fe(CO)_5$ is slightly greater, but still only about (10.7 ± 0.6) *Yo*. Likewise, addition of $Fe(CO)_5$ to the fuel stream at either 450 µL/L or 4500 µL/L causes only a (1.3 ± 0.1) *Yo* or (2.6 ± 0.2) % reduction in the amount of CO_2 required for extinction. These results were completely unexpected since only 100 µL/L of $Fe(CO)_5$ in a premixed flame halves the burning velocity [11]. Hence, the higher volume fractions of $Fe(CO)_5$ added here were expected to strongly influence $X_{CO_2,ext}$.

Table 5 - Extinction volume fraction of CO_2 $X_{CO_2,ext}$ in methane-air cup burner with and without various amounts of $Fe(CO)_5$ or CF_3Br added to the fuel or air stream (air flow =41.6 L/min) (from ref. [1]).

Catalytic Inhibitor	X_{inh} (µL/L)	Inhibitor Location	$X_{CO_2,ext}$ (%)	% Reduction from Pure CO_2
None	-		15.7 ± 0.6	
$Fe(CO)_5$	450 µL/L	in Air	14.1 k0.6	9.6 ± 0.5
"	924 µL/L	" "	13.5 k0.5	13.5 ± 0.8
"	450 µL/L	in Air w/ 1% CH_4	14.0 ± 0.6	10.7 ± 0.6
	450 µL/L	in Fuel	15.4 f 0.6	1.3 ± 0.1
	4500 µL/L	" "	15.2 ± 0.6	2.6 ± 0.2
CF_3Br	1.3%	in Air	4.4 ± 0.2	72.0 ± 4.1
"	11. %	in Fuel	8.7 f0.3	44.2 k2.5

CF_3Br is also believed to be a strong catalytic radical scavenging agent. As a test of the validity of the present approach, $X_{CO_2,ext}$ was determined with CF_3Br added, to either the fuel or air stream, at a volume fraction which would halve the burning velocity of a premixed flame. These results are shown at the bottom of Table 5. In contrast to the results with $Fe(CO)_5$, addition of CF_3Br to either stream has a large effect on $X_{CO_2,ext}$, a reduction by factor of two to three. Clearly, CF_3Br and $Fe(CO)_5$ behave differently in the cup burner with respect to their ability to reduce the CO_2 requirement for extinction.

The results in Table 5 [1] may lead one to conclude that although $Fe(CO)_5$ is highly effective in premixed flames, it has little effect in cup-burner flames. Conducting cup-burner extinction tests with added CO_2 for a *continuous* range of concentrations of $Fe(CO)_5$ in the air stream, however, shows that $Fe(CO)_5$ does, in fact, inhibit the flame. Figure 21 shows the volume fraction of CO_2 required for extinction as function of the initial volume fraction of the catalytic inhibitor in the air stream (prior to CO_2 addition). Data are presented for $Fe(CO)_5$, as well as for the organometallic agents TMT and MMT. For comparison, tests were also performed for Br_2 and CF_3Br. For extinction of these methane-air flames, pure CO_2 is required in the air stream at volume fraction of (15.7 ± 0.6) %, whereas CF_3Br, a catalytic agent, is required at (2.4 ± 0.1) %. Moreover, as Figure 21 shows, adding CF_3Br at volume fractions below the extinction value greatly reduces the amount of CO_2 required for extinction. For example, adding half of the extinction value of CF_3Br reduces the amount of CO_2 required by 70 %. The curvature in the line for CF_3Br in Figure 21 indicates that, as described previously [85], the combination of CF_3Br and CO_2 is synergistic; that is, when combined, less of each is required for extinction than one would expect based on a linear interpolation of the individual results.

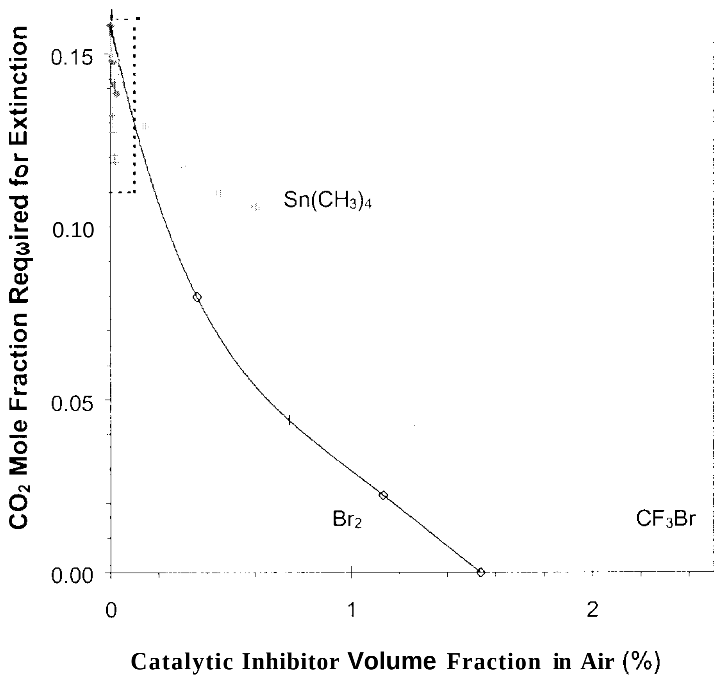

Figure 21 – Volume fraction of CO_2 required for methane-air cup-burner flame extinction as a function of catalytic inhibitor volume fraction, CF_3Br, Br_2, $Fe(CO)_5$, TMT, MMT, or a blend of the last three. The boxed region in the upper left is expanded in Figure 22.

Figure 22 shows the data for the organometallic agents in more detail, and indicates that at low volume fraction, the organometallic agents are actually *more* effective than CF_3Br. For the sequence CF_3Br, TMT, $Fe(CO)_5$, and MMT, the relative magnitude of the slopes of the curves (at low volume fraction) are 1, 2, 4, and 8, so that $Fe(CO)_5$ is about four times as effective as CF_3Br. While this performance is noteworthy, it is far less than was observed in premixed flames or counterflow diffusion flames, for which the benefit was one to two orders of magnitude for $Fe(CO)_5$ as compared to CF_3Br. Also, the relative performance of $Fe(CO)_5$ and MMT is switched, with $Fe(CO)_5$ about twice as effective as MMT in premixed flames, while the opposite is true for the present cup-burner flames. Especially apparent in Figure 22 is that the curve for each of the three agents, TMT, $Fe(CO)_5$, and MMT, all have a decreasing slope as their volume fraction increases. This behavior is similar to that in premixed and diffusion flames in which the loss of effectiveness was believed to be due to condensation of active species.

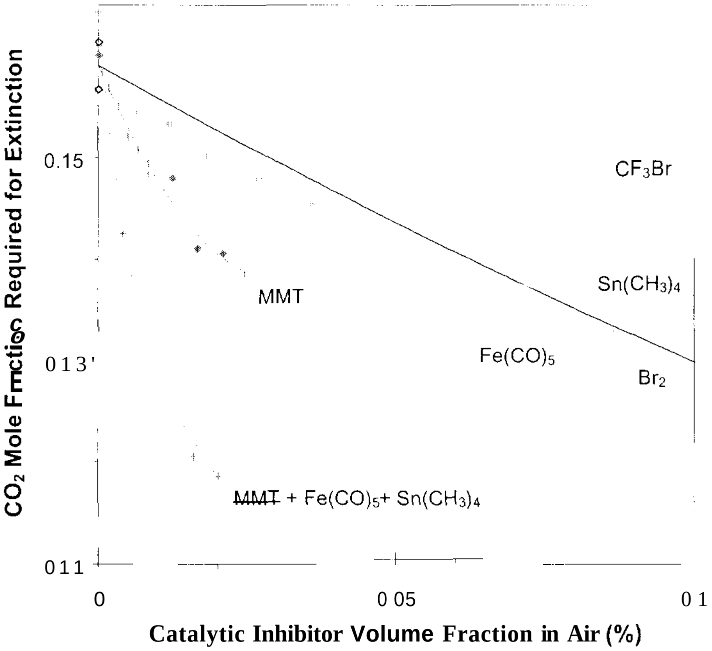

Figure 22 – Data of Fig. 1 with expanded x- and y-axis to show influence of metallic inhibitors in more detail.

In previous work it has been argued that to obtain good performance by the super-effective agents, it might be possible to add small, non-condensing amounts of several catalytic agents together with an inert agent [36]. We tested this claim by adding a blend of the three catalytic metals MMT, $Fe(CO)_5$, and TMT to the air stream and then finding $X_{CO_2,ext}$. The bottom curve in Figure 22 shows $X_{CO_2,ext}$ for such a blend. MMT, $Fe(CO)_5$, and TMT are present in the molar ratio 1:2.1:15.5, and the curve is plotted as a function of the MMT volume fraction. Note that at the test point of the highest volume fraction, the three agents are added at 200 µL/L, 420 µL/L, and 3100 µL/L, respectively. (These values were selected since the individual curve for each agent is roughly linear up to these volume fractions; i.e., they have not yet lost their marginal effectiveness). As shown, the agents do work together to reduce the amount of CO_2 required for extinction, and, up to the maximum volume fractions added, the blend does not drastically lose its effectiveness. Amazingly, with addition of *three* catalytic inhibitors, *each* at a volume fraction which would easily reduce the overall reaction rate in a premixed flame by a factor of four, and each at a volume fraction at which the agent alone is not believed to lead to condensation, the combination still reduces the amount of CO_2 required for extinction by only 25 %.

Although the organometallic compounds *are* effective at reducing the amount of CO_2 required for cup burner extinction as compared to CF_3Br, their relative performance is drastically poorer than one would expect based on their behavior in premixed flames, and it is of interest to try to understand why. Two possible causes of the loss of effectiveness are the same as were discussed previously for premixed and counterflow diffusion flames, namely: 1.) saturation of the catalytic cycles and 2.) condensation of active gas-phase species. The saturation of the catalytic cycles is defined as a state in which the chain-carrying flame radicals have already been reduced to near equilibrium levels, so that additional catalytic inhibitor has no further benefit. This explanation of the lack of effectiveness is deemed to be unlikely, based on two results shown in Figure 21: those for Br_2, and those for the blend of MMT, $Fe(CO)_5$, and TMT. The experiments with Br_2 were designed to test the action of a catalytic agent without the confounding effects of condensation of inhibiting species. Further, it is an improvement over tests with CF_3Br for this purpose, since CF_3Br, because of its carbon content and use at relatively high volume fraction (>2 %), can have fuel-like behavior, moving the flame location, changing the scalar dissipation rate, and affecting the extinction condition. Bromine, added at half the volume fraction, and having no reducing species, does not have a fuel effect. As Figure 21 shows, the curve for Br_2 is linearly decreasing in the region where the other curves are starting to flatten out—that is, it keeps working, implying radical depletion is not the cause of the loss of effectiveness of the metals (otherwise, Br_2 would stop working at about the same value of $X_{CO_2,ext}$). The data for the blend of metallic inhibitors shows a similar result. If each of the agents added alone was losing its effectiveness due to radical depletion, adding a second (or third) catalytic agent to the mix would not provide additional inhibition (since radicals are already reduced to their equilibrium levels). In the bottom curve of Figure 22, however, the blend of all three agents clearly shows additional inhibition over MMT alone, providing evidence against saturation of the radical scavenging by the metals.

Particle formation is more likely the cause of the degraded performance of the metal agents. Evidence to support this is that the approximate agent volume fraction for the loss of effectiveness is an order of magnitude higher for TMT (4000 µL/L) than for the iron or manganese (400 µL/L) (as occurs in premixed flames) [12], which is consistent with the higher vapor pressure for the tin compounds. Also, the manner in which Fe-, Sn- and Mn-containing compounds lose their effectiveness in premixed flames [12] is comparable to that indicated in Figure 22. Finally a visible outer annulus, apparently particles, was observed in all flames with added metals, and the blackbody radiation from that region increased with higher agent volume fraction.

3.4.5. Conclusions

The first data on the extinction characteristics of highly effective catalytic agents at varying volume fraction added with CO_2 to a cup burner flame of methane and air have been measured. Although such catalytic agents have previously been found to be very effective in premixed and counterflow diffusion flames, they are surprisingly ineffective in cup-burner flames. At low mole fraction, the metallic agents are still more effective than CF_3Br at reducing the amount of CO_2 required for extinction, but their relative performance benefit is much less than in premixed flames. The experiments have shown that for reducing the amount of CO_2 required for extinction, the order of increasing performance is: CF_3Br, TMT, $Fe(CO)_5$, and MMT. Hence, the relative performance of $Fe(CO)_5$ and MMT are switched relative to premixed flames. Further, a combination of three organometallic catalytic agents, each at a volume fraction which should reduce the overall reaction rate by a factor of four, reduced the amount of CO_2 required for extinction by only 25 %, a result which was strikingly unexpected. At higher volume fractions, each of the metal-based agents experienced a loss of effectiveness which is reminiscent of their behavior in premixed flames. In contrast, the agent Br_2 was effective alone or in combination with CO_2, with a performance improvement over CF_3Br of about a factor of two. The relative performance of these very powerful flame inhibitors has been found to be highly dependent upon the type of flame configurations used for the tests.

The loss of effectiveness of the organometallic agents is believed to be caused by particle formation. To more accurately detect the particles, we conducted laser-scattering experiments in the cup-burner flames with and without added $Fe(CO)_5$. These experiments are described below, after first reviewing the insight gleaned from previous measurements of particles in premixed and counterflow experiments.

3.5. Laser Scattering Experiments of Particles in $Fe(CO)_5$-Inhibited Flames

3.5.1. Introduction

Particle formation is believed to be responsible for the loss of effectiveness of organometallic agents in cup-burner flames. A significant amount of previous research has been conducted to understand the loss of effectiveness of $Fe(CO)_5$ in both premixed and counterflow diffusion flames. In that work, the particle formation was measured and correlated with the loss of effectiveness, and the parameters which most affected the particle formation were discussed. In this section of the report, we present work in which those techniques used in premixed and counterflow diffusion flames were extended to cup-burner flames inhibited by $Fe(CO)_5$.

This section of the report describes laser scattering experiments used to measure the particles in cup-burner flames. The presentation of these new data is relatively straightforward; however, in order to interpret the new results, it is useful to first review the important findings of the measurements and analyses from premixed and counterflow diffusion flames.

3.5.2. Background

At low volume fractions, $Fe(CO)_5$ is about eighty times more effective than CF_3Br at reducing the burning velocity of premixed flames, MMT forty times, and TMT three times. Kinetic modeling of the flame inhibition has lead to an understanding of the reasons why these metallic agents differ in their effectiveness. Both manganese monoxide and iron monoxide can react with H_2O to form the stable di-hydroxide intermediate (e.g., $Fe(OH)_2$ and $Mn(OH)_2$), which can then react with H atom directly. Conversely, the di-hydroxide of tin has not been observed for the present conditions. The intermediate species SnO relies upon a three-body reaction with H atom to form the hydroxide, and the reaction is rate-limiting and slow. Further, iron is superior to manganese in premixed flames because the equilibrium for the reaction $FeO + H_2O \leftrightarrow Fe(OH)_2$, unlike the equivalent relation for manganese species, favors the di-hydroxide, so it can exist in high concentrations to react with H atoms.

For premixed flames, all of these organometallic agents lose their effectiveness at relatively low volume fractions. For $Fe(CO)_5$, there is a very large change in its effectiveness at about 100 μL/L. This is believed to occur from condensation of the active iron-containing intermediates to particles [37]. In a similar fashion, MMT loses it's effectiveness at about 300 μL/L, and TMT loses its marginal effectiveness at about 3000 μL/L. Indeed, if added directly to a cup-burner flame alone, $Fe(CO)_5$ is not expected to be a particularly effective suppressant because condensation of active iron-containing intermediates to particles limits their gas-phase volume fraction, restricting the potential of the gas-phase catalytic cycle. Any practical fire suppressant using these super-effective agents would require some method to overcome the loss of effectiveness.

The primary motivation of the present work is to describe the effect of particle formation on flame inhibition. Laser-light scattering experiments are used to determine the particle formation region and to estimate the particle size. The premixed flame experiments use Bunsen-type flames of CH_4-O_2-N_2 and CO-H_2-O_2-N_2, and in those flames, thermophoretic sampling with transmission electron microscopy provide the particle size and morphology. By making proper choices of concentrations and gas flows, the effects of both flame temperatures and residence time on particle formation are studied. The unresolved issue of whether the inhibition is heterogeneous or homogeneous is addressed, and results are presented for inhibition by an ideal heterogeneous inhibitor. We also present data on particle formation in counterflow diffusion flames of methane and air (with agent addition to either the fuel or air stream), and cup-burner type co-flow diffusion flames of methane and air with TMT, MMT, and $Fe(CO)_5$ added to the air stream together with CO_2. The longer residence time diffusion flame burners demonstrate the roles of particle formation and flow field effects in the loss of active species from the gas-phase inhibiting region of the flame.

3.5.3. Experiment

Three flame types were tested with the organometallic inhibitors: premixed, counterflow diffusion, and co-flow diffusion flames. The burners used to produce these flames are described below, along with the common gas-handling system and the optical system used for particle detection. The thermophoretic sampling system for collection of the nanoparticles (subsequently analyzed by transmission electron microscopy) is also described. These are followed by discussion of measurement uncertainty.

3.5.3.1. Burners

The premixed burner system, described previously [10] and in section 3.2.2. above[35,36], has been used for flame speed measurements using the total area method [34]. Premixed flames ($\phi=1.0$) were stabilized on a Mache-Hebra nozzle burner (inner diameter 1.02 cm ± 0.005 cm) [92] with an air co-flow. The burner produces a steady, straight-sided, conical, non-sooting flame with a height of 13 mm. The burner and annulus for the co-flowing air were housed in an acrylic chimney with three optical access holes. Rubber bellows connect the chimney with the adjacent optical elements to provide a flexible and airtight seal. The premixed flame conditions correspond to those of the $Fe(CO)_5$ inhibition measurements described in Refs. [10] and [36].

The counterflow burner system has been described previously [10,93]. The fuel and oxidizer tubes (22.2 mm diameter) are separated by 11 mm, and there is a nitrogen shroud flow from a concentric annulus (51 mm diameter) around the bottom (oxidizer) jet. The burner produces a non-sooting flame with a flat region in the center. The strain rate a (the derivative of the velocity with respect to the axial position) is approximated from the outer flow jet exit velocities as $a=\left(2|V_O|/L\right)\left(1+|V_F|\sqrt{\rho_F}/|V_O|\sqrt{\rho_O}\right)$, where L is the jet separation distance, V_i is the velocity of gas i (F=fuel, O=oxidizer), and ρ_i is the density of gas i [71]. The jet exit velocities were chosen so that the momentum of the two streams were balanced at all values of the strain rate; that is, $\rho_F V_F^2=\rho_O V_O^2$.

The cup burner, described previously [90] and in section 3.4.3. above[91], consists of a cylindrical glass cup (28 mm diameter) positioned inside a glass chimney (53.3 cm tall, 9.5 cm inner diameter). To provide uniform flow, 6 mm glass beads fill the base of the chimney, and 3 mm glass beads (with two 15.8 mesh/cm screens on top) fill the fuel cup. The traditional cup-burner was modified slightly for optical access. To prevent laser light from scattering off of the cup-burner chimney walls, the round cup-burner chimney was cut off to a height 2 mm below the fuel cup rim and a second. square chimney (as in the premixed flame experiments described above), with an additional co-flow of air, enclosed the round chimney and burner.

The organometallic inhibitors were added to the flames using multi-stage saturators in controlled temperature baths. The $Fe(CO)_5$ and TMT used two-stage saturators of a design described previously [36] and in section 3.4.3. above, while the MMT used a three-stage saturator, with

50 % larger stages, to insure saturation. A measured portion of the added carrier gas (N_2, CO_2, or CH_4) flowed in series through the saturators, and was then added to the bulk flow of that gas. The volume fraction of the organometallic inhibitors in the air stream was calculated based on the measured bulk flow, measured carrier gas flow, and calculated vapor pressure of the agent at the bath temperature. The experimental vapor pressure data was obtained from refs. [39-41]. Tests to validate the assumption of agent saturation in the carrier gas have been described previously [36].

Gas flows were measured with digital mass flow controllers (Sierra Model 860) with a claimed repeatability of 0.2 % and accuracy of 1 % of full-scale flow, which have been calibrated with piston, bubble, and dry flow meters so that their accuracy is 1 % to 2 % of the indicated flow. The fuel gases were methane (Matheson UHP), carbon monoxide (Matheson UHP) and hydrogen (Matheson UHP). The oxidizer consisted of nitrogen (boil-off from liquid N_2) and oxygen (MG Industries), or air, from house compressed air (filtered and dried) which was additionally cleaned by passing it through an 0.01 µm filter, a carbon filter, and a desiccant bed to remove small aerosols, organic vapors, and water vapor. All experiments were performed at ambient pressure. The chemicals used were $Fe(CO)_5$ (Aldrich), TMT (Alfa Aesar), MMT (Alfa Aesar), and CO_2 (Airgas).

3.5.3.2. Optical System

Light-scattering and extinction techniques with phase-sensitive detection were used to determine particle location and properties. The apparatus, shown in Figure 23, is similar to those used by other researchers [94,95]. The light source is a 4-W argon-ion laser (Spectra Physics BeamLok 2060), with a vertically-polarized 2.2-W beam at 488 nm. A mechanical chopper (Stanford Research 640) modulates the beam at 1500 Hz and provides a reference signal for the lock-in amplifiers. A polarization-preserving single-mode optical fiber (3 µm diameter) carries the light into a chemical fume hood (90 cm x 150 cm x 150 cm) which contains the burner. At the fiber output, collimating optics, a polarization rotator, mirrors and a focusing lens (f = 250 mm) deliver the laser light to the test region. A glass wedge between the polarization rotator and the focusing lens diverts a small fraction of the beam to a reference detector which monitors the laser power during the experiments. The transmission efficiency for the laser-to-fiber coupling system is only about 15 %, but this provides sufficient power for the experiments. The steep temperature gradients in the present flames cause significant beam steering and distortion. These effects, if unmitigated, would produce fluctuations of a few percent in the measured transmissivity, which is approximately the same magnitude as the peak absorptivity (< 2 %). To reduce the beam steering effect in the premixed and counterflow diffusion flame burners, wc follow an approach used by Dibble [96] and Nguyen [97], which involves reflecting the beam back through the flame along the same path, thus “unsteering” it. The approach has the additional benefit of doubling the path length and nearly doubling the laser light intensity at the focus. A concave spherical mirror (f=250 mm) reflects the beam back through the optical path and a glass wedge sends it to an integrating sphere. To spatially probe the flames, a three-axis translation stage (minimum step size of 0.0016 mm) positions the burner and chimney in the stationary optical path.

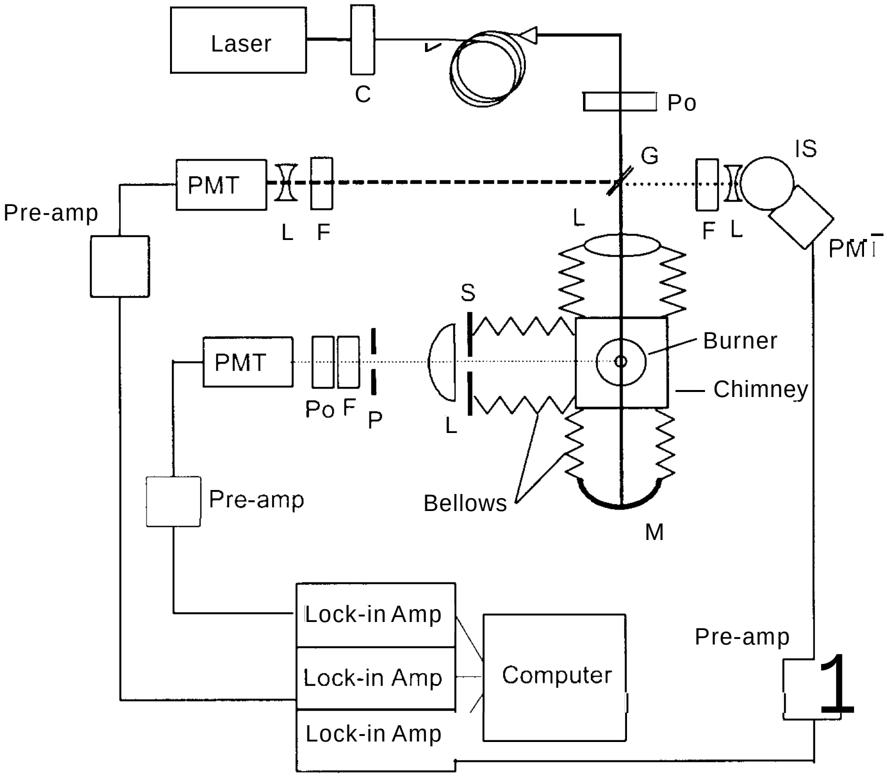

Figure 23: Schematic of laser scattering/extinction system: C, chopper; M, mirror; G, beam pick-off; L, lens; S, spatial filter (circular aperture); Po, polarizer; F, laser-line and neutral density filters; PMT, photomultiplier; P, pinhole; IS, integrating sphere (from ref. [37]).

The light detection system consists of three photomultiplier tubes (PMT, all type 1P28) with appropriate filtering. The reference PMT has neutral density filters and a laser-line filter (Δλ = 10 ± 2 nm). The detection system for light scattered normal to the laser beam consists of a circular aperture (5 mm diameter), collection lens (f = 100 mm), pinhole aperture (diameter 1 mm), laser-line filter, polarizer and PMT. For the 90'-scattered light, the circular aperture (5 mm diameter) located 10 cm from the laser beam focus provides a solid angle of 0.002 sr. The pinhole aperture (1 mm diameter) defines the length of the sample to be 1 mm based on unity magnification.

The signal from each of the detectors is pre-amplified (Stanford Research 552) before entering a lock-in amplifier (Stanford Research 530). A personal computer controls the amplifiers and records the measurements during the experiments using a data acquisition card (Strawberry Tree DynaRes Ultra 8). In the data acquisition software, each scattering or transmission data point is normalized by the reference signal. Typically, 100 readings are averaged over a time of about 1 second; post-processing software reduces the data and calculates uncertainty as described below. The measured quantities in the experiment are the voltage outputs of the reference, transmission, and scattered light detectors, and these depend on the system geometry, optical efficiencies, detector responsivity, gas density and particle number density, and the scattering cross section of the gases or particles. To obtain the scattering cross section (Q_{vv}) of the gases or particles in the flame, a calibration of the optical system efficiency is performed using a gas with known scattering cross section [98,99] (ethylene is used because of its relatively large cross section). The scattering and transmission signals are measured for the calibration gas to give a calibration factor, $C = Q_{vv,cal}\frac{\tau_{cal}}{S_{vv,cal}}$, where $Q_{vv,cal}$ is the known scattering cross section of the calibration gas, τ_{cal} is the transmissivity of the calibration gas, and $S_{vv,cal}$ is the scattering signal caused by the calibration gas. Given the calibration constant and scattering measurements, the scattering cross section at each location can be found as $Q_{vv} = C\frac{S_{vv}}{\tau_{\lambda}}$, where S_{vv} is the measured scattering signal and τ_{λ} is the transmissivity of the flame gases and particles.

3.5.3.3. Thermophoretic Sampling

Thermophoretic sampling with transmission electron microscopy (TEM) is used as a supplemental technique to determine particle size and morphology. The procedure and apparatus are similar to those used by Dobbins and Megaridis [100] and Koylu et al. [101]. A computer-controlled, double-acting piston with travel of 5.08 cm quickly inserts and removes the electron microscope grid from the flame. Transit times and the dwell time in the flame were measured using a laser, mirror, photodiode, and oscilloscope [101]. Each grid is attached to a stainless steel substrate with thickness of 0.4 mm, and height between 3 mm to 5.7 mm. The EM grids are copper with a carbon film deposited on one side (Electron Microscopy Sciences p/n CFH4-SPEC-CU), and are fastened onto the metal substrates using adhesive or double-sided tape.

3.5.3.4. Uncertainty Analysis

The uncertainty analysis consists of calculation of individual uncertainty components and their root mean square sums [102]. All uncertainties are reported as *expanded uncertainties:* $X \pm U$, where U is ku_c, and is determined from a combined standard uncertainty (estimated standard deviation) u_c, and a coverage factor $k = 2$ (level of confidence approximately 95 %). Likewise, when reported, the relative uncertainty is $U / X \cdot 100$ %, or $ku_c / X \cdot 100$ %.

The expanded relative uncertainties for the experimentally determined quantities in this study are as follows: 6.5 % to 11.5 % for $Fe(CO)_5$ volume fraction, 1.4 % for equivalence ratio, 1.1 % for oxygen mole fraction, 1.2 % for hydrogen mole fraction in the reactants, and between 1 % and 5 % for normalized burning velocity and 2 % to 5 % for the normalized extinction strain rate (the *normalized* burning velocity is defined as the burning velocity of the inhibited flame divided by the burning velocity of the uninhibited flame, and like wise for the extinction strain rate). For the scattering measurements, the combination of slight fluctuations in the flame position, small particle scattering cross section, steep spatial gradients in the flame, and system noise cause the scattering signal to vary about a local mean value at any given location. The expanded relative uncertainty of the Q_{vv}, for the premixed and counterflow diffusion flames is no more than 10% of the mean in the particle zone and no more than 20% of the mean in the unburned reactants. The expanded relative uncertainty in the extinction volume fraction for CO_2 added to the cup burner is 4 %, and for the added organometallic agents, CF_3Br, and Br_2, 5 %, 2.7 %, and 2 %, respectively.

3.5.4. Results and Discussion

3.5.4.1. Premixed Flames(ϕ=1.0)

3.5.4.1.1. Scattering Measurements

The premixed methane-air Bunsen-type flame with $Fe(CO)_5$ added to the reactant stream showed a scattering signal which varied greatly with the position in the flame [37]. Figure 24 shows the scattering signal as a function of distance from the burner centerline along a horizontal profile 7 mm above the burner base. At this measurement height, the Bunsen cone has a radius of about 2.3 mm (the diameter of the burner exit nozzle is shown at the base of the figure). As the figure shows, there are two scattering peaks within the flame region (one for each side of the Bunsen cone). Far outside the flame region (i.e., downstream of the flame in the product gases), the scattering signal is two orders of magnitude larger than the in-flame signal, indicating very large or numerous particles. These downstream particles have little consequence for the flame inhibition by iron species; instead, it is the in-flame particles which affect the performance of $Fe(CO)_5$ in this flame, and we concentrate our discussion on the in-flame particles.

5

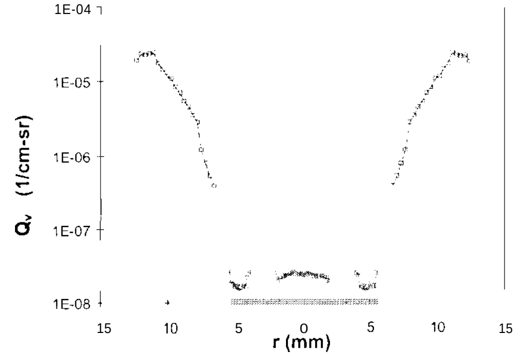

Figure 24: Scattering cross section Q_{vv} as a function of the radical distance r from the burner centerline at 7 mm height in stoichiometric CH_4-air flame with 200 µL/L of $Fe(CO)_5$ (from ref. 1371).

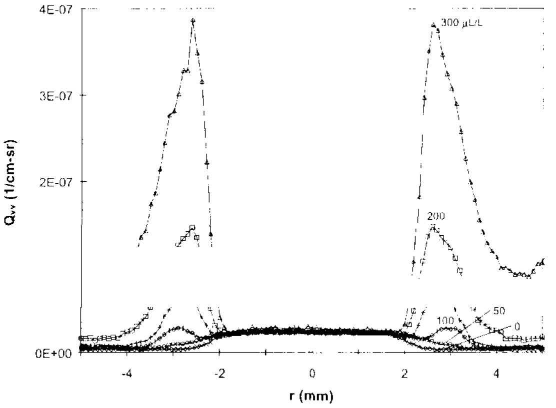

Figure 25: Measured scattering cross section through *a* stoichiometric CH_4-air flame 7 mm above the burner rim at various inhibitor mole fractions (from ref. [37]).

The in-flame particles are present near the region of peak reaction rate of H-atom, which is also near the region where the inhibiting species (FeO, FeOH, and $Fe(OH)_2$) are most active [103]. Hence, the particles can act as sinks for the inhibiting iron-containing intermediate species. As the particles are carried further into the flame, the temperature rises, and they disappear. Only very far downstream (r>6 mm) do the particles reappear, but this location is too far removed from the radical chain-branching region to have much effect on the burning velocity. For those large values of r, the velocity is decreasing, leading to a larger residence time, and the temperature is decreasing (due to heat losses and co-flow air entrainment); both of these effects can lead to the very large scattering signal at that location.

Figure 25 shows the in-flame particle region in more detail. Scattering data are shown for $Fe(CO)_5$ volume fractions in the reactant stream of (0, 50, 100, 150, 200, and 300) μL/L. The curve for 0 μL/L of inhibitor (the bottom curve in the figure) clearly shows the difference in scattering by the reactant and products species (which have a different density and composition). The scattering signal increases with increasing amounts of $Fe(CO)_5$.

Since the loss of effectiveness in premixed flames inhibited by $Fe(CO)_5$ was postulated to be caused by condensation of iron-containing intermediate species to particles, it is of interest to compare how the loss of effectiveness correlates with the particle scattering signal. The presence of particles is characterized by the height of the scattering peak above the background scattering caused by the gas-phase species at the same physical location in the flame (approximately the height of the peaks in Figure 25). Figure 26 shows data for the normalized burning velocity (left axis), and the maximum value of the in-flame scattering (right axis), as a function of the volume fraction of added $Fe(CO)_5$. To provide variation in the manner in which the inhibitor loses its effectiveness, curves are provided for two values of the oxygen mole fraction in the oxidizer $X_{O_2,ox}$, 0.21 and 0.244. Referring to the two curves for $X_{O_2,ox}$ = 0.21 in Figure 26, the value of the mole fraction of added inhibitor X_{inh} at which the great loss of effectiveness occurs (i.e., the slope changes dramatically) is about 100 μL/L, and this volume fraction also corresponds to the point at which the scattering signal starts to rapidly increase in magnitude. The curves for $X_{O_2,ox}$ = 0.244 indicate that loss of effectiveness of $Fe(CO)_5$ occurs at a higher value of X_{inh} than for $X_{O_2,ox}$ =0.21, and that the increase in particle scattering is also retarded until a larger quantity of $Fe(CO)_5$ is added. The curves in Figure 26 indicate that the formation of particles is correlated with a *loss* of effectiveness of $Fe(CO)_5$, rather than being associated with the strong inhibition itself.

Two features of the higher oxygen mole fraction flames may be causing the loss of effectiveness to occur at a higher value of X_{inh}. The larger value of $X_{O_2,ox}$ leads to a higher final temperature of the flame, which would hinder condensation, requiring a larger value of X_{inh} for an equivalent amount of scattering. Alternatively, the higher temperature flames have a higher flame speed, which provides a shorter residence time in the flame for particle inception and growth. In order to examine which of these effects is important for particle formation and loss of effectiveness of $Fe(CO)_5$, experiments with varying $X_{O_2,ox}$ and fuel type were conducted.

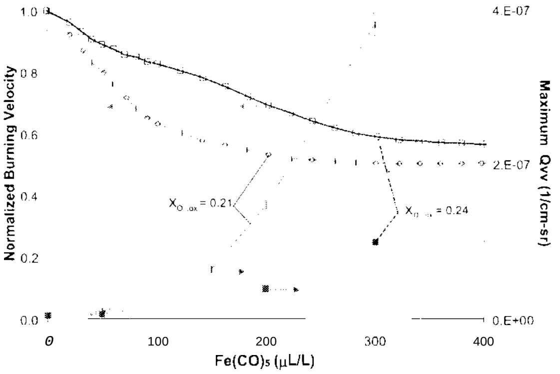

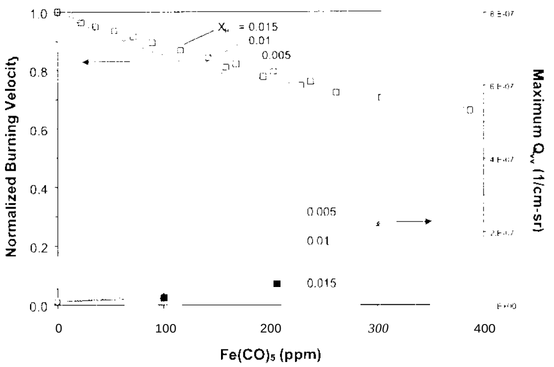

Figure 26: Normalized burning velocity (from Ref. [10]) and maximum Q_{vv} for ϕ=1.0 CH_4 flame with $X_{O_2,ox}$ = 0.21 and 0.24 (from ref. [37]).

Figure 27: Maximum scattering signal and normalized burning velocity (from ref. [36]) for CO-H_2 flames as $Fe(CO)_5$ concentration varies (from ref. [37]).

In order to obtain flames with nearly identical adiabatic flame temperatures but varying residence times (i.e., flame speeds) we conducted experiments with $CO/O_2/N_2/H_2$ mixtures, with varying hydrogen volume fraction. The normalized burning velocity and peak in-flame scattering signal for flames with H_2 volume fractions X_H, of 0.005, 0.010, and 0.015 are shown in Figure 27. As the figure shows, the flames with less H_2 (slower flames, longer residence times) lose their effectiveness at lower values of X_{inh}, and these flames also have particle scattering signals which rise faster at lower values of X_{inh}.

The data for a collection of experiments having a range of burning velocity and peak adiabatic flame temperature show the importance of residence time for particle formation. Figure 28 shows the peak in-flame scattering signal for methane and CO flames with varying peak temperature, burning velocity, and $Fe(CO)_5$ loading. Each solid line is a linear least-squared fit to all of the data at a certain value of X_{inh}, namely (100, 200, and 300) μL/L of $Fe(CO)_5$., which are noted by circles, diamonds, and squares, respectively. Within each data set for an inhibitor loading, the points correspond to: (h)igh, (m)edium, and (l)ow temperature, and CH_4 flames (open symbols) and CO flames (closed symbols). As Figure 28 shows, the scattering signal is clearly related to the burning velocity, which is inversely related to the residence time. Similar plots investigating the importance of peak flame temperature did not show its correlation with the scattering signal.

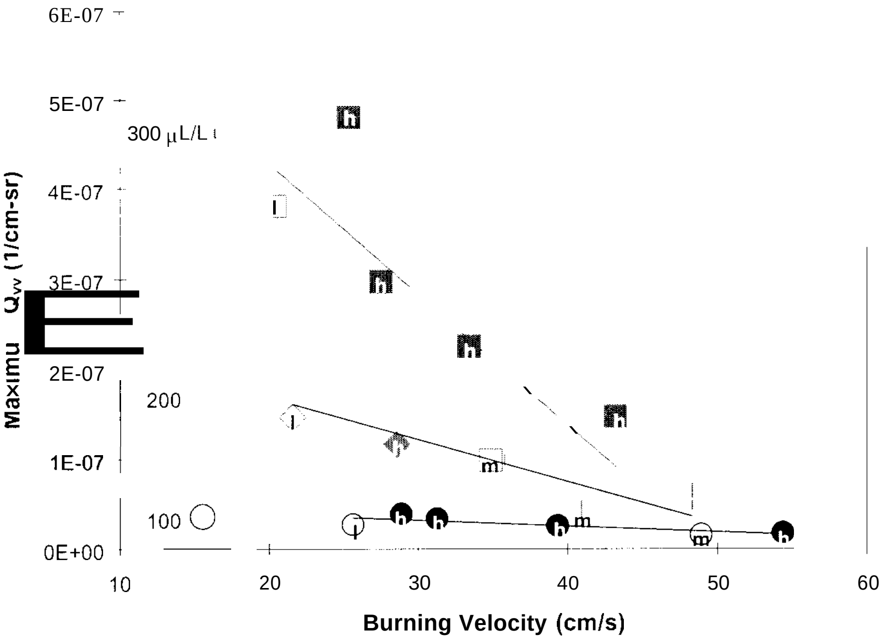

Figure 28: Maximum Q_{vv} for flames of CH_4 (open symbols) and CO (closed symbols) as a function of the burning velocity. The letters correspond to the adiabatic flame temperature (low, medium, and high, 2220, 2350, and 2370 K), while the symbol shape (square, diamond, and circle) corresponds to the loading of $Fe(CO)_5$: (100, 200, and 300) μL/L (from ref. [37]).

3.5.4.1.2. Particle Size and Morphology in Premixed Flames

Further insight into the particle properties can be extracted from the scattering signals (e.g.,Figure 25) by using other information available [37]. For example, we may assume that 50 % to 100 % of the iron in the feed stream condenses to particles. Previous calculations using a gas-phase only mechanism for the flame inhibition by $Fe(CO)_5$ were in good agreement for low mole fraction, but deviated once the inhibitor reached the mole fraction at which it lost its marginal effectiveness [48]. The amount of deviation corresponds to condensation of about 50 % of the available $Fe(CO)_5$ (X_{inh}=200 μL/L), and an upper limit of particle mass is obtained assuming 100 % condensation. Other reasonable assumptions (for estimation purposes) are that the particles are monodisperse Rayleigh scatterers composed of FeO. Using the scattering signals collected for 200 μL/L of added $Fe(CO)_5$, we estimate that for 50 % and 100 % condensation, the particles have, respectively, a volume fraction of 1.2×10^{-8} and 2.2×10^{-8}, diameter of 16 nm and 13 nm, and number density of 5.3×10^{9} cm^{-3} and 2.1×10^{10} cm^{-3}. Using the optical and bulk properties of Fe instead of FeO increases the inferred diameter by 15% and the number density by 9%.

For the counterflow diffusion flames, both laser scattering and laser extinction measurements were possible for some conditions. It was found [104], that for low strain rate flames, the particles have diameters between 10 nm and 30 nm, number densities of 10^8 cm^{-3} *to* 10^{10} cm^{-3}, and volume fractions of 10^{-7} to 10^{-8}. The mean diameter and volume fraction of the particles generally increased with increasing $Fe(CO)_5$ loading.

Additional information on the particle properties is obtained from thermophoretic sampling of the flames. For the premixed flames, the 3 mm-diameter TEM grid was inserted at a height of 7 mm above the burner rim, and at a location corresponding to the main reaction zone of the flame (r = (2.7 ± 0.3) mm). The image shown in Figure 29 corresponds to a dwell time of 375 ms in a flame with X_{in} = 200 μL/L. The particles show a moderate degree of agglomeration, with about 1 to 10 primary particles per agglomerate and primary particle sizes of under 20 nm. The primary particle diameters from the TEM images are in reasonable agreement with those estimated above from the scattering signal (assuming 50 % to 100 % of the iron species condense). These small diameters, 10 to 20 nm, support the possibility of particles evaporating as they convect to regions of higher temperature. Note that the larger agglomerates in the figure may have been collected as the TEM grid was insert into the flame, unavoidably passing into the region of very large or very numerous particles, as shown in Figure 24.

For the counterflow flames, the appearance of the particles is similar. To extract the sample, the TEM grid was inserted perpendicular to the plane of the flame, at the centerline of the burner, into the center visible flame [104]. Figure 30 shows the electron micrograph of part of the sample grid which was inserted into a counterflow diffusion flame of methane and air with 300 mlll or $Fe(CO)_5$ added to the air stream. In general, the degree of agglomeration is much smaller than that in the premixed flame. Primary particle sizes range from 5 nm to 25 nm in diameter.

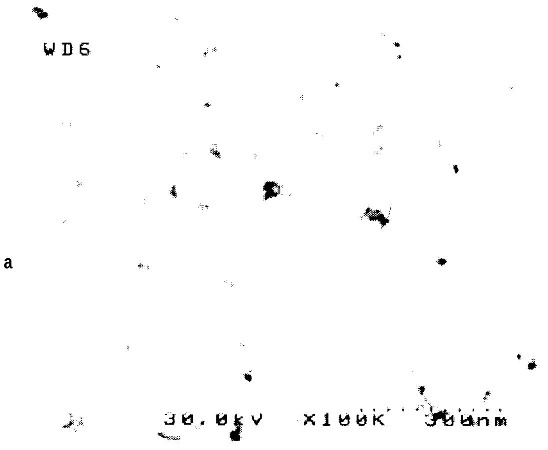

Figure 29 : Electron micrograph of particles sampled from a CH_4/air premixed flame with X_{inh} = 200 μL/L.

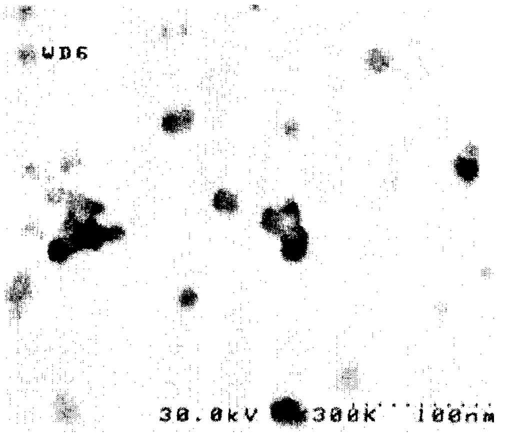

Figure 30 - Electron micrograph of particles sampled from counterflow dif-fusion flame at a = 1SO s^{-1} and X_{inh} = 300 μL/L (from ref. [104]).

3.5.4.1.3. Estimate of Upper Limit of Heterogeneous Inhibition

Although the evidence presented above supports a gas-phase inhibition mechanism of $Fe(CO)_5$, it is possible that heterogeneous chemistry also makes a contribution. The effects of walls on radical chain branching with regard to explosion limits are well documented [105], and heterogeneous iron and iron oxide catalysts are widely used in industrial processes. Further, iron oxide particles have recently been proposed as catalysts for NO_x reduction in stationary combustors [106]. With some assumptions, we can estimate the upper limit of radical recombination by collisions with particles, and determine the maximum effect of the particles on the burning velocity. To provide this upper limit, we assume: 1.) a two-step heterogeneous inhibition mechanism (Langmuir-Rideal type) in which a radical is absorbed onto a particle surface $R+P \rightarrow RP$, followed by the reaction of the activated particle RP with another radical and the release of the stable species $RP+R \rightarrow R_2+R$; 2.) all of the iron present condenses to particles; 3.) the particles are spherical with a specified mean diameter d_m, and log-normal size distribution; 4.) all collisions of radicals with particles lead to their recombination; 5.) only H-atom recombination is considered (the additional benefit of adding OH and O recombination is minor). The calculation is implemented using the PREMIX code and with the particles represented as fictitious species with the required rate parameters [37]. The results of the calculation are shown in Figure 31 for particles of diameter 10 nm to 80 nm. Also shown for comparison are

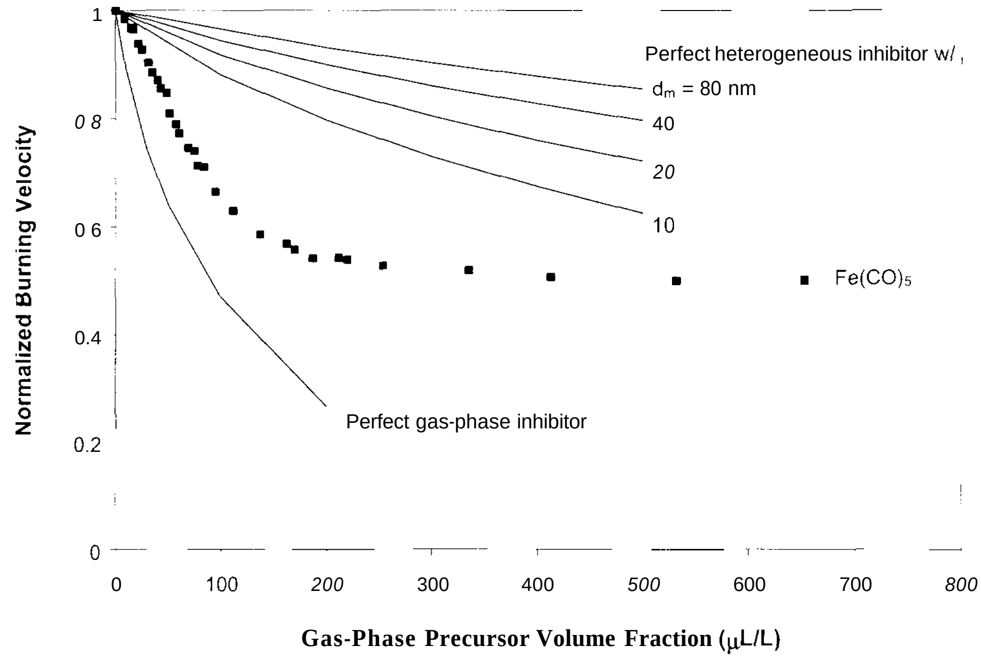

Figure 31 : Calculated normalized burning velocity for several diameters d_m of ideal heterogeneous inhibitor. Also shown are $Fe(CO)_5$ data [10], and calculated normalized burning velocity using the perfect gas-phase inhibitor mechanism [107] (source [37]).

experimental data (points) for $Fe(CO)_5$ inhibition of the premixed methane-air flames [10], and the results of a calculation for a proposed perfect gas-phase inhibitor [107] (bottom curve). In the perfect gas-phase mechanism, collisions of a chain-carrying radical with *any* gas-phase intermediate species of the inhibitor result in trapping of the radical. As the figure shows, the heterogeneous mechanism does show significant flame inhibition, which increases as the assumed particle diameter decreases. Nonetheless, the inhibition from the heterogeneous mechanism is not as strong as that shown by the experiment or by the perfect gas-phase inhibition mechanism.

The results of the calculations presented in Figure 31 support the importance of a homogeneous inhibition mechanism of iron rather a heterogeneous one. The formation of particles essentially increases the number of inhibitor molecules per particle, and increases the particle mean diameter d,,, . Since of the number of particles scales as $1/d_m^3$, but the collision cross section of particles with radical scales as $1/d_m^2$, the net effect of particle formation is to decrease the collision rate of radicals with inhibiting species. These idealized calculations support the proposals [10,107] that only gas-phase chemistry is fast enough to account for the extraordinary inhibition effect of $Fe(CO)_5$, since a more realistic model of heterogeneous radical recombination would probably result in less inhibition. It is interesting to note that the residual inhibition of $Fe(CO)_5$ at $X_{in} > 300$ µL/L in Figure 31, while small compared to values at $X_{in} < 100$ µL/L, is not zero. It is, in fact, comparable to agents such as CF_3Br and may be due to heterogeneous inhibition.

3.5.4.2. Counterflow Diffusion Flames

Laser scattering experiments to detect the presence of particles were also conducted in counterflow diffusion flames [104]. For these flames, the measurements were made along a vertical profile at the centerline of the fuel and oxidizer tubes. Figure 32 shows the scattering signal as a function of the distance from the center of the methane and air jets. The data points (connected by lines) correspond to values of $Fe(CO)_5$ volume fraction of (0, 50, 100, and 300) µL/L. The calculated gas temperature [83] as a function of distance from the center of the jets is shown by the top scale, and the calculated gas-flow stagnation plane is indicated by the vertical line. As the figure illustrates, the particles form in the low-temperature region on the air side of the flame, at temperatures below 500 K. Interestingly, as in the premixed flames, the particles are nearly completely consumed by the time they reach the location of the peak flame temperature (1961 K), and then re-form as they approach the stagnation plane. For this flow field, however, the residence time gets much longer as the particles approach the stagnation plane, allowing much time for particle growth. Further, as discussed below, thermophoretic forces cause the particles to cross the stagnation plane and reach an area of particle stagnation, which corresponds roughly to the location of the peak particle scattering signal, and occurs on the fuel side of the gas stagnation plane.

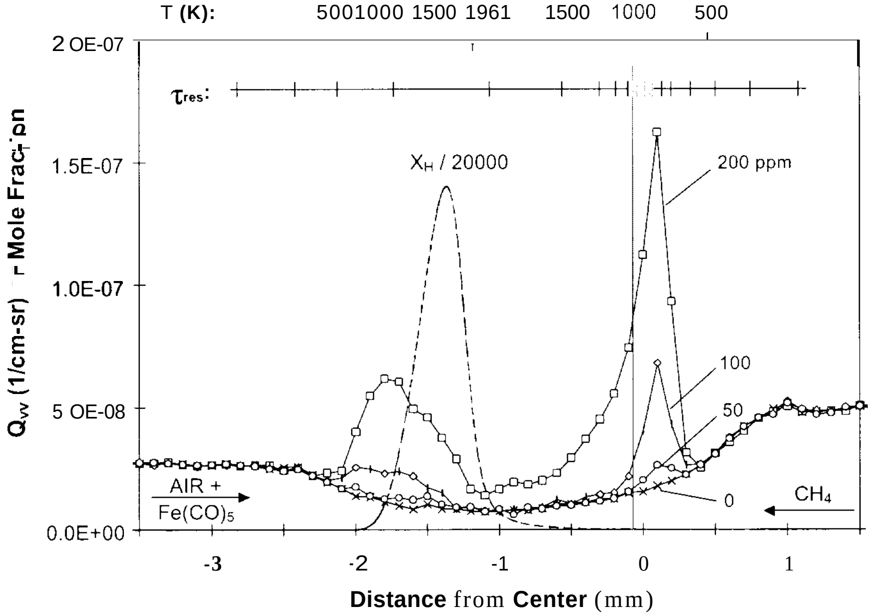

Figure 32 - Methane-air counterflow diffusion flame with inhibitor in the oxidizer. Shown are the calculated temperature (upper scale), stagnation plane location (vertical line), and H-atom mole fraction (dashed line) for the uninhibited flame, and the measured scattering profiles (connected points) for $Fe(CO)_5$ mole fractions of (0, 50, 100 and 200) μL/L in the air stream ($a = 330\ s^{-1}$,which is 50 % of a_{ext} for the uninhibited flame and 77 % of a,,, for X,,,= 200 μL/L). The estimated residence time for 5 nm particles is shown as 10 ms intervals in the hatched line near the top (from ref. [1041).

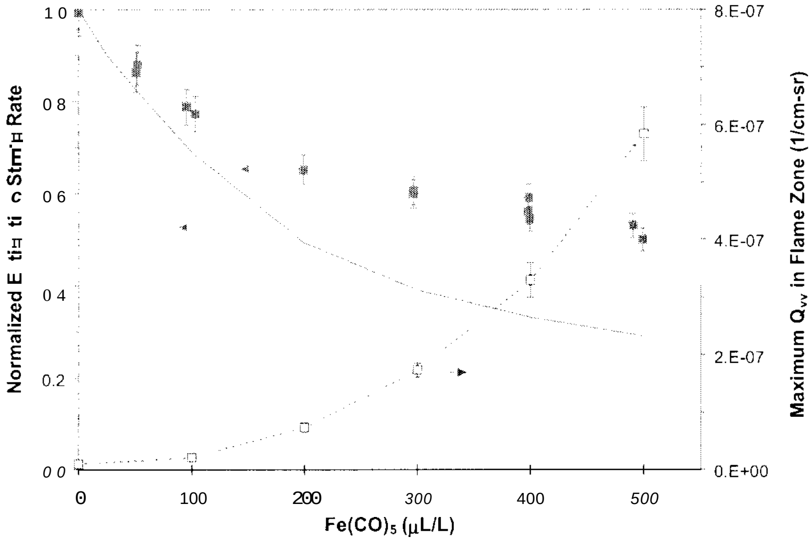

Figure 33: Correlation between inhibition effect and maximum Q_{vv} . Filled points are experimental normalized a,, , solid line is calculated a_{ext} ([83]). Open symbols connected by dotted lines are maximum measured Q_{vv}. Particle data collected at 75 % of a,,, (from ref. [1041).

Thermophoresis is important for the movement of small particles in these counterflow flames. Based on the gas-phase flame structure obtained from numerical calculations of uninhibited flames, we calculated the thermophoretic velocity of particles 5 nm in diameter [104]. Combining these with the gas-phase velocity, we determined the residence time of 5 nm particles injected from either the fuel or air jet. The hatched line near the top of Figure 32 shows the particle residence time (as 10 ms intervals between the hatch marks). Near the particle stagnation region, the near-zero particle velocities create large uncertainties in the estimated residence time (caused in part by the limited spatial resolution of the numerical flame structure calculation); this region is indicated by the shaded bar on the line showing the residence time. The inclusion of the thermophoretic velocity of the particles shows that 5 nm particles are expected to cross the stagnation plane about at the location of the fuel-side scattering peak, explaining its existence.

The formation of the particles on the *air* side of the gas stagnation plane is the likely cause of the loss of inhibition. With addition of $Fe(CO)_5$ to the air stream, the air-side scattering signal increases, even for values of X_{inh} as low as 50 µL/L. The dotted line in Figure 32 illustrates the calculated H-atom mole fraction in the uninhibited flame. The location of the peak particle scattering (about −1.75 mm) overlaps with the region of high H-atom mole fraction. Catalytic radical recombination cycles are most important in the regions where radical mole fractions are the highest (and iron species most strongly catalyze H-atom recombination). Hence, particles forming near the peak [H] can sequester the active gas-phase iron-containing intermediate species and thereby reduce the strength of the catalytic cycles.

The loss of effectiveness of $Fe(CO)_5$ in counterflow diffusion flames can be directly correlated with the formation of the air-side scattering peak from particles. Following the approach described above for premixed flames with $Fe(CO)_5$, the presence of particles is quantified by the height of the air side scattering peak (minus the scattering signal from the gas-phase species). Figure 33 shows the normalized extinction strain rate (left axis) as a function of the $Fe(CO)_5$ volume fraction in the air stream. As in the premixed flames, the inhibitor is very effective at low values of X_{inh}, but loses its effectiveness sharply as X_{inh} reaches a certain value (about 150 µL/L for these conditions). Similarly, the normalized extinction strain rate calculated using a gas-phase only kinetic mechanism [48] (solid line in Figure 33) follows the experimental data reasonably closely for X_{inh}<100 µL/L, but starts to deviate as X_{inh} increases. The measured scattering cross section (right axis; open squares connected by dotted lines) shows that the scattering signal increases noticeably when the $Fe(CO)_5$ reaches the point of lower marginal effectiveness (~ 150 µL/L). As in the premixed flames, the *loss* of effectiveness of the $Fe(CO)_5$ is correlated with particle formation, rather than the converse.

Particle formation followed by flow-field effects can also *prevent* metallic inhibitors from entering into gas-phase catalytic radical scavenging reactions. To illustrate this, Figure 34 shows the scattering cross section from a counterflow methane-air diffusion flame with $Fe(CO)_5$ added to the *fuel* side of the stagnation plane at various values of X_{inh}. The calculated temperature field, residence time estimate, and location of peak [H] are the same as in Figure 33 for air-aide agent addition. In the case of fuel-side $Fe(CO)_5$ addition shown in Figure 34, the iron-containing species also start to condense at local gas temperatures less then 500 K. In this case, however,

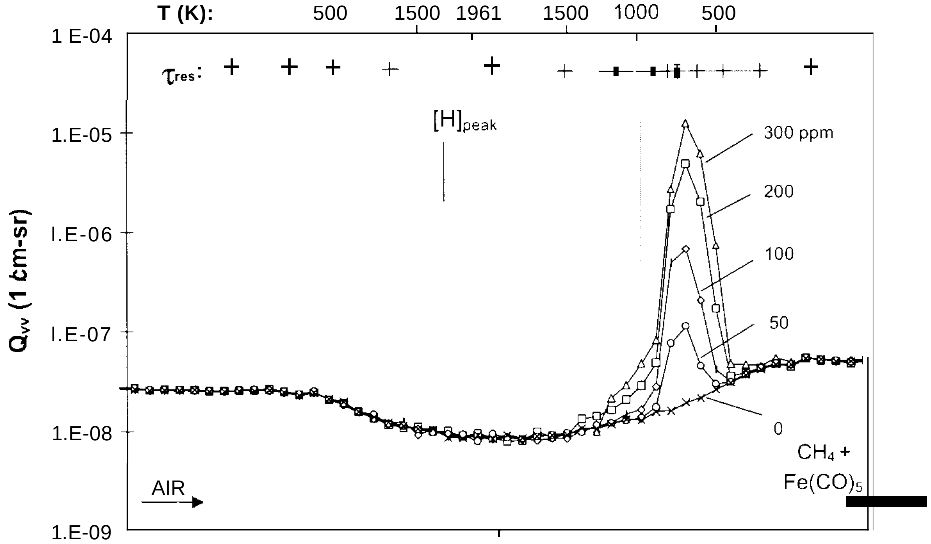

Figure 34: Measured scattering profiles in CH_4-air counterflow diffusion flame with inhibitor in the fuel. The calculated temperature and point of peak H-atom mole fraction are marked on the upper x-axis, and the vertical line denotes the calculated location of the stagnation plane. Strain rate = 330 s^{-1} (from ref. [104]).

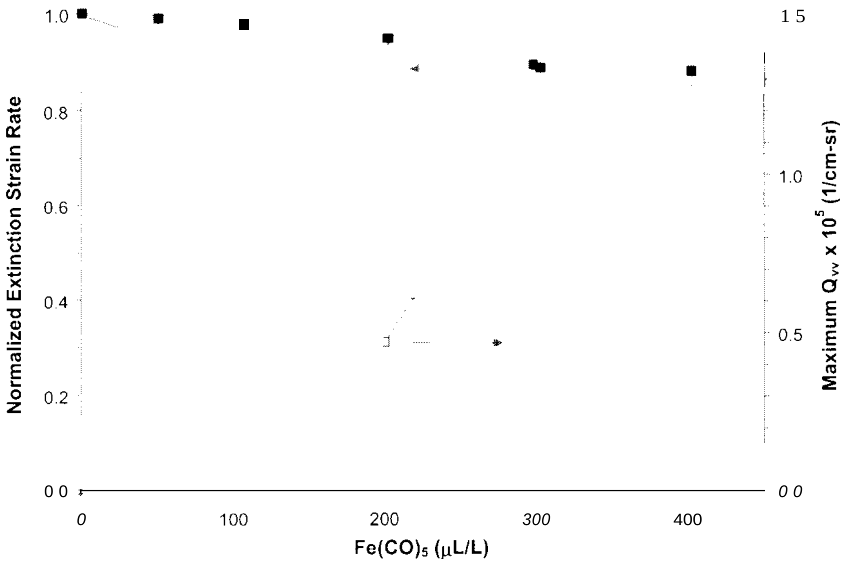

Figure 35 – Effect of $Fe(CO)_5$ added to the fuel stream of a methane-air counterflow diffusion flame. The experimentally measured and numerically calculated normalized extinction strain rate [83] are shown (left axis) as a function of $Fe(CO)_5$ volume fraction in the fuel stream. The maximum scattering cross section (right axis). obtained from the results in Figure 34 is also shown for increasing X_{inh}.

the thermophoretic forces *prevent* the iron from crossing the stagnation plane, and the scattering signal reaches its peak value near the calculated particle stagnation region for 5 nm particles. The scattering signal at the particle stagnation plane is two orders of magnitude larger for fuel-side agent addition than for air-side addition. Thus, fuel-side agent addition leads to particle formation, which together with thermophoretic and flow-field effects, effectively prevents the active species from reaching the location of peak [H]. For the methane-air flames of Figure 34, however, the $Fe(CO)_5$ added to the fuel stream would not be expected to inhibit the flame, even if the particles did not form. This is illustrated in Figure 35, which shows the reduction in the normalized extinction strain rate (left axis) with added $Fe(CO)_5$ to the fuel stream. For both the experimental data and the numerical predictions (based on a gas-phase only model), the inhibition of the flame is minimal. The increase in the scattering signal (right axis) with added $Fe(CO)_5$, however, is very large. As discussed previously [83], the $Fe(CO)_5$ added to the fuel stream is ineffective even if it remains in the gas phase; to be effective, the inhibiting species (or their precursors) must diffuse upstream into the oxidizer stream and reach the location of significant H-atom mole fraction. For these flames, however, the convective flow is larger than the diffusive flow, so the inhibitor (or its fragments) can't get to where it is required for radical recombination.

The importance of particle convection can be more clearly illustrated by considering a counterflow diffusion flame with the peak temperature and [H] closer to the stagnation plane, where gas-phase inhibiting species could diffuse. Such a flame is obtained from an oxidizer with volume fractions of 30 % O_2 / 70 % N_2 , and a fuel of 80 % CH_4 / 20 % N_2. The results of particle measurements for $Fe(CO)_5$ added to the air stream of such a flame is shown in Figure 36. For this flame, both the peak temperature and [H] are slightly on the fuel side of the gas stagnation plane (vertical line), while the particle stagnation plane (shaded box on the residence time bar at the top) is slightly on the oxidizer side. Clearly, very large particle scattering signals are present, and as in Figure 34 above, the particles do not appear to have significantly crossed the gas stagnation plane, and hence cannot deliver the active species to the region of high [H]. Unlike in Figure 34, however, the gas-phase inhibiting species *can* diffuse to the region of high [H]. This is illustrated in Figure 37, which shows the experimental measured and numerically calculated reduction in the normalized extinction strain and the particle scattering cross section for increasing amounts of $Fe(CO)_5$ in the air stream. Based on the experiments, adding $Fe(CO)_5$ has little effect on this flame. The calculations, however, which are based on a gas-phase model, predict that the added $Fe(CO)_5$ should have a significant effect (implying that the gas-phase species *can* diffuse to the location of the peak [H] (shown in Figure 36). Nonetheless, the scattering measurements show prominent particle formation. Since, in Figure 36, both the gas stagnation plane (vertical line) and the particle stagnation region (shaded box on residence time bar at top) separate the particles from the region of peak [H], the particles can effectively isolate the active intermediate species from the location of H-atom where they are required to inhibit the flame. Consequently, we see in Figure 37 that while the gas-phase model (solid line) implies that inhibition should occur with addition of $Fe(CO)_5$, the experiments (points) do not show inhibition, and this is consistent with the large scattering signal (dotted line) observed with addition of the $Fe(CO)_5$.

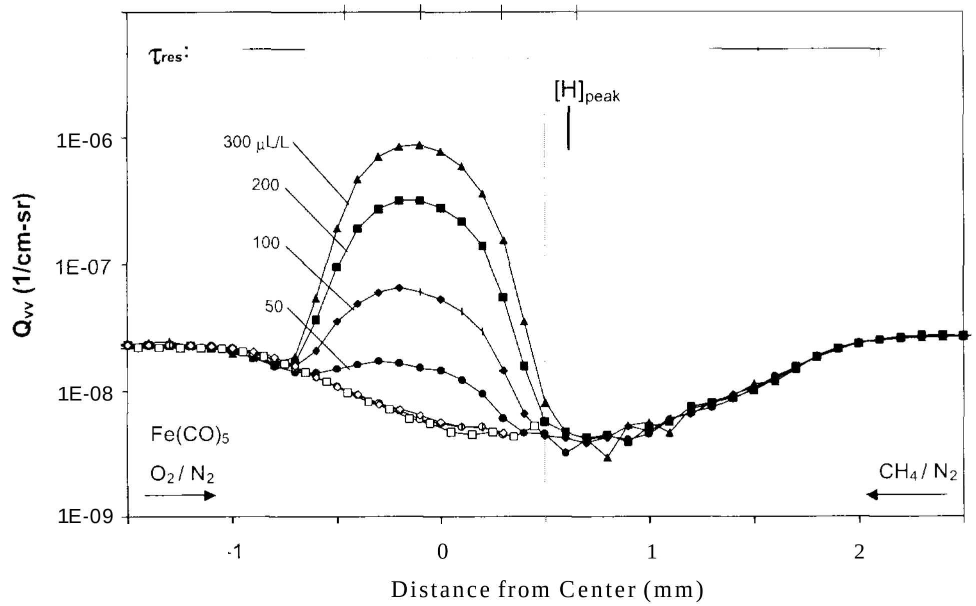

Figure 36 - Scattering profiles through a counterflow diffusion flame of 30 % O_2/70 % N_2 and 80 % CH_4/N_2. The calculated temperature and point of peak H-atom mole fraction are marked on the upper x-axis, and the vertical line denotes the calculated location of the stagnation plane. $Fe(CO)_5$ is added to the oxidizer stream at the indicate volume fraction. The estimated residence time for 5 nm particles is shown as **10** ms intervals in the hatched line near the top (from ref. [104]).

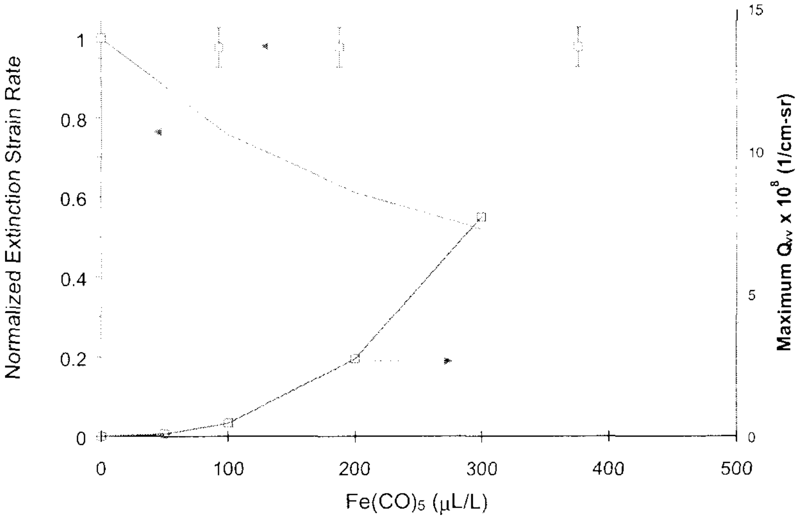

Figure 37 - Effect of $Fe(CO)_5$ added to the air stream of a diluted methane-air counterflow diffusion flame. The experimentally measured (points) and numerically calculated (solid line) normalized extinction strain rate [83] are shown (left axis) as a function of $Fe(CO)_5$ volume fraction in the air stream. The maximum scattering cross section (right axis), obtained from the results in Figure **34** is also shown for increasing X_{inh}.

The results presented for the counterflow diffusion flames with added Fe(CO)$_5$ illustrate the following *physical* phenomena which can influence the efficiency of the inhibitor. 1.) The rate of gas-phase transport of the active inhibiting species to the location of peak [H], either by diffusion or convection; 2.) Particle formation, which can reduce the availability of active gas-phase species either by: a.) reducing the gas-phase mole fraction of the active iron-containing intermediate species in the vicinity of the peak [H], or b). physically separating the particles from the region of peak [H] by flow field and thermophoretic effects. This background information is essential for understanding the relevant phenomena affecting the action of metallic inhibitors when added to the more complex flow field of the cup-burner flames, as described below.

3.5.4.3. Cup-Burner Flames

As described above, for inhibiting cup-burner flames, the organometallic agents TMT, MMT, and Fe(CO)$_5$ were found to be far less efficient than they were in either premixed or diffusion flames. Figure 38 shows the volume fraction of CO_2 required to blow off a cup-burner flame as a function of the mole fraction of added catalytic inhibitor in the air stream [14]. Data are presented for CF_3Br, Br_2, TMT, Fe(CO)$_5$, and MMT, as well as for a blend of TMT, MMT, and Fe(CO)$_5$. The inset of Figure 38 shows the region of interest (low inhibitor volume fraction) with expanded scales. The agents CF_3Br and Br_2 are shown to effectively reduce the amount of

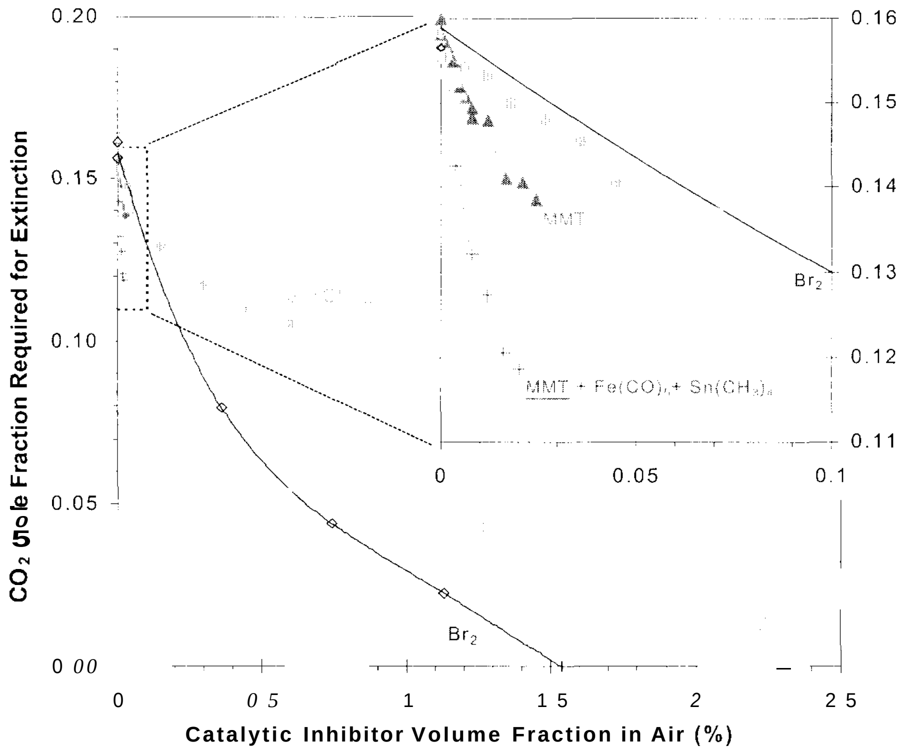

Figure 38 – Volume fraction of CO_2 required for extinction of methane-air cup burner tlames as a function of the volume fraction of catalytic inhibitor added to the air stream. Inset shows region in dotted box with expanded scales

CO_2 required to extinguish the flame. The metallic agents reduce the amount of required CO_2 somewhat more effectively than does CF_3Br, but they lose their effectiveness in a manner that is similar to that described above for premixed and diffusion flames. In the cup-burner flames, TMT, MMT, and $Fe(CO)_5$ were approximately 3, 8, and 4 times as effective as CF_3Br, in contrast to premixed flames, in which they were 3, 40, and 80 times as effective. The net result is that the metallic agents were not particularly effective in cup-burner flames. This result was surprising, and further work was conducted to understand the loss of effectiveness.

Particle formation is likely the cause of the degraded performance of the metal agents in cup-burner flames. Evidence to support this is that the approximate agent volume fraction for the loss of effectiveness is an order of magnitude higher for TMT (4000 µL/L) than for the iron or manganese (400 µL/L) (as occurs in premixed flames) [12], which is consistent with the higher vapor pressure for the tin compounds. Also, the manner in which Fe-, Sn- and Mn-containing compounds lose their effectiveness in premixed flames [12] is comparable to that indicated in Figure 38 (inset). Finally a visible outer annulus, apparently particles, was observed in all flames with added metals, and the blackbody radiation from that region increased with higher agent volume fraction.

To more accurately detect the particles, we conducted laser-scattering experiments in the cup-burner flames with and without added $Fe(CO)_5$. The scattering measurements were made on several horizontal paths across the flame at fixed heights above the fuel-cup rim. Although methane-air cup burner flames are unsteady, flickering at about 10 Hz with a large amplitude, steady, nearly non-flickering flames are achieved with addition of CO_2 to the air stream. Hence, scattering measurements in cup-burner flames with $Fe(CO)_5$ added to the air stream were performed with a CO_2 volume fraction of 8 % in the air stream. This approach was reasonable since the extinction tests were also conducted with appreciable volume fractions of CO_2. The agent $Fe(CO)_5$ was added to the air stream at (0, 100, 200, 325, and 450) µL/L. Figure 39 to Figure 42 present radial profiles of the scattering cross section (arbitrary but consistent units) at heights above the burner rim of (3, 6, 10, 15, and 20) mm. Also shown in each figure is the location of the peak visible emission, obtained from a digitized video image of the flame with 0 µL/L of $Fe(CO)_5$. Since the oxygen demand of the $Fe(CO)_5$ in the oxidizer stream at 450 µL/L is about 0.6 % that of the methane, the flame location should not be significantly modified by presence of this fuel-like agent in the co-flow [108]. In Figure 39 to Figure 42, the peak scattering signal detected is (1.1, 4.7, 12.7, and 25.5) x 10^{-6} 1/(cm-sr), respectively, which are 50, 209, 559, and 1166 times the scattering signal for air at laboratory conditions. In all cases, the presence of particles is clearly indicated, and the magnitude of the scattering signal increases with $Fe(CO)_5$ volume fraction in the air. For each value of X_{inh} , the relative distribution of the particles for each height and radial position is approximately conserved. Particles are present both inside and outside, but not coincident with, the visible flame location. Flames without $Fe(CO)_5$ (not shown) had scattering cross sections attributable to only the hot and cold product and reactant gases.

Figure 39 to Figure 42 – Scattering cross section for laser light at 488 nm as a function of radial position and height above burner in methane-air cup-burner flame with 8 % CO_2 and $Fe(CO)_5$ in air at specified volume fraction . Dotted lines show flame location from a digitized video image of the uninhibited flame.

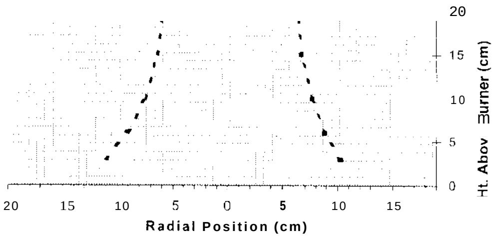

Figure 39 - $Fe(CO)_5$ in air at 100 μL/L.

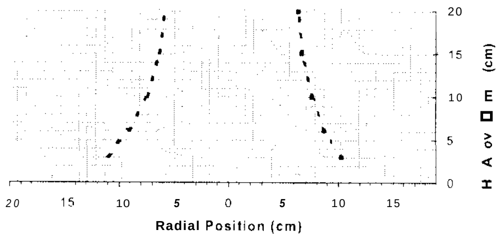

Figure 40 – $Fe(CO)_5$ in air at 200 μL/L.

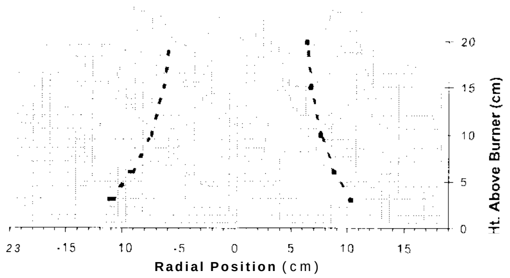

Figure 41 – $Fe(CO)_5$ in air at 325 μL/L.

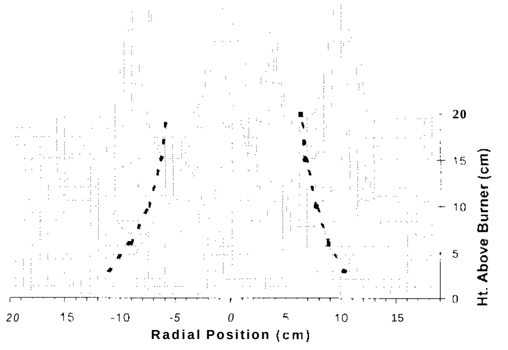

Figure 42 – $Fe(CO)_5$ in air at 450 μL/L.

In order to interpret the scattering results shown in Figure 3, it is useful to consider the particle measurements in the premixed [37] and counterflow diffusion flames [104] seeded with $Fe(CO)_5$. From the above results, it appears that: 1.) the iron-containing species start to condense as the temperature increases to about 500 K , which is hot enough to breakdown the iron precursor [48], but not too hot to vaporize the iron compound; 2.) the particles are small, –10 nm to 20 nm; 3.) thermophoresis moves the particles away from the peak temperature; 4.) drag forces tend to entrain the particles along the gas flow streamlines; *5).* particles can re-vaporize as they enter regions of high temperature; 6.) longer residence times lead to a greater scattering signal (and presumably, a greater fraction of condensed species); and 7.) more $Fe(CO)_5$ leads to a larger scattering signal. In order for the iron species to have a chemical effect on the flame, they must: 1.) reach the region of peak [H] as gas-phase species; 2.) be active in a region which affects the flame stability (and hence, the blow-off condition).

Since the present cup-burner flames have quite different flow fields than either premixed or counterflow diffusion flames, it is likely that the particle formation and behavior in them is different. For example, iron added to the air stream of either the premixed or counterflow diffusion flame eventually must pass through the flame by convection. In contrast, convection is comparatively less important in co-flow diffusion flames. Further, thermophoretic forces can have a strong influence on particle trajectories in flames [109]. Recent attempts to seed co-flow diffusion flames with $TiCl_4$ to provide very small TiO_2 for laser imaging of the velocity field proved ineffective due to strong thermophoresis of the particles [110]. For the present co-flow diffusion flames, the thermophoretic forces are nearly tangent to the flow streamlines, so their relative importance will be greater. Also, as discussed by Faeth et al. [1 11], the flow streamlines tend to enter the flame near the burner jet exit, and then remain approximately parallel to the temperature contours before again crossing the flame near the tip. Hence, iron could enter the center region from convection into the flame near the base (providing the iron inside the flame sheet for particle formation). Thermophoresis could then push the particles away from the flame sheet, resulting in the particle distribution shown in Figure 39 to Figure 42. Alternatively, the particles may still be present in the region of peak [H], but may be too small to be detected at the lock-in sensitivity used to resolve the larger scattering signals.

It is possible to plot the flame inhibition strength as a function of added $Fe(CO)_5$ for comparison with the particle scattering signal. Figure 43 shows such a plot, which can be compared to Figure 26, Figure 33, and Figure 37 for premixed and counterflow diffusion flames (with pure and diluted gases). The added iron has little effect on the amount of CO_2 required for extinction, yet the peak particle scattering signal clearly increases with added iron. What is missing from Figure 43 is a model prediction to show that for gas-phase inhibiting species, a reduction in CO_2 for flame extinction is expected. While such calculations are desired (but as yet unavailable for the cup burner), we can still infer the active role of gas-phase species from the data available. For example, both CF_3Br and Br_2 added to the air stream were very effective at reducing the CO_2 for extinction. Hence, catalytically acting gas-phase agents which don't condense do reduce the amount of CO_2 required for extinction.

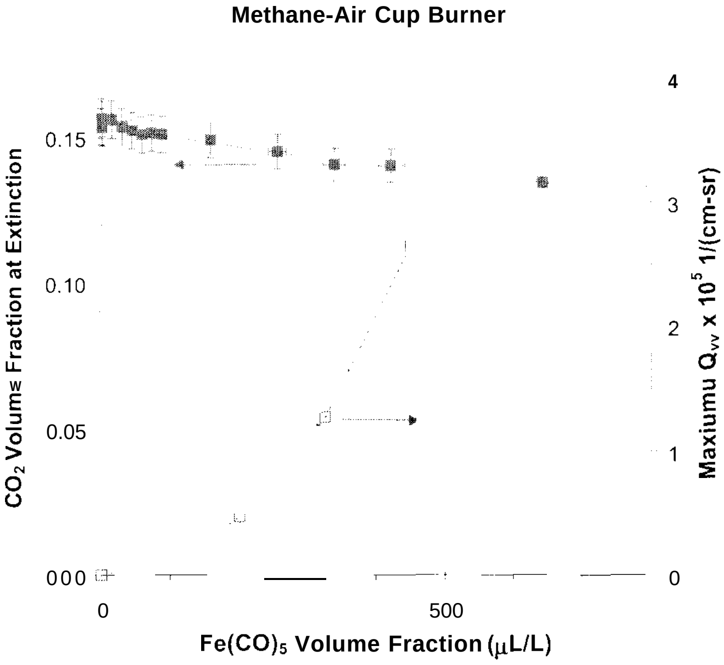

Figure 43 – Extinction volume fraction of CO_2 (left axis) [14] and peak measured scattering cross section (right axis), as a function of the volume fraction of $Fe(CO)_5$ in the air stream.

From the ineffectiveness of iron when added to the cup burner (as shown in Figure 38), it seems that the iron species of the catalytic cycle are not reaching the regions of the flame in which they are need to cause flame destabilization and blow-off. Examination of Figure 39 to Figure 42 shows that the iron particles are not coincident with the visible flame location. One might infer that this means that 1.) the iron is sequestered in the particles, and 2.) the particles are kept away from the high-temperature regions near the peak [H] by thermophoresis, and 3.) these lead to a low value of the gas-phase mole fraction of the iron–containing intermediate species near the peak [H]. While these features are probably true in the flame, it is not possible to extract this understanding from the data available.

At the present time, the location of the stabilization region of the cup burner flame most sensitive to chemical inhibition is not known, nor are the H-atom concentration profiles or the flow streamlines. These data would provide a much clearer explanation of the effects of particles on iron inhibition of cup-burner flames.

3.5.5. *Conclusions*

Large scattering signals from cup-burner flames with $Fe(CO)_5$ added to the air stream indicated that particles are present both inside and outside of the flame, but not co-incident with the visible flame location.

A review of the results from previous work with particle formation in premixed and countertlow diffusion flames inhibited by $Fe(CO)_5$ outlined the importance of the following physical effects with respect to effective chemical inhibition:

1.) gas-phase transport of the active iron-containing species to the region of high H-atom concentration is necessary for efficient inhibition.
2.) Particle formation near the location of peak [H] can act as a sink for the iron-containing intermediate species and reduce the catalytic effect.
3.) The mole fraction of inhibitor influences condensation since at low values, it may be below its saturation value.
4.) The available residence time affects particle growth.
5.) Thermophoretic forces can be large in the flame and re-distribute particles away from peak [H].
6.) Convection and drag forces combined with the existing flow field in the flame can prevent particles from reaching the region of peak [H].

Using this information we can infer that particles start to form in the cup-burner flames in regions where $Fe(CO)_5$ is transported and when the temperature has risen slightly (to allow decomposition of the precursor molecule $Fe(CO)_5$). These particles act as sinks for the active species, reducing their overall catalytic ability. Therinophoretic forces (which are tangent to the flow streamlines) move the particles away from the region of peak temperature and [H].

Nonetheless, the actual regions in a cup-burner flame which are most sensitive to chemical inhibition are not known for *any* catalytic agent. The work illuminates the need for detailed measurements and numerical modeling (with full chemistry) of cup-burner flames so that the actions of chemical inhibitors in such flames can be more clearly discerned.

4. Technical Problems

This project uncovered three major technical problems. The first is that the relative effectiveness of any suppressant agent which involves particles (either formed during the suppression process, or as the form of the added agent) depends upon the type of flame used to assess its performance. The second is that it is not known which type of tractable laboratory flame most clearly represents the conditions of an actual fire. Indeed, most likely, different burners will be necessary to understand different fire threats. This raised the important point (not addressed in the present work) that the flame structure in actual fires to be suppressed have not been measured or modeled. Finally, even for the simple cup burner, the detailed flame structure is not known, so it is not currently possible to understand in detail why metallic agents, at non-condensing mole fractions were less effective than expected. That is, for any agent, including CF_3Br, it is not known where the agent must act in order to effectively extinguish or blow off the flame. Hence, until this deficiency is remedied, it is unlikely that such information will be available for more complicated flames as occur in fires.

5. Recommendations

While good progress has been made in understanding chemical inhibition and suppression of laboratory flames, the technical problems described above should be addressed in order to understand the potential and limitations of chemical inhibitors for suppressing actual fires. We recommend that the conditions which exist in fire to be suppressed be measured and modeled. This is useful both for understanding the mechanism of chemical inhibitors in large fires, but also for determining the optimum size of condensed-phase suppressants (such as water mist or sodium bicarbonate). Next, the laboratory flame types should be identified which most closely describe the conditions in the actual suppressed fires. Finally, experiments and modeling should be conducted to understand the flame structure of inhibited and suppressed flames in the burner type which is most closely related to the actual fire threats. This burner type may well be a low-strain diffusion flame such as the cup burner. Since this is a standard device used to assess suppressant effectiveness, we recommend experiments and numerical modeling to more fully understand the regions of the cup burner flame most susceptible chemical inhibition, and how the properties of various chemical and inert agents act to cause blow-off or extinction. Cup burners represent flames which may be more representative of some fires, but still of a scale and simplicity for which detailed numerical modeling is now possible. Those tests and calculations should precede those for larger scale fires—which are still beyond current experimental and numerical capabilities.

6. Conclusions

Manganese and tin are more effective flame inhibitors than bromine, but less effective than iron. However, all of the organometallic agents are essentially ineffective in cup-burner flames. and it is likely that they will also be ineffective in suppressing actual fires. The loss of effectiveness is likely caused by condensation to particles, followed by flow field and thermophoretic effects which sequester the particles from the regions of high radical mole fraction in the flame, where they are likely needed to cause flame extinction. Metal salts added to droplets can reduce the quantity of water needed to extinguish laboratory flames. The efficiency of droplets, however also depends upon their size. It is likely that any metal containing agent will experience the same loss of effectiveness in the cup burner since it is the active intermediate species (not the agent itself) which are believed to be condensing.

An additional conclusion of this work is that the performance of any inhibitor which involves a condensed phase (either as the form of the added agent, or from condensation of intermediate or product species of the inhibitor) will depend upon the interaction of the flow and temperature field of the fire with the particles. Hence, the performance of the such agents can vary widely with the type of laboratory flame or fire in which it is used.

Acknowledgements: *Helpful conversatoins with Wing Tsang, Kermit Smyth, Fumi Takahashi, Dick Gann, George Mulholland, and Bill Grosshandler are gratefully acknowledged. This research is part of the Department of Defense's Next Generution Fire Suppression Technology Program, funded by the DoD Strategic Environmental Research and Development Program under contract number W74RDV83528667. Internal NIST funding is also gratefully acknowledged. The author thanks Taniu Ritchie for conducting the extinction experiments. This research was supported by DOD SERDP's Next Generation Fire Siippression Technology Program, and by NASA's Office of Biological and Physical Research.*

7. References

[1]. Linteris, G. T. and Chelliah, H. K. *Powder-Matrix Systems for Safer Handling arid Storage of Suppression Agents,* National Institute of Standards and Technology, NISTIR 6766, 2001.

[2]. Andersen, S.O., *Fire Journal* 81:56-& (1987).

[3]. Grosshandler, W. L., Gann, R. G., and Pitts, W. M., *Evaluation of Alternative In-Flight Fire Suppressants for Full-scale Testing in Simulated Aircraft Engine Nacelles and Dry Bays,* NIST SP 861, 1994.

[4]. Gann, R. G., *Fire Suppression System Performance of Alternative Agents in Aircraft Engines and Dry Bay Laboratory Simulations,* NIST SP 890, vols. I and II, 1995.

[5]. Miziolek, A. W. and Tsang, W., *Halon Replacements,* Acs Symposium Series 611, American Chemical Society, Washington, D.C., 1995.

[6]. MacDonald, M.A., Jayaweera, T.M., Fisher, E.M., and Gouldin, F.C., *Proceedings of the Combustion Institute, Vol. 27,* The Combustion Institute, Pittsburgh, 1998, pp.

[7]. Babushok, V. and Tsang, W., *International Conference on Fire Research and Engineering, Third,* Society of Fire Protection Engineers, Boston, MA, 1999, pp. 257-267.

[8]. Macdonald, M.A., Jayaweera, T.M., Fisher, E.M., and Gouldin, F.C., *Combust. Flame* 116:166 (1999).

[9]. Macdonald, M.A., Gouldin, F.C., and Fisher, E.M., *Combust. Flame* 124:668 (2001).

[10]. Reinelt, D. and Linteris, G.T., *Proc Combust. Inst.* 26:1421 (1996).

[11]. Linteris, G.T., Rumminger, M.D., Babushok, V., and Tsang, W., *Proc. Combust. Inst.* 28:2965 *(2000).*

[12]. Linteris, G.T., Knyazev, K., and Babushok, V., *Combust. Flame* accepted (2001).

[13]. Fallis, S., Holland, G.F., McCormick, J.L., Reed, R., and Wilson, K.A. *Halon Options Technical Working Conference,* Albuquerque, NM, 2001, pp. pp. 364-372.

[14]. Linteris, G.T.. *Proc. Combust. Inst.* 29:submitted *(2002).*

[15]. Chelliah, H.K., Lazzarini, A.K., Wanigarathne, P.C., and Linteris, G.T., *Proc. Combust. Inst.* 29:submitted *(2002).*

[16]. Linteris, G.T. and Rumminger, M.D., *Western States Section Meeting, The Combustion Institute,* La Jolla, CA,

[17]. Bulewicz, E.M. and Padley, P.J., *Proc. Combust. Inst.* 13:73 (1971).

[18]. Bulewicz, E.M. and Padley, P.J., *Chem. Phys. Lett.* 9:467 (1971).

[19]. Hastie, J. W., *High Temperature Vapors,* Academic Press, New York, 1975.

[20]. Jensen, D.E. and Webb, B.C., *AIAA J.* 14:947 (1976).

[21]. Howard, J.B. and Kausch, W.J., *Prog. Energy Combust. Sci.* 6:263 (1980).

[22]. Cusack. P.A. and Killmeyer, A.J., ACS *Symp. Ser.* 425:189 (1990).

[23]. Hornsby, P.R., Mitchell, P.A., and Cusack, P.A., *Polym. Degrad. Stab.* 32:299 (1991).

[24]. Lask, G. and Wagner, H.G., *Proc. Combust. Inst* 8:432 (1962).

[25]. Miller, D.R., Evers, R.L., and Skinner, G.B., *Combust. Flame* 7:137 (1963).

[26]. Miller, D.R., *Combust. Flame* 13:210 (1969).

[27]. Morrison, M.E. and Scheller, K., *Combust. Flame* 18:3 (1972).

[28]. Pitts, W. M., Nyden, M. R., Gann, R. G., Mallard. W. G., and Tsang, W., *Construction of an Exploratory List of Chemicals to Initiate the Search for Halon Alternatives,* National Institute of Standards and Technology, NIST Technical Note 1279, 1990.

[29]. Vanpee, M. and Shirodkar, P., *Proc. Combust. Inst.* 17:787 (1979).

[30]. Westblom, U., Fernandezalonso, F., Mahon, C.R., Smith, G.P., Jeffries, J.B., and Crosley, D.R., *Combust. Flame* 99:261 (1994).

[31]. *Manganese Containing Antinock Compounds (Nesnieyanov, A.N., Ed.)*, Nauka, Moskow, 1971.

[32]. Tapscott, R. E., Heinonen, E. W., and Brabson, G. D., *Advanced Agent Identification and preliminary Assessment*, NMERI, University of New Mexico, NMERI 95/38/32350, 1996.

[33]. Chao, B.H., Egolfopoulos, F.N., and Law, C.K., *Combust. Flame* 109:620 (1997).

[34]. Andrews, G.E. and Bradley, D., *Combust. Flame* 18:133 (1972).

[35]. Linteris, G.T. and Truett, L., *Conibust. Flame* 105:15 (1996).

[36]. Rumminger, M.D. and Linteris, G.T., *Combust. Flame* 120:451 *(2000).*

[37]. Rumminger, M.D. and Linteris, G.T., *Combust. Flame* 123:82 *(2000).*

[38]. Rumminger, M.D., Reinelt, D., Babushok, V., and Linteris, G.T., *Halon Options Technical Working Conference*, Albuquerque, NM, 1998, pp. 145-156.

[39]. Gilbert, A.G. and Sulzmann, K.G.P., *J. Electrochem. Soc.* 121:832 (1974).

[40]. Stull, D.R., *Ind. Eng. Chem.* 39:517 (1947).

[41]. Hollrah, D., "Ethyl Corp., Personal Communication, Jan. 2001.

[42]. Bulewicz, E.M. and Padley, P.J., *Trans. Faraday Soc.* 67:2337 (1971).

[43]. Goodings, J.M. and Chen. Q.-F., *Can. J. Chem.* 76:1437 (1998).

[44]. Taylor, J.E. and Milazzo, T.S., *J. Phys. Chem.* 82:847 (1978).

[45]. Gurvich, L. V., Karachevtsev, G. V., Kondratiev, V. N., Lebedev, Yu. A., Medvedev, V. A., Potapov, V. K., and Hodeev, Ya. S., *Bond Energies. Ionization Potentials and Electron Affinities* , Nauka, Moskow, 1974.

[46]. Smith, G.P., "Personal Communication, 1999.

[47]. Hildenbrand. D.L. and Lau, K.H., *J. Cheni. Phys.* 100:8377 (1994).

[48]. Rumminger, M.D., Reinelt, D., Babushok, V., and Linteris, G.T., *Combust. Flame* 116:207 (1999).

[49]. Fontijn, A. and Bajaj, P.N., *J. Phys. Cheni.* 100:7085 (1996).

[50]. Husain, D., Plane, J.M., and Xiang, C.C., *J. Chem. Soc., Faraday Trans. 2* 80:1465 (1984).

[51]. Gurvich, L. V., Iorish, V. S., Chekhovskoi, D. V., Ivanisov, A. D., Proskurnev, A. Yu., Yungman, V. S., Medvedev, V. A., Veits, I. V., and Bergman, G. A., *IVTHANTHERMO - Database on Thermodynamic Properties of Individual Substances,* Institute of High Temperatures, Moscow, 1993.

[52]. J.A. Martinho Simões , in *NIST Chemistry WebBook, NIST Standard Reference Database Number 69* (Mallard, W. G. and Linstrom, P. J., Ed.), National Institute of Standards and Technology, Gaithersburg, MD 20899 (`http://webbook.nist.gov`), 2000.

[53]. Lippincott, E.S. and Tobin, M.C.J., *J. Am. Chem. Soc.* 75:4141 (1953).

[54]. Jensen, D.E., *J. Chem. Soc., Faraday Trans.* 76:1494 (1980).

[55]. Babushok, V. and Tsang, W., *Joint Meeting of the United States Sections of the Conibustion Institute.* The Combustion Institute, Pittsburgh, PA, 1999, pp. 587-590.

[56]. Kee, R. J., Grcar, J. F., Smooke, M. D., and Miller, J. A., *A Fortran Computer Program for Modeling Steady Laminar One-dimensional Premixed Flames,* Sandia National Laboratories Report. SAND85-8240, 1991.

[57]. Kee, R. J., Rupley, F. M., and Miller, J. A., *CHEMKIN-II: A Fortran Chemical Kinetics Package for the Analysis of Gas Phase Chemical Kinetics,* Sandia National Laboratory, SAND89-8009B, 1989.

[58]. Kee, R. J., Dixon-Lewis, G., Warnatz, J., Coltrin, R. E., and Miller, J. A., A *Fortran Coniputer Package for the Evaluation of Gas-Phase, Multicomponent Transport Properties,*

Sandia National Laboratory, SAND86-8246, 1986.

[59]. Smith, G. P., Golden, D. M., Frenklach, M., Moriarty, N. W., Eiteneer, B., Goldenberg, M., Bowman, C. T., Hanson, R. K., Song, S., Gardiner, Jr. W. C., Lissianski, V. V., and Qin. Z., http://www.nie.berkeley.edu/gri_mech, 2000.

[60]. Linteris, G.T., in *Halon Replacements* (Miziolek, A. W. and Tsang, w., Ed.), Acs Symposium Series 611, American Chemical Society, Washington, D.C.. 1995.

[61]. Noto, T., Babushok, V., Hamins, A., and Tsang, W., *Combust. Flame* 112:147 (1998).

[62]. Linteris, G.T., Rumminger, M.D., and Babushok, V.I., *Combust. Flame* 122:58 (2000).

[63]. Grant, G., Brenton, J., and Drysdale, D., *Prog. Energy Combust. Sci.* 26:79 (2000).

[64]. Zegers, E.J.P., Williams, B.A., Sheinson, R.S., and Fleming. J.W., *Proc. Combust. Inst.* 28:2931 (2000).

[65]. Lentati, A.M. and Chelliah, H.K., *Proc. Combust. Inst.* 27:2839 (1998).

[66]. Prasad, K., Li, C., Kailasanath, K., Ndubizu, C., Ananth, R., and Tatem, P.A., *Combust. Sci. Technol.* 132:325 (1998).

[67]. Zheng, R.. Bray, K.N.C., and Rogg, B., *Combust. Sci. Technol.* 126:389 (1997).

[68]. Mitani, T. and Niioka, T., *Combust. Flame* 55:13 (1984).

[69]. Lazzarini, A.K., Krauss, R.H., Chelliah. H.K., and Linteris, G.T., *Proc. Combust. Inst.* 28:2939 *(2000).*

[70]. Wanigarathne, P. C., *MS Thesis,* 2001.

[71]. Seshadri, K. and Williams, F.A., *Int. J. Heat Mass Transfer* 21:137 (1978).

[72]. Rosser, W.A., Inami, S.H., and Wise, H., *Combust. Flame* 7:107 (1963).

[73]. Chelliah, H.K. and Williams, F.A., *Combust. Flame* 80:17 (1990).

[74]. Lentati, A.M. and Chelliah, H.K., *Combust. Flame* 115:158 (1998).

[75]. Friedman, R. and Levy, J.B., *Combust. Flame* 7:195 (1963).

[76]. Patrick, R. and Golden, D.M., *Int. J. Chem. Kinet.* 16:1567 (1984).

[77]. Dacruz, F.N., Vandooren, J., and Vantiggelen, P., *Bull. Soc. Chim. Belg.* 97:1011 (1988).

[78]. Williams, F. A., *Combustion Theory,* Benjamin/Cummings Publishing Company, Menlo Park, California, 1985.

[79]. Peters, N., *Combust. Sci. Technol.* 30:1 (1983).

[80]. Chelliah, H.K., Yu, G.. Hahn, T.O., and Law, C.K., *Proceeding* of *the Combustion Institute* 24:1083 (1993).

[81]. Bonne. U., Jost, W., and Wagner, H.G., *Fire Res. Abstracts Rev.* 4:6 (1962).

[82]. NFPA, *Clean Agents Fire Extinguishing Systems,* NFPA 2001, 1999.

[83]. Rumminger, M.D. and Linteris, G.T., *Fire* Safety *Science: Proc.* of *the Sixth Int. Symp.,* Int. Assoc. for Fire Safety Science, Marne-La-Vallee, France, 2000, pp. 289-300.

[84] Rosser, W. A, Inami, S. H., and Wise, H., *Study* of *the Mechanisms of Fire Extinguishment* of *Liquid Rocket Propellants,* WADC Technical Report 59-206, 1959.

[85]. Lott, J.L., Christian, S.D., Sliepcevich. C.M., and Tucker, E.E., *Fire Technol.* 32:260 (1996).

[86]. Saso, Y., Ogawa, Y., Saito, N., and Wang, H., *Combust. Flame* 118:489 (1999).

[87]. Williams, B.A. and Fleming, J.W., *Halon Options Tech. Working Conf.,* Albuquerque, NM, 2001, pp. 144-154.

[88]. Fallis, S., Reed, R., Lu, Y.-C., Wierenga, P.H., and Holland. G.F., *Halon Options Technical Working Conference,* Albuquerque, NM, *2000,* pp. 361-370.

[89]. Fenimore, C.P. and Jones, G.W., *Combust. Flame* 10:295 (1966).

[90]. Hirst. B. and Booth, K., *Fire Technol.* 13:296 (1977).

[91]. Linteris, G.T. and Gmurczyk, GW., in *Fire Suppression System Performance of Alternative Agents in Aircraft Engine and Dry Bay Laboratory Simulations* (R.G. Gann, Ed.), National

Institute of Standards and Technology, Gaithersburg, MD, 1995.
[92]. Mache, H. and Hebra, A., *Sitzungsber. Osterreich. Akad. Wiss.* IIa, 150:157 (1941).
[93]. Puri, I.K. and Seshadri, K., *Combust. Flame* 65:137 (1986).
[94]. Santoro, R.J., Semerjian, H.G.. and Dobbins, R.A., *Combust. Flame* 51:203 (1983).
[95]. Charalampopoulos, T.T., Hahn, D.W., and Chang, H., *Appl. Opt.* 31:6519 (1992).
[96]. Dibble, R. W., Ph.D. Dissertation, University of Wisconsin, Madison, 1975.
[97]. Nguyen, Q.-V., Ph.D. Dissertation, University of California, Berkeley, 1995.
[98]. Rudder, R.R. and Bach, D.R., *J. Opt. Soc. Am.* 58:1260 (1968).
[99]. D'Alessio, A., in *Particulate Carbon: Formation during Combustion* (Siegla, D. *C.* and Smith, G. W., Ed.), Plenum Press, New York, pp. 207-256, 1981.
[100]. Dobbins, R.A. and Megaridis, C.M., *Langmuir* 3:254 (1987).
[101]. Koylu, U.O., Mcenally, C.S., Rosner, D.E., and Pfefferle, L.D., *Combust. Flame* 110:494 (1997).
[102]. Taylor, B. N. and Kuyatt, C. E., *Guidelines far Evaluating and Expressing the Uncertainty of NIST Measurement Results*, National Institute of Standards and Technology, NIST Technical Note 1297, 1994.
[103]. Rumminger, M.D. and Linteris, G.T., *Proc. Combust. Inst.* 29:submitted (2002).
[104]. Rumminger, M.D. and Linteris, G.T., *Combust. Flame* 128:145 (2002).
[105]. Glassman, I., *Combustion,* Acedemic Press, New York, NY, 1977.
[106]. Lissianski, V.V., Maly, P.M., Zamansky, V.M., and Gardiner, W.C.. *Industrial & Engineering Chemistry Research* 40:3287 (2001).
[107]. Babushok, V., Tsang, W., Linteris, G.T., and Reinelt, D., *Combust. Flame* 115:551 (1998).
[108]. Roper, F.G., *Combust. Flame* 29:219 (1977).
[109]. Gomez, A. and Rosner, D.E., *Combust. Sci. Technol.* 89:335 (1993).
[110]. Takahashi, F., "NASA-Glenn, Personal Communication, Sept. 2001.
[111]. Urban, D.L., Yuan, Z.G., Sunderland, P.B., Linteris, G.T., Voss, J.E., Lin, K.C., Dai, Z., Sun, K., and Faeth, G.M., *AIAA J.* 36:1346 (1998).